Thesis for the degree
Master of Science

Submitted to the Scientific Council of the
Weizmann Institute of Science
Rehovot, Israel

עבודת גמר (תזה) לתואר
מוסמך למדעים

מוגשת למועצה המדעית של
מכון ויצמן למדע
רחובות, ישראל

By
Lee Peleg

מאת
לי פלג

העברת יציבות מופע על פני מקשתת התדרים האופטיים באמצעות מסרק תדרים אופטי

Transfer of phase stability across the optical spectrum using an optical frequency comb

Advisor:
Roee Ozeri

מנחה:
רועי עוזרי

March 2018

ניסן תשע״ח

To Yali and Alma,

with love

Abstract

Spectrally narrow optical electronic transitions in trapped ion systems can be used as high quality frequency standards in a timekeeping device. To extract the frequency accuracy of such atomic standard, an external laser system is maintained in coherence with the ion by a repeated sequence of spectroscopic measurements. For such operation, a spectrally stable laser is required, as the laser intrinsic phase noise limits the ability to perform long and coherent observations of the ion. Stabilization of a laser linewidth is usually done by comparing it to a different frequency standard, commonly a well maintained high finesse optical cavity or a different stable laser system of roughly the same frequency. In this work we reduced phase noise of a 674nm laser diode by comparing it to a narrow linewidth laser of wavelength 1560nm. By phase locking an optical frequency comb to that stable laser, we were able to deliver its relative frequency stability all across the optical spectrum. We then used one of the comb frequency components as a frequency reference for our diode laser. We characterized the performance of the electronic locking circuit, and observed the spectral properties of the locked and stabilized 674nm laser, using a different laser system as probe. We then performed a series of spectroscopic measurements on a trapped ion, estimating the coherence time limit imposed by either the laser residual phase noise or by ion-related noise processes. Other limiting factors, such as servo bumps or frequency drifts were also identified and characterized.

Acknowledgements

Being an experimental physicist for the first time in my life, I had to learn a lot inside and outside the immediate scope of this project. Seeking help or looking for an answer was a major part of my day to day here, so it seems like a good place to thank all those whose physical, intellectual (and sometimes even mental) help was indispensable to this work. Starting with my group members, I first like to thank Nitzan, whose talent, experience and wisdom made him my first and usually last stop to every problem I encountered, to Meir for supporting, discussing and teaching electronics, and to Ravid, Tom, Yotam, Ziv, Thomas, Ruti, Meirav and Jonathan for being always ready and happy assist in building the system, performing measurements, analyzing the results and discussing whatever follows into mind. Id like to thank my advisor Roee for introducing me to the ion-trapping world, bringing an enthusiastic approach into science in and mentoring in particular, and for being always available for giving advice and review. I would like also to thank the Complex Systems faculty staff, to Ezra, Guy, Gershon, Yuri, Rusti, Malka, Perla and everyone else who solved every electronic, mechanical or logistic problem I ever had, and to all other friends and colleagues here who made all of this to be a great experience.

Outside the faculty I was greatly supported and encouraged by my family, and I wish to show them my gratitude as well; Specifically to my parents, who are always proud and supportive of the paths I take, to my wife Yael, for enjoying taking it with me, and to my daughter Alma, which came into the world when I just started the M.Sc. studies and gave me a compelling lesson about life.

Contents

Part I

Introduction and Background

Chapter 1

Narrow linewidth lasers and atomic clocks

The ability to accurately track time had always played a central role in advances of modern technology and science. Clocks, being the machinery aimed for performing this task, are constantly improved and re-invented to address the requirement presented by fields like precision measurements, navigation and telecommunication. A clock performance is highly dependent on the quality of the periodic phenomena it counts, such as pendulum swings or crystal oscillations. Atomic clocks, tracking the oscillation frequency defined by the energy gap of two internal states of an atom, first appeared over 60 years ago and since played a dominant part in the aforementioned fields, yielding applications such as the Global Positioning System or the redefinition of the second.

Atomic clocks, that are now common both in science and industry, track the oscillation of two hyperfine levels of an atom (The second is defined by the two cesium-133 ground-state hyperfine split levels). The quality of an oscillator, defined as its oscillation frequency divided by its frequency uncertainty $f_0/\Delta f$, ultimately determines the performance of a clock which uses that oscillator to count time. The oscillation frequency of the common atomic standards is in the microwave frequency regime, and using more energetic transitions in the optical domain could result in far better quality due to the large increase in f_0. However, the technical difficulty of counting the electric field oscillations at the THz regime prevented the realization of such optical atomic frequency standards, or at least rendered the ability to perform absolute readout of an optical frequency an extremely complicated task [1]. Developments in the field of fs-lasers and the appearance of the frequency comb about two decades ago, provided means to bridge the gap between the optical and radio frequency ranges, track and count optical frequencies and consequently build optical atomic clocks. In recent years several optical frequency clocks were demonstrated, exhibiting fractional frequency uncertainty $< 10^{-18}$, surpassing that of the microwave atomic clocks by several orders of magnitude [2] [3].

As the energy level transition of an atom is of quantum nature, there is no immediate observable we can measure to estimate the corresponding transition frequency. To actually extract the desired frequency we let our atom interact with a classical system which changes the internal state of the atom. By measuring the atom post interaction, we can tune our classical system to be resonant with the desired atomic transition. In an optical clock, the classical system is a laser, which is an electric field

oscillating at an optical frequency initially close to the atomic frequency. To recover that frequency a spectroscopic measurements is conducted, after which the laser is tuned to the estimated atomic transition frequency. We can thereafter measure the laser frequency and obtain an oscillator ideally locked to an atomic transition.
Owing to the fact that the high Q-factor resonance is a result of atom-light interaction, both ingredients are needed to be highly coherent. Specifically, the laser field oscillation frequency should be stable enough to be able to perform high resolution spectroscopy. Moreover, considering the frequency uncertainty with respect to the integration time [4]:

$$\sigma_y(\tau) = \frac{\Delta f}{f_0}\sqrt{\frac{T_c}{\tau}} \tag{1.1}$$

with τ being the averaging time and T_c the single measurement time, we note that whenever the frequency instabilities induced by the laser exceed those that are inherent to the atom, such as the quantum limiting projection noise, the total instability of our clock is actually dominated by the laser instability. Other effects, such as the Dick effect [5] [6], degrades the clock performance through aliasing of fast oscillator frequency noise to low frequency noise. It is therefore clear that reduction of the probing laser linewidth is necessary to obtain a high performance clock as described.
Driven by precision metrology applications, the field of narrow linewidth lasers advanced over the years to produce spectrally narrower lasers, reaching the 1 Hz linewidth [7] [8]. To narrow a laser linewidth, two main tasks should be performed: attaining a frequency reference with better Q factor and tightly lock the laser to it. In the most common scheme, a carefully designed and well maintained Fabri-Perot cavity is used as the frequency reference, and the laser linewidth is kept close to its resonance by means of active electronic feedback, with Pound-Drever-Hall technique being a popular choice for such setup. Cavity stabilization offers great frequency reference with linewidth reaching the sub-Hz level, but maintaining such a cavity is a formidable task - the limiting factor is usually the fluctuations of the two mirror spacing, and it has to be stabled to the femto-meter level and isolated from any mechanical, acoustical or thermal source of vibration. An alternative frequency reference might be an already spectrally narrow laser, but such narrow linewidth reference laser is not readily available for an arbitrary wavelength, and can only be used as a reference in a very narrow band of frequencies around it.
In this work we follow a somewhat different approach, and use the optical frequency comb not only to link the optical frequency to the RF, but also to bridge over the spectral difference between a narrow linewidth laser at a wavelength of 1.5 µm and our laser to be narrowed at 674 nm. The reference laser at the telecom frequency is referenced to an ultra low noise cavity and stabilized by PDH technique. The comb, locked to that stable laser, acts as a frequency bridge and delivers coherent frequencies, with their phase stability acquired from the stable laser reference, to the rest of the optical spectrum. We then use one of these frequency components as a frequency reference to lock the 674 nm laser to, and perform measurements with a different 674 nm laser and a single trapped ion to estimate the performance of such laser locking scheme.
In the following chapters we first present some background and theoretical description of our problem: the statistical tools we use to characterize out laser phase noise, the laser operation mechanism and its various noise origins, the frequency comb principle of operation, and some technical methods for detecting noise and removing it by means of control circuitry. In the second part of the thesis a description of the experimental setup is presented, following by the details of performed measurements and their results.

Chapter 2

Characterization of phase noise properties of an oscillator

A first step in the task of estimating and reducing a laser phase noise is to develop common tools and methods to describe and measure the phase noise of an oscillator. The discussion presented in the following chapter is based on [9]

2.1 A noisy oscillator model

A perfect oscillator with a frequency $\omega_0 = 2\pi\nu_0$ can be described using any perfectly periodic function with the same frequency. A real-world oscillator, however, regardless of the physical nature of its periodic phenomenon, can usually be described as an ideal oscillator with two super-imposed noise processes:

$$U(t) = [U_0 + \Delta U(t)]\sin(2\pi\nu_0 t + \varphi(t)) \tag{2.1}$$

The two non-perfect processes, $\Delta U(t)$ and $\varphi(t)$ represent unwanted amplitude and phase noise respectively, that degrade the performance of the ideal oscillator. Depending on the physical nature of the oscillator, a large variety of physical processes might contribute to any of the two noise processes in a way that cannot be straight-forwardly accounted for. Being so, statistical tools have to be applied to describe the properties of these random processes. We should notice that the random phase noise process determines completely the frequency fluctuations, owing to the definition of the frequency:

$$\nu(t) = \frac{1}{2\pi}\frac{d\Phi(t)}{dt} = \nu_0 + \frac{1}{2\pi}\frac{d\varphi(t)}{dt} \triangleq \nu_0 + \Delta\nu(t) \tag{2.2}$$

Where $\Phi(t) = 2\pi\nu_0 t + \varphi(t)$ is the oscillator phase described as a random noise process superimposed on a linear trend with rate $2\pi\nu_0$.
The analysis to be presented is applicable to any of the two noise processes, as long as we assume that their underlying statistic is stationary and ergodic. On the other hand, since the focus of this work is elimination of an oscillator phase noise, we will assume from here on $\Delta U(t) = 0$ and ignore amplitude fluctuations. The following definitions are used as the normalized frequency and phase fluctuations:

$$x(t) = \frac{\phi(t)}{2\pi\nu_0}, \quad y(t) = \frac{\Delta\nu(t)}{\nu_0} = \frac{dx(t)}{dt} \tag{2.3}$$

2.2 Fourier domain analysis

The frequency stability of the oscillator can be characterized in terms of the intensity of the frequency (or phase) fluctuations, as a function of the spectral frequency. This is usually done by computing the power spectral density function based on the frequency (or phase) time signal.

2.2.1 Power spectral density

A spectral analysis of the frequency fluctuations, $\Delta\nu(t)$, can be achieved by first computing the autocorrelation function:

$$R_\nu(\tau) = \int_{-T}^{T} \Delta\nu(t+\tau)\Delta\nu(t)dt = E[\Delta\nu(t+\tau)\Delta\nu(t)] \tag{2.4}$$

Where the last step is valid for an ergodic process. For a weak-sense stationary process we can obtain the two sided power spectral density as the Fourier transform of the autocorrelation function, following Weiner-Khintchine theorem:

$$S_\nu^{2-sided}(f) = \int_{-\infty}^{\infty} R_\nu(\tau)e^{-i2\pi f\tau}d\tau \tag{2.5}$$

This PSD also defines the normalized frequency deviation PSD, $y(t) = \frac{\Delta\nu(t)}{\nu_0}$, and the phase PSD $S_\phi(f)$, following (2.2):

$$S_y(f) = \left(\frac{1}{\nu_0}\right)^2 S_\nu^{2-sided}(f) = \left(\frac{f}{\nu_0}\right)^2 S_\phi(f) \tag{2.6}$$

From the definition of the autocorrelation function in Eq. (2.4), the standard deviation of the purely fluctuating random process can be estimated as:

$$R_\nu(0) = \int_{-T}^{T} \Delta\nu(t)\Delta\nu(t)dt \equiv \left\langle\sigma_\nu^2\right\rangle = \int_{-\infty}^{\infty} S_\nu^{2-sided}(f)df \tag{2.7}$$

We note that since the frequency fluctuations, and hence their autocorrelation function are real valued functions, the 2-sided spectrum is symmetric about the zero frequency, and so one can present only the one sided spectrum as

$$S_\nu^{1-sided}(f) = 2\cdot S_\nu^{2-sided}(f), \quad f>0 \tag{2.8}$$

The extraction of the frequency (or phase) fluctuation signal from an oscillating signal is not a trivial task, and a more straight-forward measurement is the power spectral density of the oscillating signal itself. We can relate the oscillating signal PSD $S_U(f)$ to the phase noise PSD by the following argument: Describing our field as the complex form of Eq. (2.1) without amplitude fluctuations, its power spectral density is:

$$S_U(\nu) = \int_{-\infty}^{\infty} e^{-i2\pi\nu\tau}d\tau U_0^2 e^{i2\pi\nu_0\tau}\int_{-\infty}^{\infty} dt e^{i(\varphi(t+\tau)-\varphi(t))} \tag{2.9}$$

We can replace the second integral time average by the ensemble average over $\Phi(t,\tau) \triangleq \varphi(t+\tau)-\varphi(t)$ (Ergodic assumption) and using the central limit theorem (Gaussian probability distribution) we obtain:

$$\left\langle e^{i\Phi(t,\tau)}\right\rangle = \int_{-\infty}^{\infty} \underbrace{\frac{1}{\sigma\sqrt{2\pi}}e^{-\frac{\Phi^2}{2\sigma^2}}}_{p(\Phi)} e^{i\Phi(t,\tau)}d\Phi = e^{-\frac{\sigma^2}{2}} \tag{2.10}$$

where σ is the second moment of $\Phi(t,\tau)$ and can be written as:

$$\sigma^2 = \left\langle\Phi^2\right\rangle - \cancel{\left\langle\Phi\right\rangle^2} = 2\left\langle\varphi(t)^2\right\rangle - 2\left\langle\varphi(t)\varphi(t+\tau)\right\rangle = 2\int_0^\infty S_\varphi(f)\left[1-\cos(2\pi f\tau)\right]df \tag{2.11}$$

The oscillator power spectral density can be then written as:

$$S_U(\nu) = U_0^2 \int_{-\infty}^{\infty} e^{-i2\pi(\nu-\nu_0)\tau} d\tau e^{-\int_0^{\infty} S_\varphi(f)[1-\cos(2\pi f\tau)]df} \tag{2.12}$$

When we consider the weak phase fluctuation limit where $S_\phi(f)df \ll 1$ we can expend the exponent to first order and obtain:

$$\begin{aligned} S_U(\nu) =& U_0^2 \int_{-\infty}^{\infty} \left[1 - R_\phi(0) + R_\phi(\tau)\right] e^{-i2\pi(\nu-\nu_0)\tau} d\tau \\ =& U_0^2 \left[1 - \left\langle \sigma_\varphi^2 \right\rangle\right] \delta(\nu-\nu_0) + U_0^2 S_\varphi^{2-sided}(\nu-\nu_0) \end{aligned} \tag{2.13}$$

The power in the coherent peak drops by an amount proportional to the total noise power, and the phase noise power spectral density is superimposed on the delta-like power spectrum of the coherent oscillation. Thus, for low overall noise the two sidebands are a good estimator of the phase noise PSD. When the phase noise grows larger, the relationship of the two PSDs become less straightforward, and the oscillating signal's PSD itself cannot serve as a simple description of the phase noise spectrum.

2.2.2 The power-law spectral density model

Analysis done for real-world oscillators, such as electronic quartz oscillators, laser and atomic standards [10], shows that experimental results for a oscillator's phase noise power spectral density can be modeled using the a power law model:

$$S_y(f) = h_\alpha f^\alpha \tag{2.14}$$

with α taking on typical integral values between -2 and 2. The classical terminology of noise can be applied here, and we can recognize the type and possible causes of the different power law noise:

1. $\alpha = -2$ is a frequency random walk spectrum, and is usually dominant very close to the carrier frequency, making it hard to measure. It usually relates to the physical environment of the oscillator, like the temperature stability, mechanical shocks, vibrations, etc.

2. $\alpha = -1$ is a frequency flicker noise spectrum. It is common in high quality resonators, and though not fully understood, its causes are assumed to be related to either the resonator's physical properties (in quartz oscillators), or to the oscillator's electronics.

3. $\alpha = 0$ is a frequency white noise, common in oscillators where the oscillation frequency is electronically locked to a reference oscillation.

4. $\alpha = 1$ is a phase flicker noise. This kind of noise is also usually introduced by electrical components, such as amplifiers and frequency multipliers, and is common even in high quality oscillators.

5. $\alpha = 2$ is a phase white noise spectrum. Usually attributed to stages of amplification, it can be kept low by careful selection of low noise electrical amplifiers, and band pass filtering the oscillator output.

To obtain a finite power model, both low and high frequency cutoffs should be introduced.

2.3 Time domain analysis

We wish to analyze the random frequency noise process $y(t)$. Assuming the process is purely fluctuating, its variance is defined as:

$$\sigma^2 = \langle y(t)^2 \rangle = R_y(0) = \int_{-\infty}^{\infty} S_y^{2-sided}(f) df \tag{2.15}$$

In an experiment we cannot observe the actual continuous-time frequency fluctuation signal. Instead, we can estimate the average frequency $\bar{y}_i$ at time t_i estimated over some time τ using a frequency counter:

$$\bar{y}_i = \frac{1}{\tau} \int_{t_i}^{t_i+\tau} y(t) dt = \frac{x(t_i+\tau) - x(t_i)}{\tau} \tag{2.16}$$

With $t_{i+1} - t_i = T$ the frequency estimation period. This yields a time series dependent on the integration time τ, which in turn has its own statistical measures, such as the variance $\sigma^2_{\bar{y}_i}(\tau)$. This variance is a key characteristic of an oscillator's frequency stability, which we can estimate from a finite measurements set. Assuming ergodicity, we can use the classical N-sample variance estimator:

$$\left\langle \sigma_y^2(N,T,\tau) \right\rangle = \left\langle \frac{1}{N-1} \sum_{i=1}^{N} \left(\bar{y}_i - \frac{1}{N} \sum_{j=1}^{N} \bar{y}_j \right)^2 \right\rangle \tag{2.17}$$

It would be wrong to assume that this estimator converges as we increase N, as is the case with independent identically distributed data. For actual noise processes of an oscillator, where a substantial portion of the total power is concentrated at the very low frequency portion of the spectrum, correlation between samples tends to be high and the data is not independently distributed.

2.3.1 Allan variance

We need then to specify T and N so to be able to make meaningful and comparable estimation of the noise statistical characteristics. Following the work of Allan [11], a common choice is the no dead time two sample variance, called the Allan variance (AVAR):

$$\left\langle \sigma_y^2(N,T,\tau) \right\rangle \triangleq \sigma_y^2 = \left\langle \sum_{i=1}^{2} \left(\bar{y}_i - \frac{1}{2} \sum_{j=1}^{2} \bar{y}_j \right)^2 \right\rangle = \frac{1}{2} \left\langle (\bar{y}_n - \bar{y}_{n+1})^2 \right\rangle \tag{2.18}$$

A major advantage of AVAR over other N-sample variance is its convergence when applied to a noise model as the one introduced in section (2.2.2). It can be shown [12] that AVAR can be obtained from the power spectral density of the frequency fluctuation by applying the following filter:

$$\sigma_y^2 = 2 \int_0^{\infty} df S_y(f) \frac{\sin^4(\pi f \tau)}{(\pi f \tau)^2} \tag{2.19}$$

The following table summarizes the functional dependency of σ_y^2 on τ in the presence of different power-law noise processes:

Allan variance response to noise			
Noise Type	$S_y(f)$	σ_y^2	Slope of σ_y^2 Vs. τ on log-log plot
Frequency random walk	$h_{-2} f^{-2}$	$\frac{2\pi h_{-2} \tau}{3}$	1
Frequency flicker noise	$h_{-1} f^{-1}$	$2 \ln 2 h_{-1}$	0
Frequency white noise	h_0	$\frac{h_0}{2\tau}$	-1
Phase flicker noise	$h_1 f$	$\frac{3h_1}{4\pi^2\tau^2}(1.038 + 3 \ln 2\pi f_H \tau)$	≈ -2
Phase white noise	$h_2 f^2$	$\frac{3h_2 f_H}{4\pi^2\tau^2}$	-2

The table highlights the ability to extract the AVAR or PSD plots same information regarding the oscillator noise.

2.3.2 Allan variance for a frequency drift

When the fractional frequency presents a liner drift, i.e. $y(t) = \alpha t$ the resulting Allan variance is:

$$\sigma_y^2 = \frac{\alpha\tau}{\sqrt{2}} \tag{2.20}$$

So it will show up as a positive slope on the Allan deviation plot, or as $1/f^2$ slope at low frequencies at $S_y(f)$.

Chapter 3

Laser

3.1 Laser principle of operation

Laser radiation is a form of spatially and temporally coherent electromagnetic radiation induced by a laser instrument. Such instrument consist of an light amplifying medium and a resonant optical cavity for a positive feedback between the emitted radiation and the amplifying medium.

3.1.1 The Amplifying Medium

Three distinct processes are considered when describing the interaction of quantized electromagnetic field and an electronic transition in matter of energy $E_2 - E_1 = h\nu$, namely photon absorption, spontaneous emission and stimulated emission. In equilibrium the rate of the three processes combined vanishes and the occupation of each quantum level remains constant:

$$\frac{dN_2}{dt} = 0 = B_{12}N_1\rho(\nu) - A_{21}N_2 - B_{21}N_2\rho(\nu) \tag{3.1}$$

Where $N_1,\ N_2$ are the populations of the two matter states, $\rho(\nu)$ is the energy density of the electromagnetic field at frequency ν, and A_{21}, B_{21} and B_{12} are called Einstein coefficients and relates to the matrix elements coupling the electronic levels and the continuum vacuum states. The third term in Eq (3.1) is the rate for stimulated emission, a process in which the matter de-excite, emitting a photon coherent with the present electromagnetic field, and increase its occupation number by one. Proportional to the energy density of the present electromagnetic field, this process serves as the physical basis for photon amplification inside a lasing material, as the emitted photon carries the exact same polarization, phase and direction as the stimulating electric field, hence it constructively adds up to increase the intensity of that field. For a non-degenerate two level system $B_{21} = B_{12}$, and the intensity of an electromagnetic wave along its propagation direction z is:

$$\frac{\partial n}{\partial z} = b_{21}(N_2 - N_1)n \rightarrow n(z) = n_0 e^{b_{21}(N_2-N_1)z} \equiv n_0 e^{Gz} \tag{3.2}$$

When $N_1 > N_2$ we get the usual light absorption in a material $n(z) \sim e^{-\alpha z}$. When $N_2 > N_1$ however, we get light amplification through the medium. The process of achieving $N_2 > N_1$ is called population inversion, and is a required condition for lasing. We note that since Einstein's $B_{21} = B_{12}$, we cannot achieve more the 50% occupation of the excited state by coupling the two levels, as the stimulated emission rate will be equal the absorption rate when $N_1 = N_2$, resulting in a steady state occupations. In a general scheme for population inversion the two lasing levels of $E_u > E_d$ are considered along with two other energy levels - the ground state E_g and the excited state E_e such that $E_e > E_u > E_d > E_g$. If the upper lasing level have a longer decay time with respect to any other excited level assuming the excited level decays dominantly to the upper lasing level, a population inversion can be generated by exciting the atoms to the excited state, and since it decays fast to E_u, the population at this level will accumulate to a large population inversion with respect to the almost unoccupied E_d. any photon resonant with this transition can now be amplified, due to the large population inversion of the levels. Equation (3.2) was derived for a photon of energy $\hbar\omega$ exactly resonant with the proposed to level systems, so that $b_{21} \equiv b_{21}\delta(\omega - \omega_{21})$. In actual atomic systems variations of the energy levels across the amplifying medium due to physical processes (such as collisions, Doppler shifts, stark shifts, magnetic field splitting, etc) and the finite lifetime of the excited state introduce broadening to the spectral shape of the electric transition probability. In such realistic case, the gain coefficient G can be written as:

$$G(\omega) = \Delta N b_{21} g(\omega) \tag{3.3}$$

Where $g(\omega)$ captures the spectral shape of the transition, which usually carries a shape of a Lorentzian or Gaussian around ω_{21}

3.1.2 The optical cavity

Placing the amplifier medium inside an optical cavity resonator greatly enhances the laser performance, as it supplies the essential optical feedback for building a coherent amplification, due to multiple passings of the light through the optical amplifier. Moreover, its spectral characteristics usually provide a filtering mechanism, resulting in a narrower band of optical radiation.
A simple optical cavity can be thought of as two plane mirrors with high reflectance and low transmission, placed parallel to one another. With r_i and t_i the reflectance and transmission of the two mirrors, the electric field leaving the cavity is the sum over all round trips of the field inside it:

$$E = E_0 t_1 t_2 e^{-i\frac{\omega}{c}L} \sum_{m=0}^{\infty} \left(r_1 r_2 e^{-i2\frac{\omega}{c}L} \right)^m = E_0 t_1 t_2 e^{-i\frac{\omega}{c}L} \frac{1}{1 - r_1 r_2 e^{-i2\frac{\omega}{c}L}} \tag{3.4}$$

and the power is

$$P = |E|^2 = \frac{E_0^2 t_1^2 t_2^2}{1 + r_1^2 r_2^2 - 2 r_1 r_2 \cos\left(\frac{2\omega L}{c}\right)} \tag{3.5}$$

The frequency dependent term in the sum give rise to a constructive interference when $\omega = 2\pi n \cdot \frac{c}{2L}$, and destructive interference almost everywhere else. Being so, only very specific wavelength are able to perform multiple round trips inside the cavity, leading to a longitudinal mode constraint on the amplified laser field. The term $\frac{c}{2L}$ is called the free spectral range (FSR) of the cavity. The spectral width of each such peak is determined as the full width at half the maximal power (FWHM), and can be shown to be:

$$\delta\nu = \frac{1 - r_1 r_2}{\pi\sqrt{r_1 r_2}} \frac{c}{2L} \tag{3.6}$$

Hence the more reflecting the mirrors are, the narrower a peak will be, due to contribution of more waves to the interference pattern. The Finesse of the cavity, a characteristic for the losses of the cavity, is defined by:

$$\mathcal{F} = \frac{FSR}{\delta\nu} = \frac{\pi\sqrt{r_1 r_2}}{1 - r_1 r_2} \equiv \frac{c}{2L} 2\pi\tau_p \tag{3.7}$$

Where τ_p is the photon lifetime inside the cavity due to losses. The Finesse can be interpreted as the average number of round trips for a photon inside the cavity before it is lost.

3.1.3 Conditions for laser oscillation

In a configuration of an optical amplifier inside a positive feedback loop, the conditions under which a stable laser radiation is emitted should be considered. Taking β as the feedback gain parameter, A as the optical amplification factor and E_i, E_o as the initial and emitted laser field, we have:

$$E_o = A(E_i + \beta E_o) \rightarrow \frac{E_0}{E_i} = \frac{A}{1 - \beta A} \tag{3.8}$$

when $\beta A > 1$ the positive feedback becomes negative, indicating an instance configuration. For βA gradually increased towards 1, the gain parameter increases to infinity. In reality the gain saturates earlier due to the non-linear characteristics of the amplifier. Talking the round trip gain as $A = e^{2(G-\alpha_0)L}$, with α_0 represents losses due to absorption or scatterings, and the feedback parameter $\beta = r_1 r_2$, we can set $\beta A = 1$ to get:

$$r_1 r_2 e^{2(G-\alpha_0)L} = 1 \rightarrow G = \frac{1}{2L}\ln(r_1 r_2) + \alpha_0 \tag{3.9}$$

So we got a threshold condition on the round trip gain - if it can compensate the losses due to the end mirrors or other imperfections along the way, a stable lasing will build up, even from optical noise induced by spontaneous emission.

3.2 External cavity diode laser

The ECDL is a typical laser apparatus, emitting a relatively narrow band laser radiation over a widely tunable range of frequencies. It consist of a p-n junction diode as the laser source and an external cavity for enhancement of the optical feedback and noise filtering.

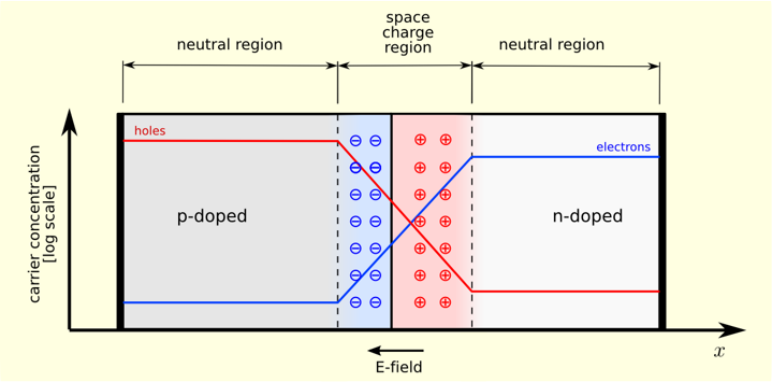

Figure 3.1: a PN junction electrons and holes concentration diagram. The depletion region is the central zone where electrons and holes recombined and an electric voltage across it balance the excess electron-hole recombination (Image taken from Wikipedia)

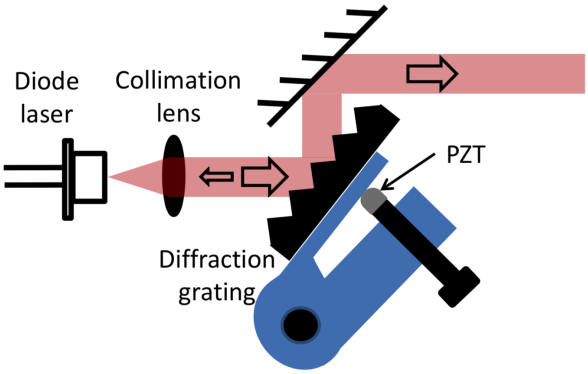

Figure 3.2: An ECDL in Litrrow configuration. The grating is aligned such that the first diffraction order is directed back into the diode thus closing a cavity (Image taken from [13])

In a semiconductor, the gap between the valance and conduction band is relatively small, and at finite temperature very few electrons occupy the conduction band. Doping the semiconductor with donor atoms (n-type doping) adds more electrons to the conduction band, while doping it with acceptor atoms (p-type doping) leads to more holes occupying the top of the valance band. When such two doped semiconductors are brought together, the Fermi level energy levels out, leading to holes and electrons recombination around the contact surface. The area around which the holes and electrons density changes gradually with respect to the far p (or far n) side of the pn diode, is referred to as the depletion region. When forward bias voltage is placed along the two terminals of the diode, electrons from the n side and holes from the p side both enter the depletion region and form the basis for population inversion. The more charge carriers are injected through the terminals, the more electrons and holes occupy their excited states at the depletion region, and once population inversion and lasing condition is achieved, the pn diode starts to act as a laser.
The optical feedback in this configuration comes from Fresnel reflection of light from the output facet of the semiconductor crystal:

$$R = r^2 = \left(\frac{n-1}{n+1}\right)^2 \approx 30\% \tag{3.10}$$

for $n \approx 3.5$. This is sufficient for lasing, due to the high optical amplifier gain, but lead to a wide radiation bandwidth of $\delta\nu \sim 10{-}100\,\mathrm{MHz}$, which is generally too wide to be reduced by means of control electronics. The FSR of a diode laser, considering the change in refractive index with frequency, gives:

$$\Delta\nu_{\phi=2\pi n} = \frac{c}{2nL\left(1+\frac{\nu}{n}\frac{dn}{d\nu}\right)} \sim 100\ [GHz] \tag{3.11}$$

The gain bandwidth however is much larger than the FSR, often leading to multimode longitudinal oscillation of the diode laser.

To suppress the multimode oscillations of the laser and further narrow each mode spectral width, an external cavity is added. Just like the first cavity, it constrains the laser radiation spectrum through the introduction of interference with the reflected light. A typical configuration for such external cavity is the Litrrow configuration, which contain a collimation lens and a grating acts as the end mirror of the external cavity. Such a scheme is presented in figure 3.2. The grating is placed such that the first order diffraction is reflected back into the laser diode creating optical feedback, while the zeroth order diffraction reflects off the grating as the laser output radiation. the wavelength dependent angle of

diffraction for gratings ensures that only a narrow band of frequencies are even able to reflect back into the diode, resulting in a much narrower effective gain profile for the entire system. Due to the higher overall reflectivity and cavity length, the width of each longitudinal permitted mode is reduced to about 1 MHz, which makes it easier for reduction using active electronic control.

3.3 Noise model of a diode laser

The spectral linewidth of a diode laser is dominated by spontaneous emission process. following the derivation presented in [14], each spontaneously emitted photon change the overall field phase by both addition of a random phase and through change of refractive index due to the change in field intensity. The field and fluctuation term phasor can be described as:

$$\begin{aligned} \beta &= \sqrt{I}e^{i\phi} \\ \Delta\beta_i &= e^{i(\phi+\Delta\phi_i)} \end{aligned} \tag{3.12}$$

Taking the electrical field as $E = \beta e^{i(\omega t - kz)} + c.c.$ and considering the wave equations, we can derive an equation for β:

$$\frac{2i\omega}{c^2}\left(\epsilon + \frac{\omega}{2}\frac{\partial\epsilon}{\partial\omega}\right)\dot{\beta} = \left[\frac{\omega^2}{c^2}\epsilon - k^2\right]\beta \tag{3.13}$$

with $\epsilon = (n' - in")^2$ the dielectric constant. Around equilibrium $n" = 0$ and $\epsilon = n'^2 - 2i\Delta n'\Delta n"(1+\alpha)$ where $\alpha = \Delta n'/\Delta n"$. Following the same derivation one can show that the dynamic equation for β is:

$$\dot{\beta} = \left[\frac{G-\gamma}{2}\right](1+i\alpha)\beta \rightarrow \begin{cases} \dot{\phi} = \frac{\alpha}{2}(G-\gamma) \\ \dot{I} = (G-\gamma)I \end{cases} \rightarrow \dot{\phi} = \frac{\alpha}{2I}\dot{I} \tag{3.14}$$

With G being the stimulated emission rate and γ the loss rate. This helps us relate the change of phase to the change in intensity. With the phase change relating to the i-th photon phase be $\Delta\phi_1 = I^{-1/2}\sin(\theta_i)$ and the phase change coming from the phase to intensity coupling $\Delta\phi_2 = -\frac{\alpha}{2I}\Delta I_i$ we have:

$$\Delta\phi = \Delta\phi_1 + \Delta\phi_2 = -\frac{\alpha}{2I} + \frac{1}{2I}\left[\sin(\theta_i) + \alpha\cos(\theta_i)\right] \tag{3.15}$$

The phase uncertainty is

$$\left\langle \Delta\phi^2 \right\rangle = \frac{Rt(1+\alpha^2)}{2I} \tag{3.16}$$

With R the spontaneous emission rate. As the power spectrum of the laser is simply the transform of $\langle\beta(0)\beta(\tau)\rangle$, its full width half max can be shown to be:

$$\Delta f = \frac{R}{4\pi I}(1+\alpha^2) \tag{3.17}$$

The α^2 term is the broadening factor leading to a broader linewidth then the expected natural linewidth of a diode laser. it usually corresponds to a couple of MHz linewidth. Further derivation can relate the spectrum to the output power per facet of the laser:

$$\Delta f = \frac{v_g^2 h\nu n_{sp}\alpha_m(1+\alpha^2)}{8\pi P_0} \tag{3.18}$$

With v_g the group velocity, $n_{sp} = gR/v_g$ the spontaneous emission factor and α_m the facet loss factor. This expression resembles that of the Schawlow-Townes quantum phase noise limit [15], with α being the broadening factor induced by the intensity to phase fluctuation coupling.

3.4 Laser phase noise due to propagation through an optical fiber

A linewidth reduction system is typically a tabletop system combining various optical, electrical and mechanical elements,and are usually cumbersome and not portable. Being so, laser light with reduced linewidth is by and large distributed to various locations via optical fibers, instead of created wherever needed. When propagating through the fiber, the laser linewidth is subjected to broadening due to a phase modulation process, induced by acoustic pressure on the silica fiber. Acoustic waves propagating through air or any other material are incident upon the fiber face, creating pressure waves that changes the optical properties of the fiber through the photo-elastic effect [16]. Considering a fiber of length L and a light phase accumulating phase $\phi = \beta L \equiv nk_0 L$ through it, the phase shift under pressure P is [17]:

$$\Delta\phi = \beta\Delta L + L\Delta\beta \tag{3.19}$$

Using Poisson's ratio μ and Young's modulus E,the phase change due to the effective length change of the fiber can be expressed as:

$$\beta\Delta L = -\beta(1-2\mu)\frac{P}{E}L \tag{3.20}$$

The change in β comes from two effects - one is the change of the fiber refractive index due to pressure, and the other is a wave-guide mode dispersion effect due to the change in fiber diameter. The second effect was shown to be negligible in fused silica fibers [17] so we disregard it. The change in optical index is related to the strain tensor ϵ through the strain-optic tensor p:

$$\Delta\eta_{ij} = \Delta\left(\frac{1}{n^2}\right)_{ij} = p_{ijkl}\epsilon_{kl} \tag{3.21}$$

With no shear strain we consider only the diagonal terms. For a homogeneous isotropic material the strain optic tensor for that part is:

$$p_{ij} = \begin{pmatrix} p_{11} & p_{12} & p_{12} \\ p_{12} & p_{11} & p_{12} \\ p_{12} & p_{12} & p_{11} \end{pmatrix} \tag{3.22}$$

And the change in optical index experienced by a wave propagating in the z direction is

$$\Delta n = -\frac{1}{2}n^3\Delta\left(\frac{1}{n^2}\right)_{x,y} = \frac{1}{2}n^3\frac{P}{E}(1-2\mu)(2p_{12}+p_{11}) \tag{3.23}$$

The total phase shift due to stress is:

$$\Delta\phi = -\beta(1-2\mu)\frac{P}{E}L + L\frac{\partial\beta}{\partial n}\Delta n = \beta(1-2\mu)\frac{P}{E}L\left(\frac{1}{2}n^2(2p_{12}+p_{11})-1\right) \tag{3.24}$$

This phase modulation becomes a limiting factor when considering the transfer of narrow linewidth laser thorough a fiber. This effect was demonstrated and shown to yield frequency modulations of 1 kHz induced by acoustical noise of intensity associated with normal speech[18]. In a different experiment, a delta like laser spectrum was shown to broaden to a $300Hz$ Gaussian linewidth when after traveling through a 25 m fiber [19].

Chapter 4

The femto-second optical frequency comb

4.1 Basic description of a mode locked laser

The basic description of a laser apparatus includes an optical gain medium and an optical resonator for applying the feedback required for a stable laser oscillation. The range of permitted frequencies is determined by the gain medium bandwidth and the losses inside the cavity. The cavity resonances are equally separated by $\delta\nu = c/2L$ with L being the cavity length, and when $2\pi \cdot \delta\nu << \Delta\omega$ the gain bandwidth, the laser is able to oscillate in multiple longitudinal modes. The overall amplitude of the electromagnetic field will be a sum of the contributions of each such mode:

$$E(t) = \sum_n \alpha_n e^{i(\omega_0 + 2\pi n \cdot \delta\nu)t + i\phi_n} \tag{4.1}$$

Usually, in both homogeneous and inhomogeneous gain broadened medium, one oscillation mode will acquire most of the gain, depleting the available gain for other frequencies by cross saturation of the gain medium. This is referred to as "gain competition" and further described in [20]. Nonetheless, in these configurations more than one mode has non-vanishing amplitude, and thus the overall power of the field at time t is a result of the interference between all oscillating modes.
In the general scenario, the phase of each mode ϕ_n is a random variable, and the various frequency components are not constructively or destructively interfere all together. Being so, the overall power of the field fluctuate periodically about its mean value, and this fluctuation is negligible with respect to the mean power of the field. On the other hand, when a fixed phase relationship is established among the relevant frequency components (e.g. $\phi_n = 0\ \forall n$), the laser output power experience constructive interference whenever $t = m/\delta\nu$ of width $\tau \propto 1/\Delta\omega$, followed by destructive interference in between these times. This gives the laser a pulse-like mode of operation, for which the output power peaks

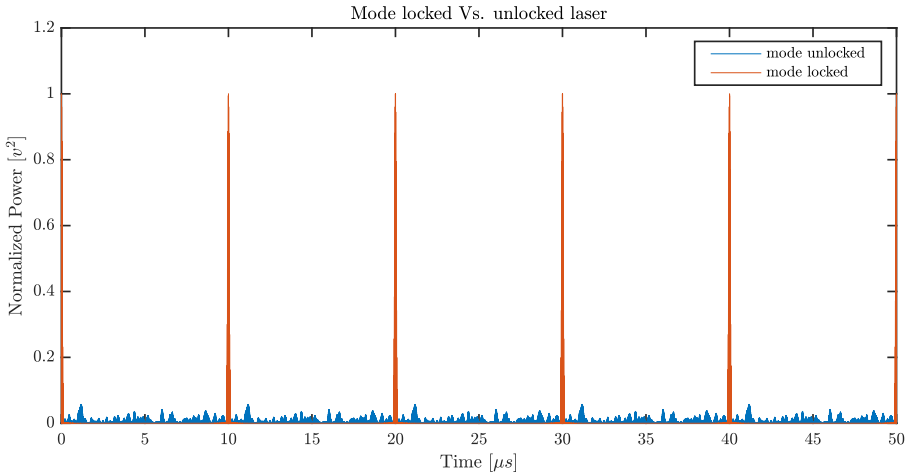

Figure 4.1: Optical power simulation of 100 frequency components spaced by 100 KHz around 200 MHz with locked phases and random phases. The pulsed-like operation of the mode locked laser is demonstrated by the periodic power peaks of resulting from the mutual constructive interference

sharply and briefly in a periodic manner in time. Figure 4.1 plots the instantaneous power for the unlocked and locked modes of the laser, for different number of contributing oscillation modes.
To attain a mode locked operation of the laser, one needs to establish a loss mechanism inducing higher net gain for short pulses. This is done by introducing either an active or a passive mode locking scheme onto the basic laser structure. Active mode locking refers to an external modulation of the intra-cavity losses or the gain, which gives rise to an AM of the oscillating frequencies and couples adjacent frequency components using their sidebands [21]. Passive mode locking, on the other hand, does not rely on external modulation or control of the laser gain and losses, but rather introduces non-linear effects of intensity related transmission or refraction [22], optimizing the gain for pulsed-like operation.

4.2 Time and frequency domain analysis

The output of a mode locked laser consist of a series of pulses, oscillating at the carrier frequency ω_0. Considering only a single pulse, its spectral contents is the Furrier transform of its temporal envelope function, centered around the carrier frequency ω_0. For example, the spectral description for a Gaussian envelope function of width τ is of a Gaussian of width $\Delta\omega = 1/\tau$ centered around ω_0. For a series of such pulses, assuming the repetition period $T_r \gg \tau$, the related Furrier description is of a series of frequency components equally spaced by $f_r = 1/T_r$ with amplitude determined by the spectrum of a single pulse. This can be seen using Poisson sum formula:

$$f(t) = \sum_{m=-\infty}^{\infty} f_P(t - mT_r) \equiv f_r \sum_{k=-\infty}^{\infty} F(k \cdot f_r) e^{i2\pi k f_r t} \tag{4.2}$$

Where $F(f)$ is the Furrier transform of the single pulse $f_P(t)$. So indeed the spectrum for such infinite series of pulses consist of a series of spectral lines at frequencies $k \cdot f_r$. If we now allow the phase of the carrier frequency with respect to the envelope peak ϕ_{ce} to evolve linearly from pulse to pulse such that $\phi_{ce} = n\Delta\phi_{ceo} + \phi_0$ for the n'th pulse, we get a series which is not quite periodic in time. Nonetheless, performing the Furrier analysis for such series as in [23], and defining $f_{ceo} = \frac{\Delta\phi_{ceo}}{2\pi} f_r$ we get the pulsed laser spectrum as a frequency comb with teeth at:

$$\nu_n = f_{ceo} + n \cdot f_{rep} \tag{4.3}$$

Figures 4.2a and 4.2b provide a description of the light pulse and its characterizing parameters in both the time and frequency domain.

4.3 Stabilization of a frequency comb

According to Eq. (4.3) a frequency comb is characterize by a set of spectral components, each determined precisely by two radio frequencies, f_{ceo} and f_{rep}. The mode spacing has been verified to be equal to the laser repetition rate up to 6 parts in 10^{-16} across the comb output spectrum [24], providing the evidence for the importance of the two radio frequencies in the determination of the comb output spectrum. In a free running mode locked laser, these two frequencies are subject to the same noise processes described in chapter 2, and each comb tooth will experience a correlated phase noise as a result of the above relation. A frequency shift by δf in f_{ceo} will result in a similar shift of all other comb teeth. A shift by δf in f_{rep} will result in a similar change to the mode spacing, and a change to each one of the comb teeth scaled by the tooth number n. For optical comb teeth of frequencies on the order of $4 \cdot 10^{14}[Hz]$ n is on the order of 10^6, which renders a huge scaling to the phase noise coming from the repetition rate noise. It is obvious then that for the comb to span

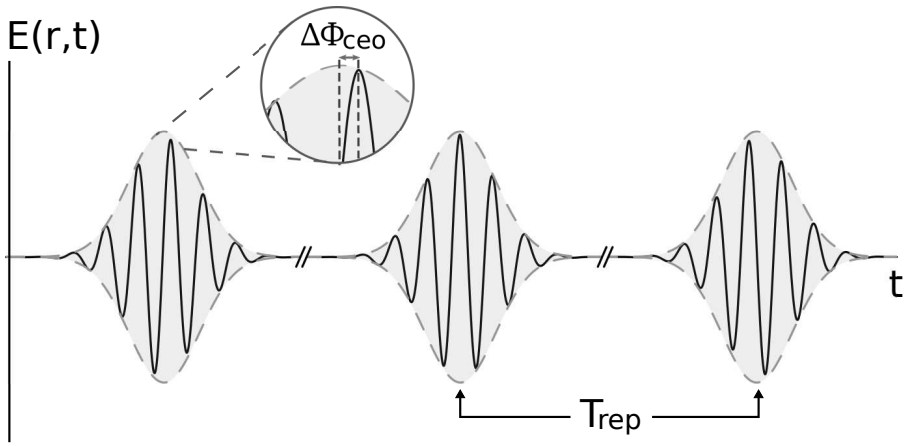

(a) Mode locked laser field Vs. time. Repetition time T_{rep} and the carrier-envelope offset phase $\Delta\Phi_{ceo}$ indicated

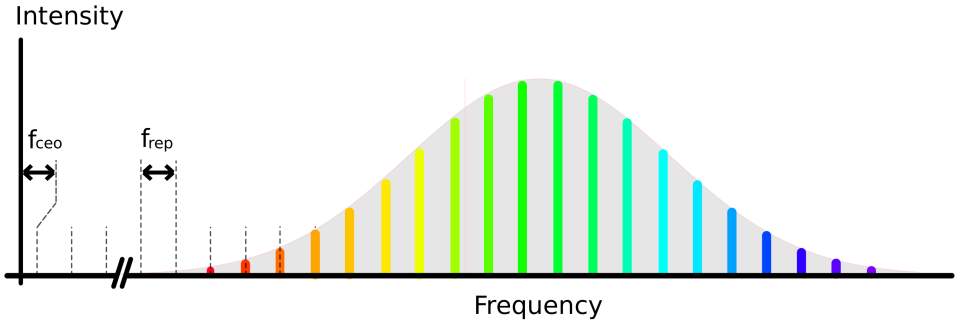

(b) Mode locked laser frequency domain description. The two RF frequencies f_{rep} and f_{ceo} are indicated as the frequency spacing and distance from DC

absolute optical references throughout the spectrum, the two radio frequencies must be extracted and stabilized.

4.3.1 Stabilization of the carrier-envelope offset frequency

Although the small contribution to the phase noise of optical frequency teeth, the inability to observe and lock the the offset frequency f_{ceo} had limited the use of frequency comb as absolute frequency references, and succeeding in stabilizing f_{ceo} had led to the exploding interest in the frequency comb in the field of precision measurements and to the physics Nobel prize in 2005. The actual physical property we wish to stabilize is the pulse to pulse carrier-envelope phase $\Delta\phi_{ceo}$, which is the excess phase that the carrier accumulates over each pulse with respect to the envelope phase, and is related to the different phase velocity and group velocity inside the cavity. Therefore, in order to stabilize this frequency we need to electronically control some properties of the laser cavity that affect this difference. This is done by controlling either the accumulated phase using intra-cavity EOMs or by tilting one of the cavity mirrors [25].
The extraction of f_{ceo} relies on the generation of an octave spanning pulse, i.e. a pulse containing in its blue spectrum frequency teeth which are double the frequency of its red spectrum teeth. This gives a hard temporal constraint on the pulse length, which amounts to a few fs pulse. It can be achieved by spectrally broadening the outgoing pulse inside an optical fiber by means of self-phase modulation [25]. When such a spectrally wide pulse is generated, its red spectrum is multiplied an overlapped

with its blue spectrum. When we the beat a spectral components f_n and f_{2n}:

$$\left.\begin{array}{l} f_n = f_{ceo} + n \cdot f_{rep} \\ f_{2n} = f_{ceo} + 2n \cdot f_{rep} \end{array}\right\} \Rightarrow 2 \times f_n - f_{2n} = 2(f_{ceo} + n \cdot f_{rep}) - f_{ceo} + 2n \cdot f_{rep} = f_{ceo} \tag{4.4}$$

This beat note frequency can be then phase locked to a reference stable oscillating signal, thus locking the frequency shift each comb tooth experiences. The excessive frequency noise random process $\Delta f_{ceo}(t)$ adds to each comb tooth in a straightforward fashion:

$$f_{ceo} = \bar{f}_{ceo} + \Delta f_{ceo}(t) \rightarrow f_n = \bar{f}_{ceo} + \Delta f_{ceo}(t) + n \cdot f_{rep} \tag{4.5}$$

So stabilizing f_{ceo} to the mHz level will yield a fractional frequency noise $< 10^{-17}$ for an optical frequency.

4.3.2 Stabilization of the repetition rate frequency

The repetition rate of a mode locked laser is easily observable, as it is manifested in the rate of laser pulses. Being so, observing the power of the laser output yield a signal oscillating at a fundamental frequency equal to the repetition rate. Stabilizing this signal is carried out by feedback on the cavity length and intra cavity EOMs. We note however that whatever residual phase noise remains for this frequency $\varphi_{rep}(t)$. it scales with the comb teeth, a factor of $\sim 10^6$ for optical frequencies. A different approach is to extract the repetition frequency from beating a stable optical frequency reference with the comb. Assuming the m^{th} comb tooth is the closest frequency component to f_{cw}, the frequency of a stable radiation source, then for every other tooth u:

$$m \cdot f_{rep} = f_{cw} - f_{ceo} + \Delta f_{rep} \rightarrow f_u = f_{ceo} + \frac{u}{m}(f_{cw} - f_{ceo} + \Delta f_{rep}) \tag{4.6}$$

So the frequency noise process scales by the teeth ratio, generating a scaled phase stability transfer of a cw laser to a large portion of the optical spectrum

Chapter 5

Measurement and reduction of a diode laser phase noise

5.1 Phase noise measurement of an optical oscillator

As described in chapter 2, an appreciation of the phase noise process of an oscillator is needed to determine the oscillator performance. The phase of the oscillator, however, cannot be directly obtained when observing the oscillating signal over time. Because of the highly non-linear nature of the sine function, we cannot obtain an estimated phase signal out of an oscillating signal, without major ambiguities. Furthermore, when it comes to laser oscillations, the high oscillation frequency of the electric field makes it intractable to build an apparatus that can track the oscillation or even count its period. The methods by which the phase noise of an optical signal can be extracted are described below.

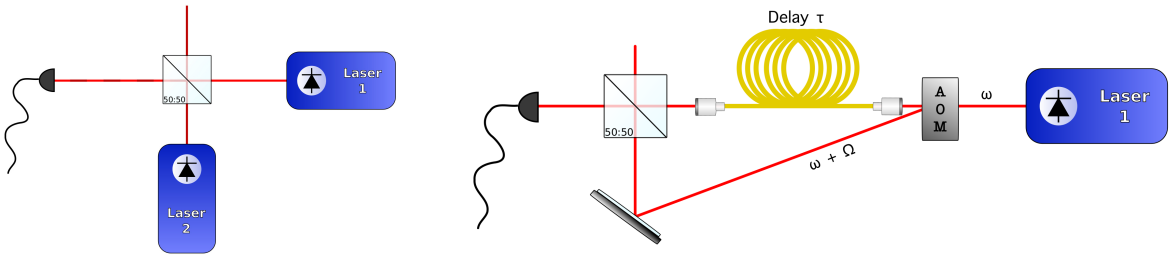

(a) Heterodyne detection scheme **(b)** Homodyne detection scheme

Figure 5.1: Heterodyne and homodyne optical schemes

5.1.1 Heterodyne detection of an oscillator phase noise

In an heterodyne scheme, like that presented in figure 5.1a, the laser under test is analyzed using a reference laser system, commonly called the local oscillator (LO). The optical scheme consist of simply beating the two lasers on a photodiode. Assuming both lasers overlap each other, the power signal detected by the photodiode will be:

$$\begin{aligned} O_{pd}(t) =& |A_{DUT}\cos(\omega_{DUT}\cdot t+\varphi_{DUT}(t))+A_{LO}\cos(\omega_{LO}\cdot t+\varphi_{LO}(t))|^2 \\ =& P_{DUT}+P_{LO}+2A_{DUT}A_{LO}\cos(\omega_{DUT}\cdot +\varphi_{DUT}(t))\cos(\omega_{LO}\cdot t+\varphi_{LO}(t)) \end{aligned} \tag{5.1}$$

Because of the photodiode finite bandwidth, which usually is of the order of $\sim GHz$, it acts as an integrator for the high optical frequencies and averages over the fast oscillating components. As for the mixed term, following the identity:

$$\cos(\omega_1\cdot t+\varphi_1)\cos(\omega_2\cdot t+\varphi_2)=\frac{1}{2}[\cos((\omega_1+\omega_2)\cdot t+\varphi_1+\varphi_2)+\cos(\Delta\omega_{12}\cdot t+\varphi_1-\varphi_2)] \tag{5.2}$$

And from the same reasons as above, the output of the photodiode can be written as:

$$O_{PD}(t)=P_{DUT}+P_{LO}+A_{LO}A_{PD}\cdot\cos(\Delta\omega\cdot t+\Delta\tilde{\varphi}(t)) \tag{5.3}$$

With $\Delta\varphi(t)=\varphi_{DUT}(t)-\varphi_{LO}(t)$ and $\Delta\tilde{\varphi}(t)$ being the low pass filtered version of $\Delta\varphi(t)$, due to the detector bandwidth. It is obvious than that when the phase noise of the local oscillator is significantly lower then that of the laser under test, the resulting signal is an RF signal oscillating at $\Delta\omega=\omega_{LO}-\omega_{DUT}$ with the exact same noise process as the laser field. Analyzing that signal using conventional RF analysis tools will reveal information of the laser phase noise characteristics.

5.1.2 Homodyne measurement technique

In an homodyne scheme, as the one presented in figure 5.1b, the same laser under test is used also as a local oscillator. To gain information on the phase noise process, the laser is split into two arms, on one of which it is frequency shifted by ω_{RF} and delayed by τ. The delay is usually introduced as simply elongation of the arm length with respect to the other arm. Following Eq. (5.2), the resulting signal at the photodiode detector can be written as:

$$O_{PD}(t)=P_0+P_0cos(\underbrace{(\omega_0+\Omega)\tau}_{\phi}-\Omega t+\varphi(t)-\varphi(t-\tau)) \tag{5.4}$$

Using the Wiener-Khinchine theorem, we can show that the power spectral density of the photodiode autocorrelation signal is [26]:

$$\begin{aligned} S(\omega,\tau) =& \frac{\frac{1}{2}P_0^2\tau_c}{1+(\omega\pm\Omega)^2\tau_c^2}\cdot\left\{1-e^{-\frac{|\tau|}{\tau_c}}\left[\cos((\omega\pm\Omega)|\tau|)+\frac{\sin((\omega\pm\Omega)|\tau|)}{(\omega\pm\Omega)\tau_c}\right]\right\} \\ &+ P_0\pi e^{-\frac{|\tau|}{\tau_c}}\delta\left(\omega\pm\Omega\right) \end{aligned} \tag{5.5}$$

Hence, when the delay along one arm is much larger then the laser coherence time $\tau \gg \tau_c$, We are left with a Lorentzian line shape which is is determined by τ_c, and gives an estimation of the white frequency noise of the oscillator. When $1/f$ noise is also present, the resulting lineshape is a convolution of a Lorentzian and Gaussian lineshsapes, known as Voigt profile. given that profile, the white and flicker frequency noise components can be estimated approximately [27]. We note that though $1/f$ noise process is not strictly weakly stationary, using Wiener-Khinchine to determine the noise properties from its power spectral density does in effect yield meaningful results.

5.1.3 Extracting the phase noise of an RF signal

Tracking the phase of an oscillating signal in the presence of noise is a complicated task, as the nonlinear nature of the oscillation results in ambiguities of the actual phase of the oscillator. Several methods have bean proposed to detect the phase noise signal [28], the main being direct observation of the spectrum, Heterodyne / phase detector based schemes and frequency discriminator schemes. The first method, being the most simple, doesn't perform well in the presence of dominant $1/f$ noise close to the carrier, and cannot distinguish AM from PM noise. It is more usable when AM is less of a problem and the carrier frequency is locked and stable during the observation window. Here, a heterodyne method usually used for coherent demodulation of phase modulated signals is presented. In the general scheme the signal under test, assumed to be oscillating in a nominal frequency f_0, is mixed with two quadratures of the same oscillator at frequency f_n. Noting that:

$$\begin{aligned} &\cos(2\pi f_0 t+\varphi(t))\cdot\cos(2\pi f_n t+\phi_i) \\ &\qquad = \frac{1}{2}\left[\cos(2\pi(f_0-f_n)t+\varphi(t)-\phi_i)+\cancel{\cos(2\pi(f_0+f_n)t+\varphi(t)+\phi_i)}\right] \end{aligned} \tag{5.6}$$

The second term canceled as it can be filtered out. Thus, by properly choosing ϕ_i's (i.e. choosing $\phi_2 = \phi_1 + \pi/2$) we can get two quadratures of an oscillating signal at frequency $f_0 - f_n$ and with the same phase noise process. These two signals, called the Q and I quadratures signals, are then demodulated using the 4 quadratures inverse tangent function:

$$v(t) = \arctan\left(\frac{Q}{I}\right) = \mod(2\pi(f_0-f_n)t+\varphi(t)+\theta, 2\pi) \tag{5.7}$$

This scheme is insensitive to amplitude noise, as the amplitude related fluctuations exactly cancel out under the devision of the two quadratures. Further more, the phase ambiguity of an oscillating signal around the minima and maxima points are removed using the second quadrature, which exhibits linear phase response at these points. The output signal is mostly a linear function of time, wrapped 2π. Unwrapping the signal is a simple task, and after elimination of the linear phase trend corresponding to the angular frequency of $2\pi(f_0 - f_n)$, the underline phase noise process sample is revealed and statistics about it can be inferred by taking repetitive measurements.

5.2 Control theory and phase locked loops

Control theory is a field in engineering dealing with the control and stabilization of physical dynamic systems. It usually aims to regulate an otherwise disturbed or noisy system output by controlling

its input. If the control signal is generated by observing the physical system output, the scheme is referred to as "feedback" control, while if the control signal is generated by measuring a different system variables, it is referred to as "feed-forward" scheme. a PLL (Phase Locked Loop), is a specific kind of feedback scheme, aimed to regulate the output phase of a VCO (voltage controlled oscillator) with respect to the phase of a reference oscillator. Since a laser is itself a VCO, this scheme is useful in stabilizing the laser output frequency and reducing its phase noise. The description and characteristics of a PLL, along with a brief overview of linear system analysis is presented in the following sections. Further details can be found in [29][30].

5.2.1 Linear systems and transfer functions

We consider a general single input single output (SISO) system, where $x(t)$ and $y(t)$ are the input and output of the system, respectively. For a linear time invariant (LTI) system, the following general differential equation relates the system input and output:

$$\sum_{i=0}^{n} a_i y^{(n-i)}(t) = \sum_{j=0}^{n} b_j x^{(n-j)}(t) \tag{5.8}$$

Using the Laplace transform: $\mathcal{L}(f(t)) = \int_0^\infty e^{-st} f(t)dt$ we can transform the time derivative into a polynomial in s. Ignoring the system initial conditions, the system of Eq. (5.8) can be represented as:

$$Y(s)\sum_{i=0}^{n} a_i s^i = X(s)\sum_{j=0}^{n} b_j s^j \rightarrow \frac{Y(s)}{X(s)} = \frac{\sum_{j=0}^{n} b_j}{\sum_{i=0}^{n} a_i s^i} \equiv H(s) \tag{5.9}$$

The output response of the system to an input signal $x(t)$ can be realized by multiplication in the Laplace domain with the system transfer function $H(s)$, or by convolution:

$$y(t) = x(t) * h(t) \tag{5.10}$$

Where $h(t) = \mathcal{L}^{-1}(H(s))$ is the inverse Laplace transform of the system transfer function.
We can now consider noise process superimposed on the output. In Laplace domain this system looks like:

$$Y(s) = G(s)X(s) + N(s) \tag{5.11}$$

Such linear open loop system is described in figure 5.2a. To eliminate the noise we might adopt a feedback scheme, involving a controller with transfer function $C(s)$. In that case, the system is:

$$\begin{aligned} Y(s) =& G(s)\left(X(s) + C(s)Y(s)\right) + N(s) \\ \rightarrow Y(s) =& \frac{G(s)}{1 + G(s)C(s)}X(s) + \frac{1}{1 + G(s)C(s)}N(s) \end{aligned} \tag{5.12}$$

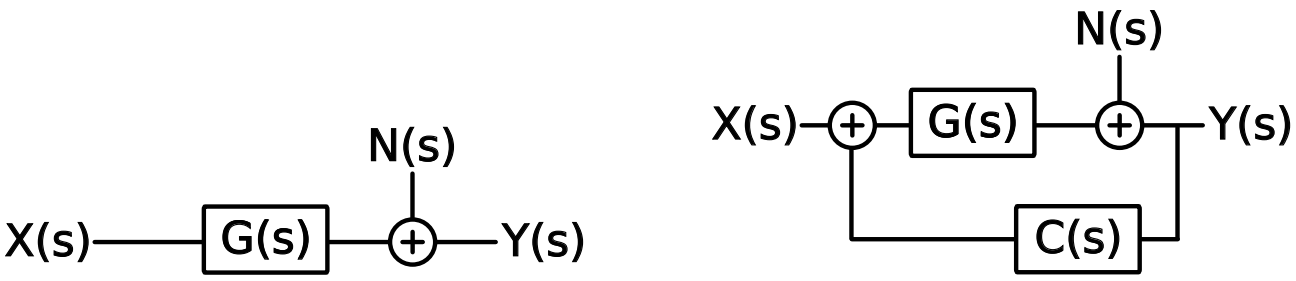

(a) Open loop system system

(b) Closed loop system scheme

Figure 5.2: An open and closed loop scheme. In a closed loop system the open loop output is injected back and determines the system input, hence the term feedback

The resulting transfer function for the signal and noise processes are called the closed loop transfer function and the error transfer function respectively. Since the controller is a system of our choice, its proper design is the key for obtaining the desired system performance and eliminating noise or other sources of error. For instance, in the limit of $G(s) \to \infty$, $Y(s) \to X(s)$ as desired.
To ensure a reliable operation of the system the stability of the closed loop transfer function must be considered. We notice that when $G(s)H(s) \to -1$, both the closed loop and error transfer function explode. Thus, a proper design of the controller should address this issue and verify that the transfer function is sufficiently distant from -1 for every frequency, where $s \to i\omega$. Noting that $-1 = 20 \cdot \log_{10}(0)e^{i\pi}$, two measures usually characterize the system stability: The first, called the gain margin of a system $F(s)$, is the system gain at the frequency ω_0 where $\arg(F(\omega_0)) = \pi$. The second term, the phase margin, is the excess phase with respect to π at ω_1, where ω_1 is the frequency at which $20 \cdot \log_{10}(F(\omega_2)) = 0$:

$$\begin{aligned} GM &= 20 \cdot \log_{10}(F(\omega_0)),\ \omega_0\ s.t.\ \arg(F(\omega_0)) = \pi \\ PM &= \pi - \arg(F(\omega_1)),\ \omega_1\ s.t.\ 20 \cdot \log_{10}(F(\omega_1)) = 0 \end{aligned} \tag{5.13}$$

A Bode plot is a plot of a system gain (in dB) and phase Vs. frequency. On this kind of plot the gain and phase margin can be graphically presented as the phase value at the zero dB gain crossing point and the gain value at the -180 phase crossing point.

5.2.2 A simple PLL model

A PLL feedback circuit on the output of a VCO, setting its average frequency equal to that of a reference oscillator. Though PLLs comes in different configurations, a simple PLL model is described for clarity. In a PLL circuit, the input variable is the phase of the reference oscillator $\theta_i(s)$, and the output is the the phase of the VCO $\theta_o(s)$. The additive noise that is superimposed on the VCO phase, that is not set by the control but rather by an inherent noise process, is labeled $\varphi(s)$. A scheme of such circuit is presented in figure 5.3. The PLL has three main components: the phase detector, the controller and the VCO.

- The Phase Detector: A phase detector, or sometimes frequency-phase detector, is a system whose linear response is proportional to the phase error $\theta_i - \theta_o \pmod{2\pi}$:

$$v_d = K_d\,(\theta_i - \theta_o) \tag{5.14}$$

  There exists a couple of physical realizations of a phase detector, the simplest is just a filtered mixer, as its output is an oscillating function of the phase that can be viewed as linear when the phase error remains small.

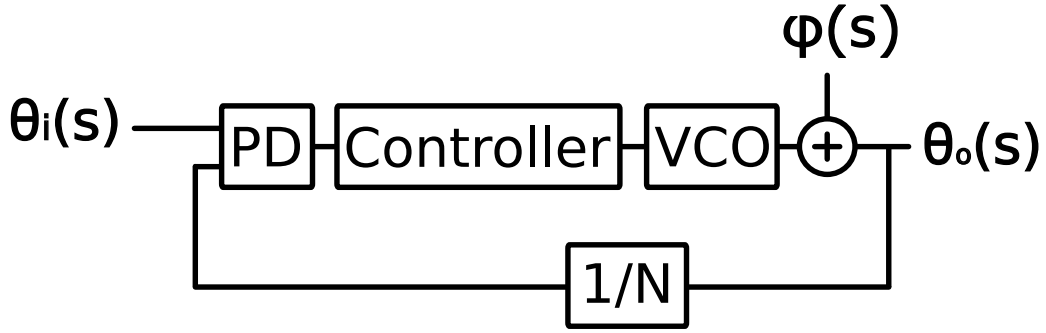

Figure 5.3: A PLL schematic model, showing the Phase detector (PD), loop controller, VCO and frequency divider

- The loop controller: The controller is the main component with which we design and implement the desired transfer function for both the noise and the signal. Its transfer function general structure and number of poles determines both the PLL order and Type. a general PLL is Type II (has two integrators) and order 2 (it's characteristic equation has two poles). A popular controller is the PID, with a proportional, integral and derivative gain of the input signal:

$$u(t) = k_p e(t) + k_i \int_0^t e(\tau)d\tau + k_d \frac{de(t)}{dt} \rightarrow U(s) = \left(k_p + \frac{k_i}{s} + k_d s\right) E(s) \tag{5.15}$$

  The intuition behind a PLL operation can be inferred from its time domain description. While the proportional part takes care of immediate phase error and corrects for it, the integral part produces an output corresponding to the accumulated phase error, in prospect of eliminating any steady state phase error and reduce possible errors oscillations. The derivative part is correcting for future errors, as estimated from the slope of the error signal, which will introduce a stronger response to more abrupt phase excursions.

- The Voltage Controlled Oscillator: as the name implies, the a VCO is an oscillator whose frequency can be tuned through changing the applied voltage on its control input. defining K_o as the voltage to frequency sensitivity of the VCO, and remembering that the output phase is an integral over the VCO frequency, we write:

$$v(t) = \int_{-\infty}^t K_o v_c(\tau)d\tau \rightarrow V(s) = \frac{K_o}{s} V_c(s) \tag{5.16}$$

  And so the basic VCO is just a phase integrator.

We note that this PLL order (which states the amount of integrators) is 2. The open loop transfer function is thus:

$$G(s) = \frac{\theta_0}{\theta_e} = \frac{K_d K_o}{s}\left[k_p + \frac{k_i}{s} + s k_d\right] \equiv \frac{K_d s^2 + K_p s + K_i}{s^2} \tag{5.17}$$

The closed loop function for the input phase and the noise in that case is:

$$\begin{aligned} H(s) =& \frac{\theta_o(s)}{\theta_i(s)} = \frac{G(s)}{1+G(s)} = \frac{K_d s^2 + K_p s + K_i}{(1+K_d)\, s^2 + K_p s + K_i} \\ E(s) =& \frac{\theta_o(s)}{\varphi(s)} = \frac{1}{1+G(s)} = \frac{s^2}{(1+K_d)\, s^2 + K_p s + K_i} \end{aligned} \tag{5.18}$$

5.2.3 Time and frequency analysis a PID transfer function

For simplicity, a system with $K_d = 0$ is further considered. Both the error and signal transfer function have the same denominator, called the characteristic equation. Since its an 2nd order equation, we can make the correspondence with a system with natural frequency ω_n and damping rate ζ:

$$H(s) = \frac{2\omega_n \zeta s + \omega_n^2}{s^2 + 2\omega_n \zeta s + \omega_n^2}, \qquad E(s) = \frac{s^2}{s^2 + 2\omega_n \zeta s + \omega_n^2} \tag{5.19}$$

Figure 5.4 depicts the frequency response gain of both transfer function, for normalized frequency and for various damping rates. These graphs illustrate the basic property of a phase locked loop - for frequencies below a certain threshold, the loop track the frequency modulation of the input phase, and attenuate noise. For higher frequencies, however, noise just pass through while the loop fails to track the input phase modulation. Thus, the loop behaves as a low pass filter for input phase modulation and high pass filter for noise modulation. This behavior is attributed to the fact that the PLL has a

finite bandwidth. This bandwidth limits the ability of the loop to track fast changes in input phase, and so limits the ability to correct for phase noise of high frequency.

Besides the frequency response of the PLL system, also the transient response should be considered, as it dictates the exact temporal way a PLL will respond to changes in the input. We can, for instance, consider the system response to a $\Delta\theta$ phase step:

$$\theta_o(s) = H(s)\frac{\Delta\theta}{s} = \frac{\Delta\theta}{s} - \frac{\Delta\theta s}{s^2 + 2\omega_n\zeta s + \omega_n^2} \tag{5.20}$$

The first part of the response correspond to the steady state response of the system. The second term, including the characteristic equation, determines the transient response, which decays with time. The decay time and behavior is fully dictated by the roots of the characteristic equation. Since these roots are $s_{1,2} = -\omega_n\zeta \pm \omega_n\sqrt[1]{\zeta^2 - 1}$, the transient response will look like:

$$\theta_0(t) \sim \cos\left(\sqrt{\zeta^2 - 1}\omega_n t\right)e^{-\zeta\omega_n t} - \frac{\zeta}{\sqrt{\zeta^2 - 1}}\sin\left(\sqrt{\zeta^2 - 1}\omega_n t\right)e^{-\zeta\omega_n t} \tag{5.21}$$

A damping parameter $\zeta < 1$ will introduce decaying oscillations into the transient response, and will exhibit an overshoot of the phase. On the other hand, a large decay will eliminate the oscillations, on the expense of a longer decay time due to the hyperbolic decays. Figure 5.5 shows the transient response to a step function for different damping parameters. By adequately tuning the controller, the two loop parameters are chosen as well, so one can attain a PLL with the transient specification needed.

5.2.4 Higher order Type 2 PLL

In reality (and specifically in our PLL implementation), PLLs might contain several additional poles besides those we considered in our basic type II 2nd order PLL. These poles might be due to the physical or parasitic behavior of one of the components inside the loop, like a modulation bandwidth for a VCO. Furthermore, these can be inserted deliberately as low pass filters along the way, to either filter-out high frequency components emanating from the phase detector, or simply to enlarge the gain

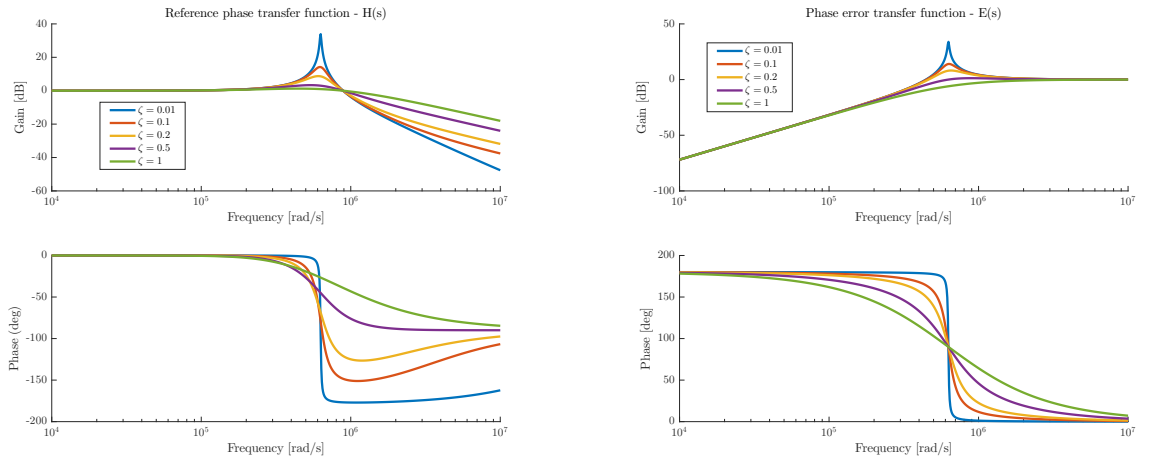

(a) Reference phase transfer function for different damping rates exhibiting a phase low pass filtering behavior

(b) VCO Phase noise transfer function for different damping rates exhibiting high pass filtering behavior

Figure 5.4: Bode plots for the reference phase and VCO phase noise showing the PLL tendency to follow the reference phase

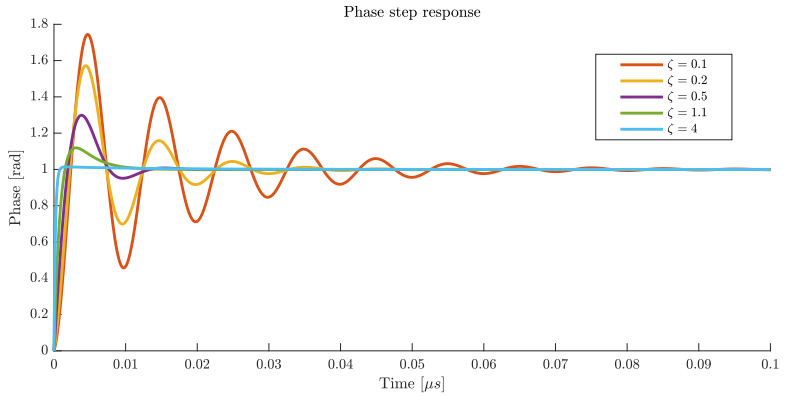

Figure 5.5: Transient response of a PLL with different damping coefficients to input phase step

roll-off of the open loop system.
We know that the closed loop response function is greatly determined by the open loop one, so it is important to realize the effect of additional poles on the transfer function. We know that the asymptotic plot of a pole is of $0dB$ gain up until the corner frequency, and a $-20dB/dec$ gain slope starting that frequency. Being so, poles that their corner frequency is far above the bandwidth of the loop, could be ignored, at least to first order, when considering the correct gains for a configuration of the loop. Parasitic poles which occur within the desired PLL bandwidth might limit it, and should be considered when designing the PLL.

Chapter 6

The trapped ion

An atomic clock is essentially an apparatus for extracting the frequency of an atomic oscillator. In our lab we trap ions and through coherent interaction perform various kinds of measurements with and on them. The ability to trap and cool the ion using optical and RF electrical fields had made it possible to perform spectroscopy in the recoil-free Lamb-Dicke regime, enabling narrow linewidth spectroscopy robust to some of the systematic frequency shifts inherent to other atomic reference systems. Spectroscopy of such system is very sensitive to the spectral content of the probing laser, a property we can use to measure and estimate the features of our laser. The following is a brief description of the physical realization of such trapped ion system, along with a derivation of the interaction dynamics of an ion with a classical laser field, and the spectroscopic tools it gives us.

6.1 A physical realization of a two level system

In our lab we work with strontium ions $[^{88}Sr^{+}]$. The strontium element is located at the second column of the periodic table, and after ionization it remains with one electron in its outer shell, making it an

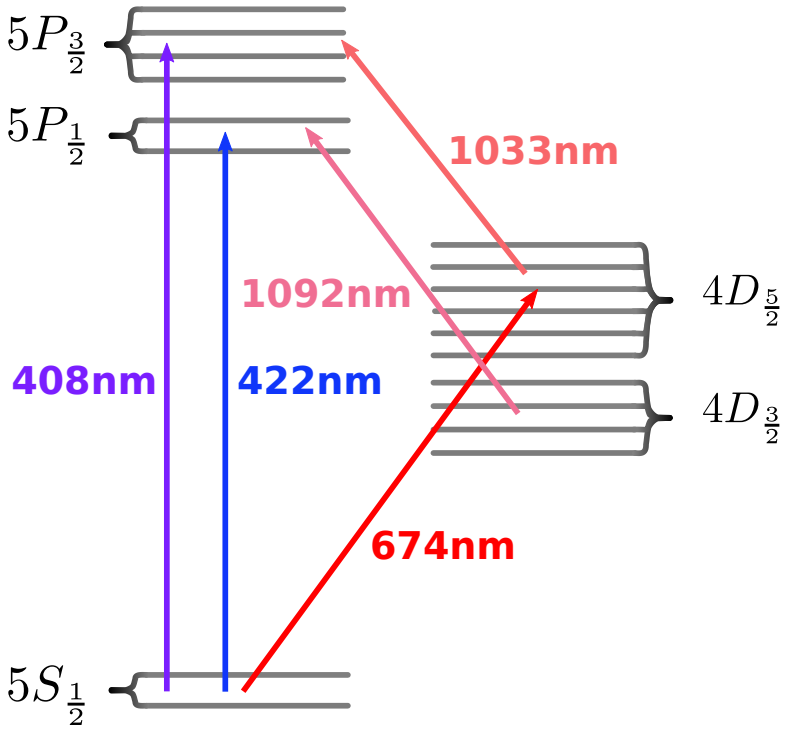

Figure 6.1: $^{88}Sr^{+}$ energy levels diagram

Hydrogen-like atom. The energy level diagram for $^{88}Sr^{+}$ is presented in figure 6.1. Two important features makes $^{88}Sr^{+}$ a good choice for trapped-ion kind of experiments, and specifically for optical clocks: first, the $\left|5S_{1/2}\right\rangle \rightarrow \left|4D_{5/2}\right\rangle$ transition is an optical narrow transition; It is an electric dipole forbidden and electric quadrupole allowed transition with a narrow linewidth and long lifetime of about 360 ms, making it a good optical reference transition. Second, all other lasers needed to actually trap, cool, initialize, re-pump the ion and detect its state are in the optical domain and can be somewhat simply generated using tabletop laser diode and optical systems.

6.1.1 Trapping and cooling an Ion

The ion, being an electrically charged particle, can be trapped using electric fields. Laplace's equation $\nabla^2\varphi = 0$ renders the trapping of an electric charge using only DC field impossible, and a Paul trap overcomes this difficulty by presenting oscillating voltages as part of the trap. The general form of such potential can be written as:

$$\phi(\vec{r},t) = \frac{V_{dc}^2}{2R_{dc}^2}\left(a_1x^2 + a_2y^2 + a_3z^2\right) + \frac{V_{RF}^2\cos(\Omega_{RF}t)}{2R_{RF}^2}\left(\tilde{a}_1x^2 + \tilde{a}_2y^2 + \tilde{a}_3z^2\right) \tag{6.1}$$

With $\sum_{i=1}^{3} a_i = \sum_{j=1}^{3} \tilde{a}_j = 0$ as implied from Laplace's equation. A popular configuration is the linear Paul trap, in which a DC potential is used to trap the ions along the trapping axis $\hat{z}$, and an RF potential traps the ion in the perpendicular plane. The RF potential is:

$$\Phi_{RF}(\vec{r},t) = \frac{V}{2}\cos(\Omega_{RF}t)\left(1 + \frac{x^2 - y^2}{R^2}\right) \tag{6.2}$$

Which, for a sufficiently high drive frequency creates an effective potential form a particle of charge q and mass m

$$\Phi_{eff} = \frac{m}{2q}\omega_r^2\left(x^2 + y^2\right) \tag{6.3}$$

Near the center of the trap, the static potential due to the end caps is

$$\Phi_s = \frac{m}{2q}\omega_z^2\left(z^2 - \frac{1}{2}\left(x^2+y^2\right)\right) \tag{6.4}$$

Where the trap secular frequency ω_z is determined by the geometrical and other electrical properties of the trap. The overall effective potential is a 3D confining potential:

$$\Phi_z = \frac{m}{2q}\omega_z^2 z^2, \quad \Phi_r = \frac{m}{2q}\left(\omega_r^2 - \frac{1}{2}\omega_z^2\right)z^2 \tag{6.5}$$

Further description of the trapping potential, as well as derivation of the ion motion inside the trap and its parametric regions of stable trapping can be found in [31][32].
Being trapped by the electric field pseudo-harmonic potential, the ion has to be cooled down to the motional and internal ground state. To cool the motional degrees of freedom, a Doppler cooling scheme is applied, where a red-detuned 422 nm wavelength laser is applied in two counter propagating directions of the ion. Before cooling begins the ion usually travels at large velocities corresponding to hundreds of K, so its motion can be described classically. Doppler effect further shifts the light red-detuned frequency, so that when it travels towards the laser source it shifts the light frequency closer to the $\left|5S_{1/2}\right\rangle \rightarrow \left|5P_{1/2}\right\rangle$ resonance, making it more plausible for the ion to absorb a photon. The momentum quanta transfered by the absorbed photon then reduces the momentum of the ion. The effective force the ion experiences by these two lasers can be derived for small velocities [33]:

$$F = \frac{\hbar k^2 \gamma^3}{2}\frac{\Delta}{[\Delta^2 + (\gamma/2)^2]^2}\frac{I}{I_{sat}}v \tag{6.6}$$

With γ the natural linewidth and Δ the laser red-detuning. This cooling scheme is limited by the fluctuating force induced from the spontaneous emission of photons to random directions, and the Doppler temperature limit $T_D = \frac{\hbar\gamma}{2k_B}$ amounts to about 1 mK for our ion, corresponding to harmonic trap potential occupation of about $\langle n\rangle \simeq 10$.

6.1.2 State initialization and detection

We initialize our ion in one of the two $\left|5S_{1/2}, m = \pm 1/2\right\rangle$ states. This is done by what called optical pumping, a scheme in which optical fields couples only one of the low energy states to an excited state in the atom, leading to the incoherent accumulation of population in the other low energy dark state through decay. In our case, we couple the $\left|5S_{1/2}\right\rangle \rightarrow \left|5P_{1/2}\right\rangle$. We used σ^+ or σ^- polarized light to couple only one of the two Zeeman levels, so that population at this level is transfered into the excited P state. The short P lifetime induces fast spontaneous decay to the two Zeeman S levels. This kind of scheme ensures that after a long time (compared to the excited state decay rate) the excited state population is accumulated at the uncoupled ground Zeeman level. When excited to the $\left|5P_{1/2}\right\rangle$ level, the ion has a small probability of decaying to the $\left|4D_{3/2}\right\rangle$ manifold, possibly transferring some of the population to a different state. To overcome this problem, a pump laser coupling the $\left|4D_{3/2}\right\rangle \leftrightarrow \left|5P_{1/2}\right\rangle$ at wavelength 1092 nm is operated at all times, making sure that that $\left|4D_{3/2}\right\rangle$ remains empty.
To detect the state of the ion after its interaction with the narrow linewidth laser, we perform a scheme of state selective florescence [34]. We take advantage of the long lifetime of the $\left|4D_{\frac{5}{2}}\right\rangle$ manifold, and couple the $\left|5S_{\frac{1}{2}}\right\rangle \leftrightarrow \left|5P_{\frac{1}{2}}\right\rangle$ states. Being very short lived excited state, high rate photon isotropic scattering starts as soon as the $|S\rangle \rightarrow |P\rangle$ coupling starts to coherently excite the $|P\rangle$ level. Before detection, the ion is assumed to be in some coherent superposition of $|S\rangle$ and $|D\rangle$, following the coherent interaction with the 674 nm laser. When the 422 nm laser is turned on and the detector

starts to capture scattered photons, the ion state collapses into either $|S\rangle$ or $|D\rangle$, according to the generated superposition. If the ion collapsed into $|D\rangle$, there would be no population in $|S\rangle$ to couple to the $|P\rangle$, and generally no photons will scatter or be detected. On the other hand, if the ion collapsed to the $|S\rangle$ state the $|S\rangle \leftrightarrow |P\rangle$ will yield many scattered photons, that would be detected by the photon detector.

6.2 Ion-light interaction and spectroscopy

6.2.1 Theoretic description

We consider the interaction of our ion, described as a two level system trapped in an harmonic potential, with a classical electromagnetic field, generated by laser radiation. The most simple Hamiltonian for such system is:

$$\mathcal{H} = H_0 + V_{int} = \hbar\omega \left|e\right\rangle\!\left\langle e\right| + \hbar\omega_t\left(\hat{a}^\dagger\hat{a} + \frac{1}{2}\right) + V_{int} \tag{6.7}$$

Here $\omega = \omega_e - \omega_g$ corresponding to the energy difference of the ground and excited state, ω_t is the harmonic trap frequency and $\hat{\sigma}_i$'s are the Pauli operators. For our purpose, since the laser detuning from the atomic resonance will be smaller then the energy associated with the trap $\delta = \omega_l - \omega << \omega_t$, we will disregard the harmonic trap potential for the rest of the derivation. The interaction part of the Hamiltonian is due to the presence of the plane-wave, for which:

$$\begin{aligned} V_{int} = \frac{e\mathbf{A}\cdot\mathbf{p}}{m_e} \propto eA_0 e^{i(\mathbf{kx}-\omega_l t)}\epsilon\cdot\mathbf{p} =& eA_0 e^{-i\omega_l t}\epsilon\cdot\mathbf{p}[1 + i\mathbf{kx} + \ldots] \\ \simeq& eA_0 e^{-i\omega_l t}\left[\epsilon\cdot\mathbf{p} + \frac{i}{2}((\mathbf{k}\times\epsilon)\cdot(\mathbf{x}\times\mathbf{p}) + k_m\epsilon_n Q_{mn})\right] \end{aligned} \tag{6.8}$$

With $Q_{mn} = x_m x_n - \frac{1}{3}x^2\delta_{mn}$ the electric quadrupole tensor, and the first two terms are the dipole electric and magnetic coupling moments. Since in our case we couple the S and D level, both with the same parity, the leading electric dipole interaction and the following magnetic dipole interaction don't contribute to the effective coupling. The resulting interaction described as [33]:

$$V_{int} = \frac{eA_0 k}{2} x\epsilon\cdot\mathbf{x}\left[ie^{-i\omega_l t} + c.c.\right] \equiv \frac{\hbar\Omega}{2}\left(\hat{\sigma}^+ + \hat{\sigma}^-\right)\left[e^{-i(\omega_l t + \frac{\pi}{2})} + c.c.\right] \tag{6.9}$$

Where $\Omega = \frac{eA_0 k}{\hbar}\left\langle S\right|x\epsilon\cdot\mathbf{x}\left|D\right\rangle$ and the $\hat{\sigma}^\pm$ are the usual raising and lowering operators in the SD subspace. To simplify the dynamics we apply the transformation into the interaction picture, with $U = e^{\frac{i}{\hbar}H_0 t}$, and use the rotating wave approximation to eliminate fast oscillating terms:

$$\begin{aligned} H_I \to UH_IU^\dagger =& \frac{\hbar\Omega}{2}\left(e^{i\omega t|1\rangle\!\langle 1|} + |0\rangle\!\langle 0|\right)\left(\hat{\sigma}^+ + \hat{\sigma}^-\right)\left[e^{-i(\omega_l t+\frac{\pi}{2})} + e^{i(\omega_l t+\frac{\pi}{2})}\right]\left(e^{-i\omega t|1\rangle\!\langle 1|} + |0\rangle\!\langle 0|\right) \\ =& \frac{\hbar\Omega}{2}\left(\hat{\sigma}^+ e^{i\omega t} + \hat{\sigma}^- e^{-i\omega t}\right)\left[e^{-i(\omega_l t+\frac{\pi}{2})} + e^{i(\omega_l t+\frac{\pi}{2})}\right] \\ \xrightarrow{RWA}& \frac{\hbar\Omega}{2}\left(\hat{\sigma}^+ e^{i(\omega-\omega_l)t} + \hat{\sigma}^- e^{-i(\omega-\omega_l)t}\right) \end{aligned} \tag{6.10}$$

We consider our general quantum state $|\psi\rangle = c_g\left|g\right\rangle + c_e\left|e\right\rangle$ (defining $|S\rangle \equiv |g\rangle$ and $|D\rangle \equiv |e\rangle$ for consistency with usual notation) and derive the Schrödinger equations of the interaction picture dynamics, with the former transformation $U = e^{i\omega t|1\rangle\!\langle 1|}$ and $\left|\tilde{\psi}\right\rangle = U\left|\psi\right\rangle$:

$$\begin{aligned} i\hbar\partial_t\left(U^\dagger\left|\tilde{\psi}\right\rangle\right) =& HU^\dagger\left|\tilde{\psi}\right\rangle \quad /\cdot U \\ \to i\hbar\partial_t\left|\tilde{\psi}\right\rangle =& \left[UHU^\dagger + i\hbar(\partial_t U)U^\dagger\right]\left|\tilde{\psi}\right\rangle = \left[\hbar\omega\left|1\right\rangle\!\left\langle 1\right| + H_I - \hbar\omega\left|1\right\rangle\!\left\langle 1\right|\right]\left|\tilde{\psi}\right\rangle = \tilde{H}_I\left|\tilde{\psi}\right\rangle \end{aligned} \tag{6.11}$$

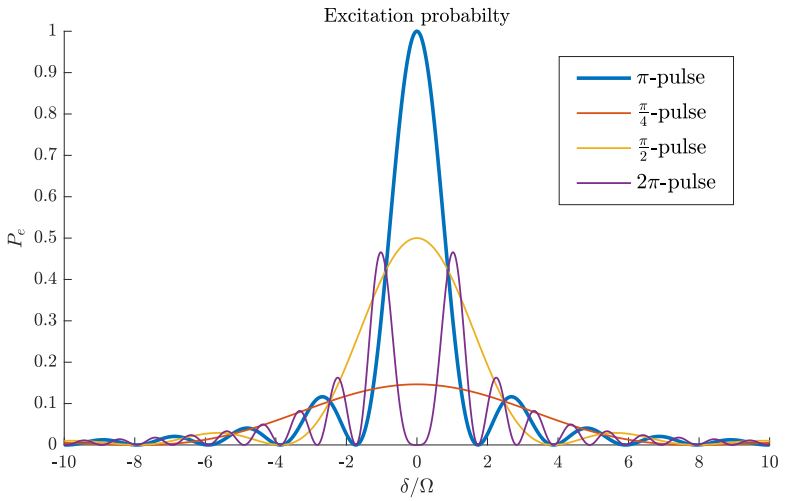

Figure 6.2: Excitation probability for the two level system Vs. the exciting field detuning, for various excitation times

In the interaction picture $U|\psi\rangle = c_g|g\rangle + c_e e^{i\omega t}|e\rangle \equiv c_g|g\rangle + \tilde{c}_e|e\rangle$. We can now write the equations for the two amplitudes:

$$\hbar\partial_t\left|\tilde{\psi}\right\rangle = \tilde{H}_I\left|\tilde{\psi}\right\rangle = \frac{\hbar\Omega}{2}\left[e^{i\delta t}c_g|e\rangle + e^{-i\delta t}\tilde{c}_e|g\rangle\right] \begin{cases} \langle g|: & i\dot{c_g} = \frac{\Omega}{2}e^{-i\delta t}\tilde{c}_e \\ \langle e|: & i\dot{\tilde{c}}_e = \frac{\Omega}{2}e^{i\delta t}c_g \end{cases} \tag{6.12}$$

Assuming our two level system began at the ground state, these coupled differential equations has the following solution:

$$\begin{aligned} c_g(t) =& e^{i\frac{\delta}{2}t}\left(\cos\left(\frac{\tilde{\Omega}}{2}t\right) - i\frac{\delta}{\tilde{\Omega}}\sin\left(\frac{\tilde{\Omega}}{2}t\right)\right) \\ \tilde{c}_e(t) =& -i\frac{\Omega}{\tilde{\Omega}}e^{\frac{\delta}{2}t}\sin\left(\frac{\tilde{\Omega}}{2}t\right) \end{aligned} \tag{6.13}$$

These equations for the dynamics of the two levels amplitude describe an oscillation at frequency $\tilde{\Omega} = \sqrt{\Omega^2 + \delta^2}$ called the "generalized Rabi frequency", which goes to the Rabi frequency Ω in the $\delta \ll \Omega$ limit. The population of the excited state:

$$P_e(t) = \tilde{c}_e^*\tilde{c}_e = \frac{1}{1+\frac{\delta^2}{\Omega^2}}\left(\frac{1}{2} - \frac{1}{2}\cos\left(\tilde{\Omega}t\right)\right) \tag{6.14}$$

In the low detuning limit $\Omega \gg \delta$ we perform full oscillations at nearly the Rabi frequency. We notice that when $\Omega t = \pi$, the excited state population is

$$P_e\left(\frac{\pi}{\tilde{\Omega}}\right) = \frac{1}{1+\delta^2/\Omega^2} \xrightarrow{\Omega\gg\delta} 1 \tag{6.15}$$

These kind of pulses are called π-pulses and they are used in spectroscopy to find the zero detuning frequency. Figure 6.2 shows the excitation probability Vs. detuning for different pulse areas.

Density matrix representation and Bloch sphere

The density matrix representation of the two level state in the rotating frame is

$$\tilde{\rho} = \left|\tilde{\psi}\right\rangle\left\langle\tilde{\psi}\right| = \begin{pmatrix} \tilde{c}_e^*\tilde{c}_e & c_g^*\tilde{c}_e \\ \tilde{c}_e^*c_g & c_g^*c_g \end{pmatrix} \tag{6.16}$$

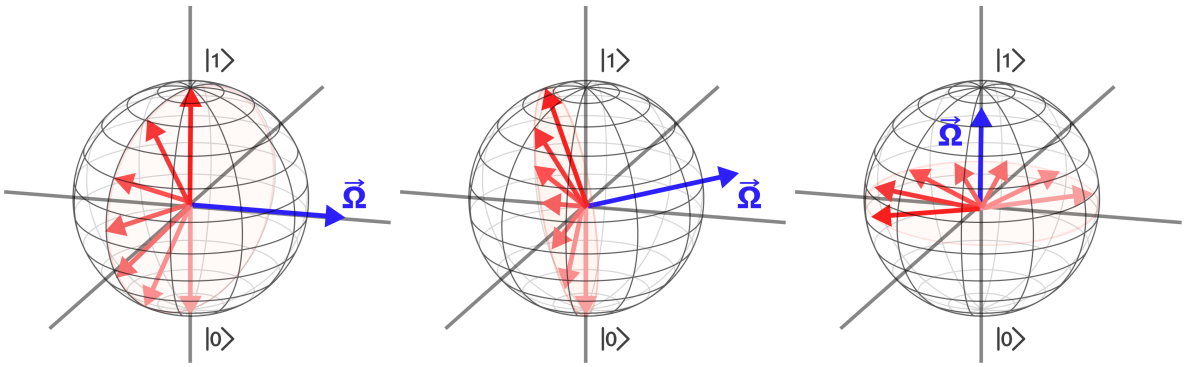

(a) Rabi oscillation with zero detuning

(b) Rabi oscillation with some detuning

(c) Phase accumulation in a detuned frame of reference

Figure 6.3: Bloch sphere representation for the two level system and light interaction. The precessing vector represents the Bloch state of the two level system. The Ω vector determines the precession orientation

and it evolves according to:

$$\partial_t \tilde{\rho} = -\frac{i}{\hbar}\left[\tilde{H}_I, \tilde{\rho}\right] \rightarrow \begin{cases} \partial_t \tilde{\rho}_{ee} = i\frac{\Omega}{2}\left(\tilde{\rho}_{eg} - \tilde{\rho}_{ge}\right) \\ \partial_t \tilde{\rho}_{gg} = -i\frac{\Omega}{2}\left(\tilde{\rho}_{eg} - \tilde{\rho}_{ge}\right) \\ \partial_t \tilde{\rho}_{ge} = -i\delta\tilde{\rho}_{ge} - i\frac{\Omega}{2}\left(\tilde{\rho}_{ee} - \tilde{\rho}_{gg}\right) \\ \partial_t \tilde{\rho}_{eg} = i\delta\tilde{\rho}_{ge} + i\frac{\Omega}{2}\left(\tilde{\rho}_{ee} - \tilde{\rho}_{gg}\right) \end{cases} \tag{6.17}$$

We can adopt a convenient perspective of this system and view the dynamics of the expectation values of the three Pauli operators:

$$\begin{aligned} \langle\hat{\sigma}_x\rangle &= \mathrm{Tr}\{|g\rangle\langle e|\,\tilde{\rho}\} + \mathrm{Tr}\{|e\rangle\langle g|\,\tilde{\rho}\} = \tilde{\rho}_{eg} + \tilde{\rho}_{ge} \\ \langle\hat{\sigma}_y\rangle &= i\,\mathrm{Tr}\{|g\rangle\langle e|\,\tilde{\rho}\} - i\,\mathrm{Tr}\{|e\rangle\langle g|\,\tilde{\rho}\} = i(\tilde{\rho}_{eg} - \tilde{\rho}_{ge}) \\ \langle\hat{\sigma}_z\rangle &= \mathrm{Tr}\{|e\rangle\langle e|\,\tilde{\rho}\} - \mathrm{Tr}\{|g\rangle\langle g|\,\tilde{\rho}\} = \tilde{\rho}_{ee} - \tilde{\rho}_{gg} \end{aligned} \tag{6.18}$$

Plugging in Eq. 6.17 governing the time evolution of the density matrix we get:

$$\left.\begin{aligned} \partial_t\langle\hat{\sigma}_x\rangle &= \delta\langle\hat{\sigma}_y\rangle \\ \partial_t\langle\hat{\sigma}_y\rangle &= -\delta\langle\hat{\sigma}_x\rangle - \Omega\langle\hat{\sigma}_z\rangle \\ \partial_t\langle\hat{\sigma}_z\rangle &= \Omega\langle\hat{\sigma}_y\rangle \end{aligned}\right\} \rightarrow \partial_t\langle\hat{\sigma}\rangle = \vec{\Omega}\times\langle\hat{\sigma}\rangle \tag{6.19}$$

$\langle\hat{\sigma}\rangle$ is called the Bloch vector, and its dynamics is of a precession about the vector $\vec{\Omega} = \Omega\hat{x} - \delta\hat{z}$. Since its size is a constant of motion under this kind of evolution, it defines a sphere called the Bloch sphere. A couple of useful visualizations are presented in figure 6.3. The first frame describes on-resonance Rabi oscillations, the Bloch vector precesses about $\vec{\Omega} = \Omega\hat{x}$ and the population inversion $\rho_{ee} - \rho_{gg}$ oscillates from 1 to -1 at an angular frequency Ω. In the second frame a detuning was added, the Bloch vector oscillates at frequency $\tilde{\Omega} = \sqrt{\Omega^2 + \delta^2}$ about the Rabi vector and does not reach the upper pole corresponding to maximal excitation probability. In the third there is no field coupling, but the detuning δ exists. The Bloch vector, here presented to be on the equator, precesses at rate δ around the $\hat{z}$ axis, due to the relative phase accumulation of the ground and excited state.

6.2.2 Spectroscopic tools

The coherent operations described above are strongly dependent on the laser detuning from the atomic resonance. We can use these as tools to estimate the resonance properties of our laser and of the Ion.

Rabi spectroscopy

Rabi spectroscopy is a method for finding the resonance frequency of the atomic system, by performing excitation pulses while scanning the laser frequency. Following Eq. (6.13) and (6.14), when we perform an on resonance π-pulse we excite our atom with probability $\to 1$. The excitation probability decrease with the detuning as presented in figure 6.2, and the spectral width of the excitation Vs. detuning graph can be helpful in determining the laser-ion combined phase noise process. From the two equations we learn that the detuning becomes significant as we lower our Rabi frequency. We can also think of the spectral broadening induced by the finite pulse time. Our oscillating laser field is a windowed oscillation function, which can be spectrally described (ideally) as two spikes at the nominal oscillation frequency ω_l, convolved with the spectral content of a time window $W_\tau(t) = \Theta(t) - \Theta(t-\tau)$ which is:

$$\mathcal{F}\left\{W_\tau(t)\right\} = \int_{-\infty}^{\infty} W_\tau(t) e^{i2\pi f t} dt = \tau e^{i\pi f \tau} \frac{\sin \pi f \tau}{\pi f \tau} \tag{6.20}$$

Which is the sinc function, with spectral width determined by τ. A numerical estimation of the main sinc lobe width gives the relation:

$$w = 2 \cdot f_{1/2} = \frac{2 \cdot 1.39}{\pi} \cdot \frac{1}{\tau} \simeq 0.89 \cdot \frac{1}{\tau} \tag{6.21}$$

We conclude that the width of the spectroscopic measurement is determined by $1/\tau$ whenever it is short compared to the spectral width of our laser oscillator. For long enough times the time window induced width will vanish, and the width of the main lobe will correspond to the characteristics of the laser-ion phase noise.
To obtain the dynamic equations for the population terms in the presence of de-coherence noise we use the Lindbladian formalism and add to Eq. (6.17) the decoherence operator $\gamma\sigma_z$ as a Lindblad super-operator $\gamma(\sigma_z \rho \sigma_z - \rho)$. The resulting dynamical equations for the Bloch variables are similar to those in Eq. (6.19) only with the new de-coherence term. When put into a matrix form:

$$\begin{pmatrix} \langle \dot{\sigma}_x \rangle \\ \langle \dot{\sigma}_y \rangle \\ \langle \dot{\sigma}_z \rangle \end{pmatrix} = \underbrace{\begin{pmatrix} -2\gamma & \delta & 0 \\ -\delta & -2\gamma & -\Omega \\ 0 & \Omega & 0 \end{pmatrix}}_{\mathbf{Q}} \begin{pmatrix} \langle \sigma_x \rangle \\ \langle \sigma_y \rangle \\ \langle \sigma_z \rangle \end{pmatrix} \tag{6.22}$$

To solve this equation we can turn to Laplace domain. Writing:

$$\mathcal{L}[\langle \vec{\sigma} \rangle] = \frac{1}{s - \mathbf{Q}} \langle \vec{\sigma} \rangle_0 \tag{6.23}$$

We can some time exactly solve for certain conditions and assumption. In our case, for $\langle \sigma_z(0) \rangle = -1$ and $\Omega \gg 2\gamma \gg \delta$ (The strong drive and low detuning regime, starting at the ground state) we get the following expression:

$$\begin{aligned} \mathcal{L}[\langle \sigma_z \rangle] = \frac{s + 2\gamma}{s^2 + 2\gamma s + \Omega^2} \to \langle \sigma_z(t) \rangle &= -e^{-\gamma t} \cos\left(\sqrt{\Omega^2 + \gamma^2}\right) - \frac{\gamma}{2\sqrt{\Omega^2 + \gamma^2}} e^{-\gamma t} \sin\left(\sqrt{\Omega^2 + \gamma^2} t\right) \\ &\simeq e^{-\gamma t} \cos\left(\sqrt{\Omega^2 + \gamma^2}\right) \end{aligned} \tag{6.24}$$

The ground state population can be than expressed as:

$$\rho_{gg}(t) = \frac{1 - \langle \sigma_z(t) \rangle}{2} \simeq \frac{1}{2} - \frac{e^{-\gamma t} \cos\left(\sqrt{\Omega^2 + \gamma^2}\right)}{2} \tag{6.25}$$

Ramsey spectroscopy

A different method for characterization of the laser phase noise is Ramsey spectroscopy. This method is sensitive to the relative phase between the ion and laser. In the basic Ramsey scheme, a short $\pi/2$-pulse of Rabi frequency $\Omega \gg \delta(t)$ drives the atom, initially at the ground state, to a superposition of the form:

$$|\psi\rangle_0 = \frac{1}{\sqrt{2}} \left[|g\rangle + e^{-i\phi} |e\rangle \right] \tag{6.26}$$

Next, the ion is allowed to freely evolve for time T, in which its state rotates around the Rabi vector $\vec{\Omega} = \delta(t)\hat{z}$. The Bloch vector phase at time T is an accumulation of the laser-ion detuning:

$$|\psi\rangle_T = \frac{1}{\sqrt{2}} \left[|g\rangle + e^{-i\left(\phi + \int_0^T \delta(t)dt\right)} |e\rangle \right] \tag{6.27}$$

At the end, another strong $\pi/2$-pulse is applied, brining the system to the state:

$$|\psi\rangle_f = \frac{1}{2} \left[|g\rangle + e^{-i\phi_f} |e\rangle + e^{-i\left(\phi + \int_0^T \delta(t)dt\right)} (|g\rangle - e^{-i\phi_f} |e\rangle) \right] \tag{6.28}$$

And the probability to be in the excited state is:

$$P_e(T) = |C_e|^2 \simeq \sin\left(\frac{\phi + \int_0^T \delta(t)dt}{2} \right) \tag{6.29}$$

When $\delta(t) \equiv \delta$ a constant detuning, the integral correspond to a linear phase accumulation process, and the excitation probability will oscillate coherently with time. These oscillations are referred to as Ramsey fringes. Whenever $\delta(t)$ is a random process the spectrum of the oscillating probability function widens, corresponding to the statistical properties of the noise process. When averaged over many realizations, $\langle P_e(T) \rangle$ exhibits a contrast decay corresponding to the inverse of its power spectral density. Adopting the definition for the coherence time according to [35] we define:

$$\Delta\tau = \int_{-\infty}^{\infty} P_e(t) P_e(t+T) dT dt = \frac{\pi}{\Delta\omega} \tag{6.30}$$

Where $\Delta\tau$ is the coherence time and defined as a measure of the excitation probability auto-correlation function decay rate (when we perform on resonance scan $\langle \delta \rangle = 0$), and $\Delta\omega$ is the spectral width or the excitation probability power spectral density function. We can measure the decoherence rate of our Ramsey oscillations to find out the spectral width of the ion-laser phase noise process.
If the ion-laser phase noise is dominantly influenced by magnetic field noise modulating the level energy separation through first order Zeeman effect, the fringes decay time will not correspond to laser-induced noise. To overcome such a limitation a Magnetic Field Dynamic Decoupling scheme (MFDD) can be carried out while performing Ramsey spectroscopy, to eliminate magnetic field related phase noise. This process, described in [36] involves a series of echo (π) pulses, performed within either the D or S manifolds. This kind of pulses transfers coherently the entire population from $|S, m_s\rangle$ ($|D, m_d\rangle$) state to $|S, -m_s\rangle$ ($|D, -m_d\rangle$). Considering the magnetic susceptibility of the optical transition:

$$\chi(\left|5S_{1/2}, m_S\right\rangle \rightarrow \left|4D_{5/2}, m_D\right\rangle) = -2.802 \cdot m_s + 1.68 \cdot m_D \quad [\text{MHz/G}] \tag{6.31}$$

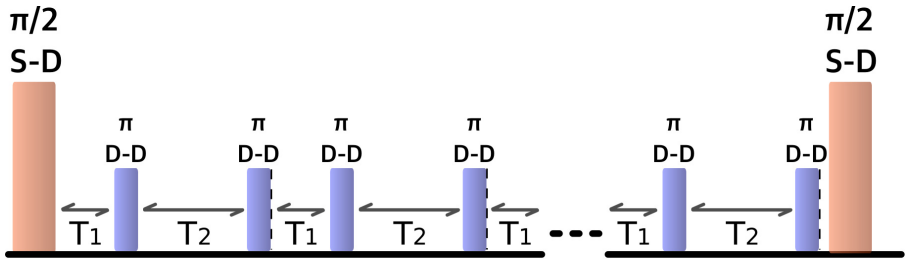

Figure 6.4: Ramsey spectroscopy scheme involving MFDD. pulses time ratio are chosen such that it will match the susceptibility ratio of the optical transitions

A proper choice of m levels coupling will yield an inversion of the susceptibility and consequently of the phase accumulation rate. Whenever such π-pulse is performed, phase accumulation due to magnetic field noise reverses its direction and start decreasing. if pulse times are chosen such that the time in between pulses ratio the magnetic susceptibility ratio are matched:

$$\frac{T_{m_s,m_{d,1}}}{T_{m_s,m_{d,2}}} = \frac{\chi_{m_s,m_{d,2}}}{\chi_{m_s,m_{d,1}}} \tag{6.32}$$

The magnetic field phase noise exactly cancels after each such two π-pulses period. This method can be used to obtain the decoherence rate eliminating magnetic σ_z phase noise, enabling a better appreciation of the laser properties.

Part II

Experimental setup and results

Chapter 7

Experimental setup

7.1 674 Laser phase stabilization

As the general method of reducing the linewidth of a ECDL lasing at 674.025nm, and motivated by Eq. (4.6), we chose to stabilize the beat frequency of the 674 diode and one of the frequency comb tooth, while its repetition rate is being optically locked to a narrow linewidth laser at 1560nm. I refer from this point on to the 1550nm cavity stabilized narrow linewidth laser as the *stable laser*, the laser emitted from the frequency comb apparatus around different carrier wavelengths as the *comb XXXnm laser*, and the 674 nm ECDL we wish to stabilized as the *clock laser*. More so, when using a different 674 nm laser, which is cavity stabilized in a different lab, for comparison and measurements, I will refer to that laser as the *probe laser*.
The following is the detailed description of the optical and electronic setup.

7.1.1 Laser phase stability transfer scheme

The optical setup for transferring the stability of the stable laser to the clock laser is presented in figure 7.1. The stable laser output of about 10mW power is split with a fiber coupled 90/10 beam splitter. We then take the 1mW into a fiber coupled beat detection unit (BDU), which is part of the comb setup. On the comb side, we take the output radiation at 1550nm from the comb output port, into an optical fiber and to the other port of the 1550nm BDU. The BDU then outputs the beat signals of the two lasers, which we lock to a DDS reference frequency in a PLL scheme implemented by Menlo system as part of the comb electronics. The comb also has an inherent $f-2f$ interferometer module, with which we lock the carrier envelope offset frequency, as described in 4.3.1.
The clock laser is generated from a laser diode (Toptica #LD-0675-0030-1), in an ECDL configuration (Toptica DL-pro ECDL). After leaving the ECDL, it propagates through an optical isolator and a prism pair, to correct for the asymmetric divergence angle of the emitted laser beam. It then goes through a $\lambda/2$ wave-plate and a polarization beam splitter cube, which splits the optical path into two lines - one for an upcoming experiment, and the other for locking, wavelength meter and to the remote trapped ion lab with an optical fiber. The split light is then split again on a 50/50 cube, taking

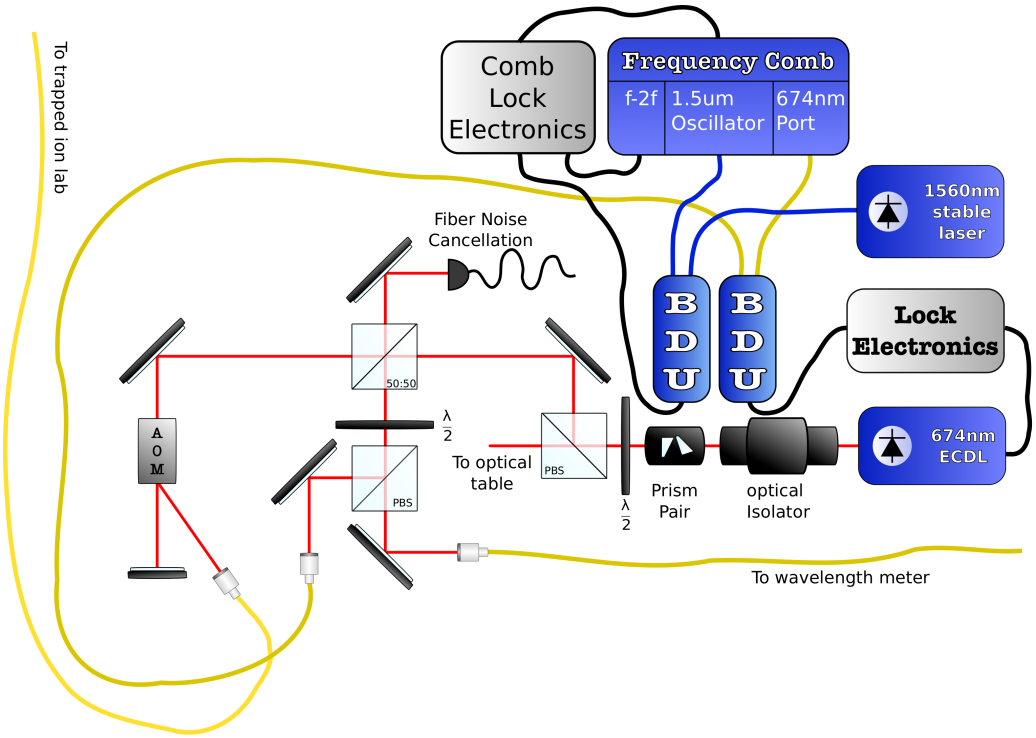

Figure 7.1: Optical scheme for phase stability transfer

half of the power to the remote lab. The remaining light then goes through another $\lambda/2$ polarization beam splitter cube, this time to adjust the light going into the wave meter and to the locking scheme. The wave meter (HighFinesse WS-10U) is a Fizeau interferometer able to measure the laser frequency with a ~ 1 MHz resolution, and is can be used for e.g. determination of the exact comb tooth number which is spectrally closest to the clock laser. About 1 mW is coupled into a fiber and enters a 674 nm BDU. On the other hand, some of the comb laser is split and coherently converted to 674 nm by a non-linear optical process. The resulting comb 674 nm light is again fed into a fiber which connects to the 674 nm BDU port. The BDU output is then connected to the electronic circuit to produce the error signal, which in turn fed into the laser dedicated port, for correction of the laser phase.

7.1.2 Laser locking electronics

The electronic PLL scheme used for phase locking the 674 nm laser to one of the comb tooth is presented in figure 7.2. The beat note signal is fed into an electronic module made by Menlo system. It is first filtered by a 105 MHz low pass filter, attenuating the beat note of the clock laser with different comb teeth. Since the comb repetition rate is ~250 MHz, we are assured that the more distant teeth beat notes will be outside of the filter pass band. Next, the signal is amplified and split in a 1:100 ratio. One fraction is used as a monitor port, and the rest is fed into an electronic circuit which was designed as part of this work. First, the signal is fed into a low phase noise amplifier (linear LTC6957-1) which converts the sine wave into a logic signal, without degrading the phase noise of the original beat note. It is then fed into a low phase noise integer synthesizer with frequency phase detector (Analog Devices HMC440QS16G). It first divides the signal by 7 and compare its phase with a reference signal, a 10 MHz atomic clock signal generated by a GPS receiver. A detailed description of the phase frequency detector (PFD) is given in next section. The two output of the PFD is then filtered for removing residual 10 MHz frequency emerging from the PSD. The filtered phase/ frequency error signal is now split and fed into three low noise amplifiers (Texas Instruments THS403l), connected in a tunable P, I and D configuration. It is then summed using a tunable summing amplifier configura-

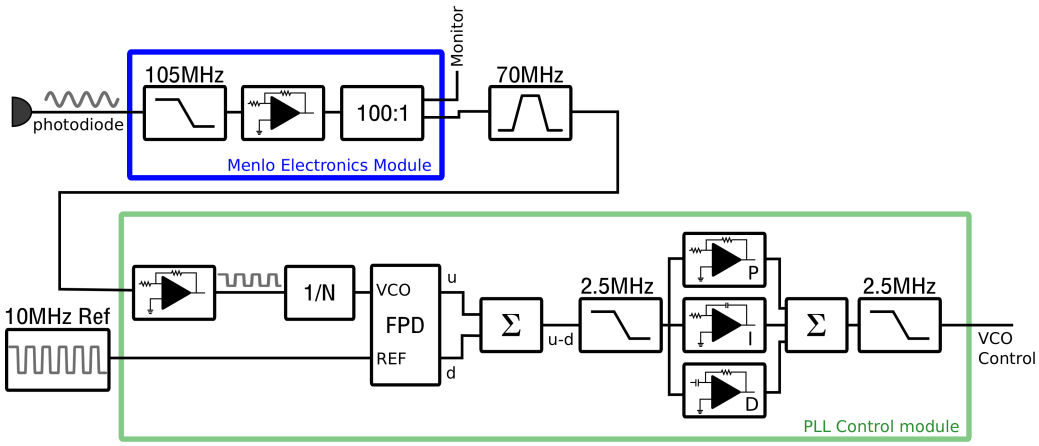

Figure 7.2: Electronic scheme for phase stability transfer

tion. The summer output correction signal, which is again filtered by a 2.5 MHz, to suppress further the remaining 10 MHz modulations. A slow integrator port exists, which integrates over the error signal to drive the piezo-electric slow drift compensation. It was not tested during the course of this work.

7.1.3 The Phase Frequency detector

The phase frequency detector we use is based on sequential D flops gates and its operation enables the determination of both phase or frequency difference between the two compared signals. Its schematic description is presented in figure 7.3a. It composes of two D-flops, each with constant logic '1' connected to the logic input and one of the signals connected as a clock. The two outputs, up and down, would indicate whether the frequency of the VCO should increase or decrease to match the reference phase. Those two output signals are fed into a NAND gate, that reset the two D-Flop outputs. Assuming at a certain time both up and down are low, both 'u' and 'd' outputs remain low until the rise

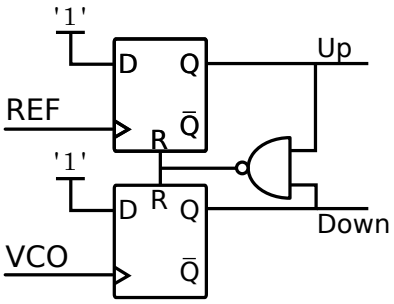

(a) Schematics for a phase frequency detector

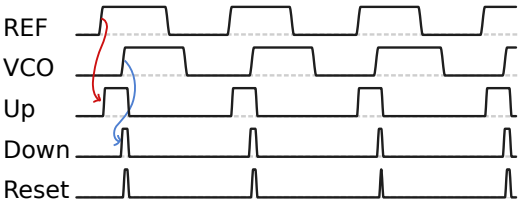

(b) A logic description of the PFD operation

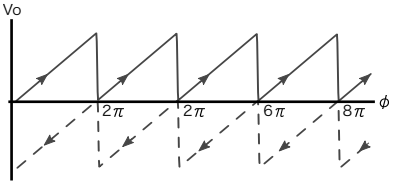

(c) PFD output Vs input phase different

Figure 7.3: PFD scheme and operation

of the first of the two compared signals. The output corresponding to the first signal will rise, until the rise of the other oscillator. When also the phase-delayed oscillator rises, the other output rises as well, and the reset signal rises (with a small propagation delay). If the VCO and reference signals repeat their pattern, the corresponding output will be of a logic signal with the same frequency as the clock and a duty cycle proportional to the phase difference between the two clocks. figure 7.3b shows a waveform plot for such scenario. The output phase is a simple linear function of the duty cycle, which can be extracted by filtering the "logic" output signal. figure 7.3c shows the S-like relation between the phase difference and the voltage of the filtered output.
The PFD can deal also with frequency differences. When the reference oscillator leads by a frequency Δf over the VCO, it accumulates phase faster. The duty cycle corresponding to phase difference will grow larger with time, until reaching 2π, where it will fold and continue to grow from zero, corresponding to a travel along the full line plot of figure 7.3c, The output voltage will correspond to the phase difference modulus 2π, which will be a periodic signal, with period being exactly the time it takes to acquire an excess phase of 2π - the frequency difference Δf.
Once the 'u' and 'd' signals are generated, we sum them up to create $v = u - d$ and filter the residual high frequencies.

7.1.4 Fiber noise cancellation system

To implement the fiber noise cancellation system we followed [37][19]. The essential idea in measuring and canceling the acoustic fiber noise is that the modulated light actually carries the information of the acoustic modulation and its phase. Owing to the fact that optical fibers introduce almost no degree of non-reciprocity, light going through a fiber in both directions experiences the same phase shift. As the time associated with the acoustic modulation frequencies is much longer than the time it takes the laser to go back and forth through the fiber, measurement of the acoustic fiber modulation can be done by extraction of the phase of light going and returning through the fiber. The optical setup is of an heterodyne detection, where light travels through the fiber in one arm. Light leaving the beam splitter cube enters an Acusto Optic Modulator (AOM), whose frequency Ω_1 is driven by a VCO which is biased to about 159.93 MHz. The 0^{th} order is reflected by a mirror, propagates back through the AOM, splits on the beam splitter cube and projected on the photodiode, to form the first arm of

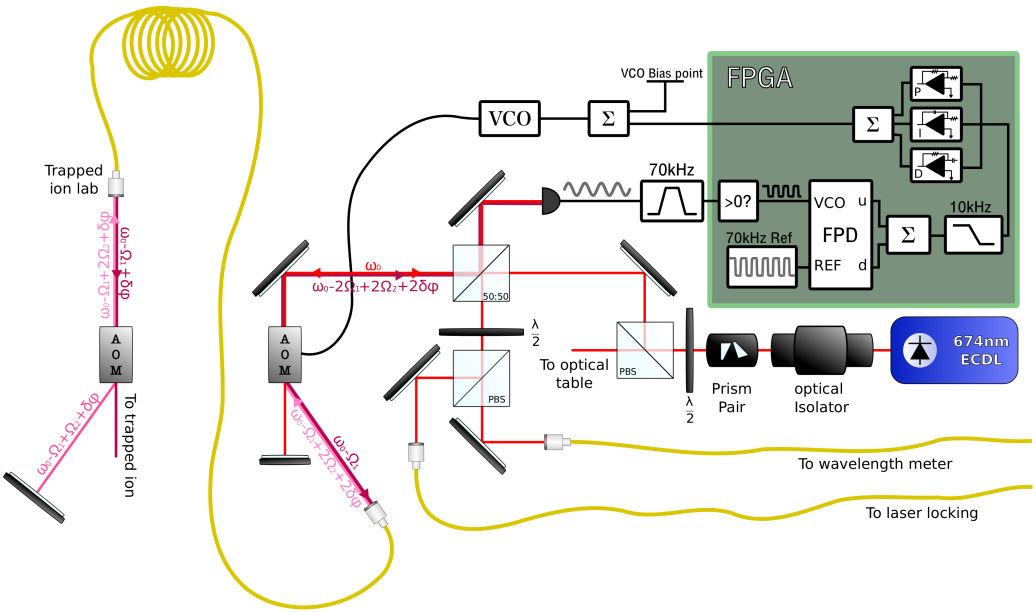

Figure 7.4: Fiber noise cancellation optical and electric scheme

the interferometer. The -1^{st} order diffracted light of the first AOM is frequency shifted by $-\Omega_1$ and coupled to a polarization maintaining optical fiber, with the other side in the distant trapped ion lab. When leaving the fiber it enters a second AOM, with modulation frequency 160 MHz set by a stable Direct Digital Synthesizer (DDS). The 0^{th} order going through the 2^{nd} AOM is the light aimed to be used as the narrow linewidth laser elsewhere, and can be compared with a local frequency reference to obtain an out-of loop estimation of the actual fiber noise cancellation performance. The 1^{st} order double passes the AOM as it reflected by a mirror, and re-coupled into the fiber. Back in the clock lab, the light leaving the fiber completes a double pass through the first AOM, after which it acquired a phase of:

$$\Phi_2 = 2\left(\Omega_2 - \Omega_1\right)t + 2\delta\phi + \varphi_2 \tag{7.1}$$

Where $\delta\phi$ is the phase associated with a single passage through the optical fiber generated by modulation, and φ_2 is some constant phase due to the propagation through air and unperturbed fiber at frequency ω. It then follows the same optical path as the other arm and overlapped with it on the photodiode. The resulting diode photocurrent is:

$$\begin{aligned} i_{pd} =& |A_1\cos(\omega_l t + \varphi_1) + A_2\cos((\omega_l + 2\Omega_2 - 2\Omega_1))t + 2\delta\phi + \varphi_2)|^2 \\ &\propto \cos(2(\Omega_2 - \Omega_1))t + 2\delta\phi + \varphi_2 - \varphi_1) \end{aligned} \tag{7.2}$$

This signal is an RF signal which carries the entire information about the fiber phase modulation. It can be used to eliminate it with a similar PLL scheme. This can be thought of as a PLL scheme for reduction of the low frequency phase noise of an oscillator, whose frequency with respect to the physical VCO sensitivity s_{VCO} and the control voltage V_c is $2(V_c s_{vco} - \Omega_2)$ and has the inherent phase noise process $2\delta\phi(t)$. After trans-impedance amplification, the corresponding RF signal is band-pass filtered, to eliminate other frequencies emanating from interferences with other reflected light, such as light reflected from the either of the fiber faces. This signal is then sampled by an FPGA, which implements a low bandwidth digital PLL scheme. The sampled signal is saturated to form a logical signal, and compared to an on board square wave of a desired frequency. A D-flop based phase detector followed by a 10 kHz filter for residual frequency removal is extracting the phase error, which is then fed to an on board PID controlled. The PID outputs an analog control signal to the VCO. With sufficient bandwidth, this feedback scheme should eliminate the fiber induced noise.
The laser light used in the rest of the experiment and needed to be compensated for fiber acoustic noise is the 0^{th} order of the second AOM. It had only passed a single time through the first AOM, corrected only half as much as intended, but on the other hand it also passes only a single time through the fiber, accumulating half the fiber induced phase. Half of the correction should then correct for half the phase modulation, and therefore we conclude that the laser linewidth should be restored using such a system.

7.2 Linewidth and phase noise estimations

A major part of this project has to do with the estimation of the spectral quality of our laser as an oscillator. The following section describes the techniques and methods for estimation of the linewidth and phase noise of our laser (compared to various different oscillators).

7.2.1 Phase noise measurements

We implemented an all digital version of the two quadratures scheme presented in section 5.1.3, following [38]. The general scheme is presented in figure 7.5a. The oscillating signal is oversampled at frequency $F_s = 1/T_s$ on a digital oscilloscope (Tektronix DPO 4034, 8bit vertical resolution) producing

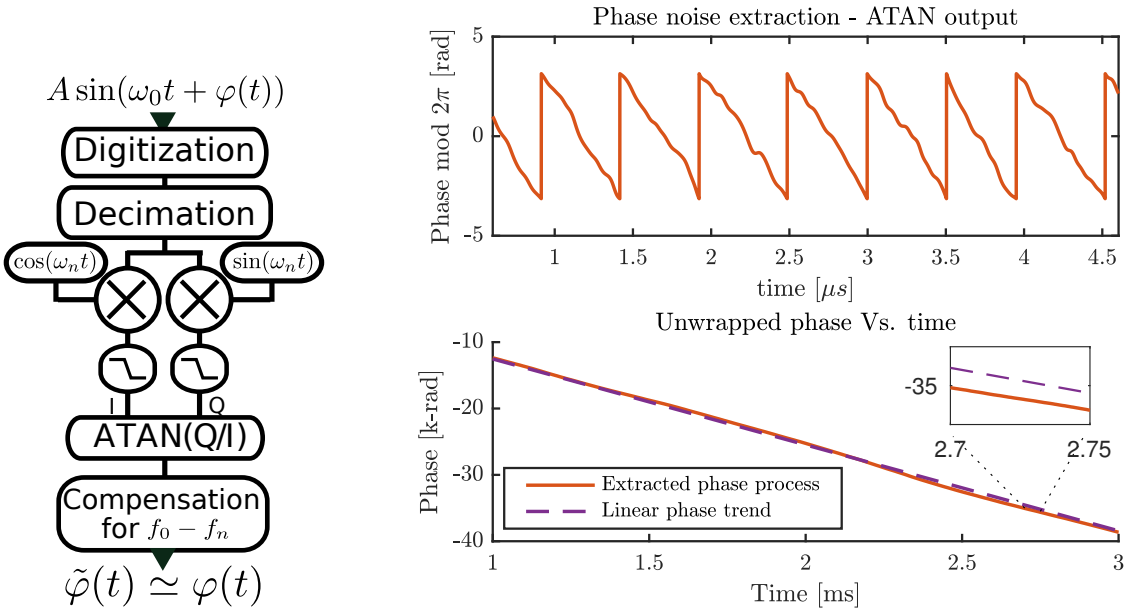

(a) The method scheme

(b) Wrapped phase at the output of the inverse tangent, and its unwrapping.

Figure 7.5: Digital phase noise extraction method

$V[n] = V(n \cdot T_s)$. At first it is averaged and decimated by a factor N_1 so that in the resulting time series:

$$V[n'] = \frac{1}{N_1} \sum_{i=0}^{N_1 - 1} v[N_1 \cdot n' + i] \tag{7.3}$$

It is done in the purpose of reducing the white quantization noise emanating from the resolution depth of the oscilloscope. It can be thought of as if by averaging, the vertical resolution of the oscillator is increased according to $\Delta_{bit} = \frac{1}{2}\log_2 N_1$. Next, the signal is mixed with two quadratures of a signal oscillating at f_0 and low pass filtered to eliminate the $f_n + f_0$ frequency component. f_0 is chosen such that the mixed signal, oscillating at $f_0 - f_n$, will be sufficiently spectrally far from DC so that its left sideband won't be spanned through DC. The resulting two signals of the Q and I branch are than fed into a 4 quadratures inverse tangent function, which produces time samples of the signal described at Eq. (5.7). Next, the phase is unwrapped, the linear trend corresponding to an oscillation frequency of $f_0 - f_n$ is removed, and the phase noise process is extracted. Figure 7.5b displays an example of the wrapped phase at the inverse tangent function and the unwrapped phase with the corresponding frequency trend.

To demonstrate the validity and limitations of the phase noise extraction method we performed a simulation: We first created a phase noise signal as a sample of a random process with power spectral density that resembles that of a laser oscillator, $\varphi_G[n] \equiv \varphi_G(nT_s)$. The blue trend in figure 7.6b depicts $\varphi_G(t)$ and its estimated power spectral density. This signal was than used to generate an oscillating signal with nominal frequency ν_0:

$$s_g[n] = (1 + w[n]) \cdot \cos(2\pi\nu_0 T_s n + \varphi_G[n]) \tag{7.4}$$

Where $w[n]$ is some zero mean white noise process representing amplitude fluctuations. This signal was the fed as the test signal to the phase noise extraction process. The extracted phase noise is the pink trend displayed in 7.6b. It is apparent that the method gives a good estimation of the power

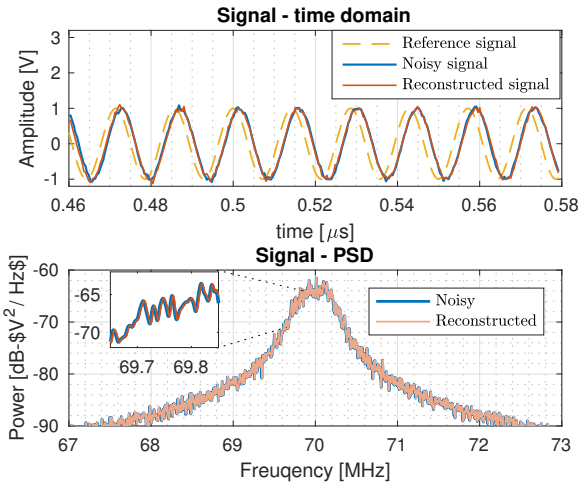

(a) An oscillator with an generated phase and amplitude noise processes, compared to an oscillator with the extracted phase noise

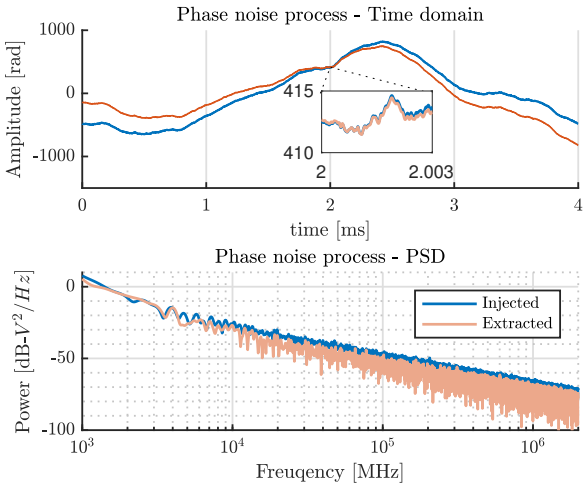

(b) The generated phase noise Vs. the detected phase noise properties

Figure 7.6: Demonstration of the method validity

spectral density of spectral frequencies well below the inverse observation time, which for our signal was 4 ms. On the other hand, it fails on estimating the frequencies, which can be seen as the difference between the generated and extracted trends on longer time scales. The extracted phase noise series $\varphi_E[n]$ was then used to create a different oscillating signal:

$$s_e[n] = (1 + w[n]) \cdot \cos(2\pi\nu_0 T_s n + \varphi_E[n]) \tag{7.5}$$

The two oscillating signals are compared and shown to yield almost the exact same power spectral density estimate, shown in figure 7.6a. In both the time domain and power spectral density graphs, $s_g[n]$ is plotted in blue and $s_e[n]$ is plotted in orange. In the time domain plot also a yellow reference oscillator signal without any amplitude or phase noise is plotted for comparison.

7.2.2 Two lasers comparisons

To estimate our locked laser linewidth we established a heterodyne detection scheme with the probe laser. This detection is performed either using the BDU, the fiber coupled beat detection unit, or on a free space heterodyne setup which was built in the trapped ion lab, so that that our clock laser could be estimated with the fiber noise cancellation system working. The characterization of the oscillation properties was done by mixing the beat signal, generated by the photodiode trans-impedance amplifier, down to IF using a stable local oscillator, and low pass filtering the higher frequency component. The signal is then recorded and analyzed, either for phase noise retrieval or for determination of the long time stability. This is done by recording the beat and extracting its central frequency repeatedly. After obtaining a time series of the beat frequency, with sampling period equal to the interrogation time of the beat signal, the Allan variance could be computed to obtain the a measure of the long term stability.

7.2.3 Interaction with trapped ion

The clock laser light is emitted in the trapped Ion lab after being phase locked to the comb and compensated for fiber induced phase noise. This radiation is then used to manipulate the internal state of a strontium ion, and to perform spectroscopic measurements of it. We replace the probe

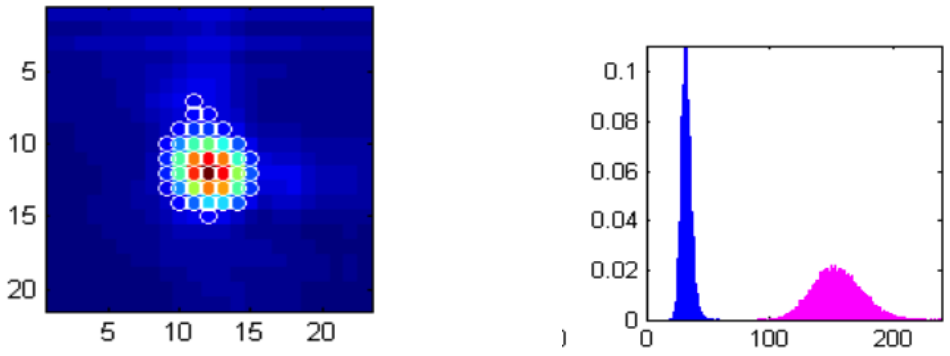

(a) Camera image of a trapped ion

(b) Photon count histograms of a florescent and 'dark' ion

Figure 7.7: Florescence detection imaging system

laser, usually used to couple the $\left|5S_{\frac{1}{2}}\right\rangle \leftrightarrow \left|4D_{\frac{5}{2}}\right\rangle$, with our clock laser. We coupled the clock laser into a short fiber and connected its other end in place of the probe laser. The clock laser beam is then injected into a slave diode, forcing it to lase at its exact same mode. The slave diode output radiation then propagates to the ion through a series of AOMs, EOMs and optical elements to be able to control the 674 pulse duration and frequency offset, as well as its spacial properties like the beam focus and waist. The optical and electrical setup of the ion trap with respect to the 674 nm laser is further described in [13] [39] [40].

We performed mainly three distinct spectroscopic measurements, for each type of measurement reveal different aspects of the ion-laser coherence. These measurements demanded the ability to interact with the ion with time controlled optical pulses, at controllable frequency and power. To do so, we used the two AOMs in the laser optical path. The pulse duration and power was set by controlling the attenuation of the two RF sources fed into the two AOMs, effectively closing it when the attenuation was large enough. The frequency offset was determined by changing the central frequency of the single-pass AOM, which enabled us a scan range of about 30 MHz about the AOM central frequency. This setup gave us sufficient control over the optical pulse duration and power, together with the ability to frequency shift the carrier frequency of our pulse.

Detecting the state of the ion is done by performing state selective florescence, described in section 6.1.2. In our experimental setup the photo-detector is a fast and sensitive CCD array camera (Andor iXon Ultra EMCCD). During the detection period the camera collects photons scattered by the ion, and when the 422 nm laser shuts down the total number of collected photons in each pixel is counted. the histogram of collected photons is produced and discriminated as being generated from an ion collapsed to a $|D\rangle$ state or $|S\rangle$ state. To actually reconstruct the ion superposition at the time of the detection, multiple repetitions of the same experiment must be carried out, as due to the projective nature of the measurement each single observation yield only 1 bit of information about the superposition coefficient. Alternatively, taking the superposition as $\sqrt{p}\,|s\rangle + \sqrt{1-p}\,|D\rangle$, we know that the variance of the binomial parameter estimator $\hat{p} = \frac{1}{N}\sum^{N} X_i$ diminishes like $N^{-\frac{1}{2}}$, N being the number of independent measurements. Further description of the detection optics and the process itself can be found it [41]

The ability to control the duration, power and frequency of the pulse forms the basic tools needed to perform Rabi spectroscopy, Rabi oscillations and Ramsey interferometry measurements. These were carried out and the results were analyzed according to section 6.2.2.

Chapter 8

Results

8.1 Frequency comb

As a prior to the characterization of the clock laser we measured some of the locked comb spectral properties. First, we performed a power spectral density estimation of the two RF signals determining the comb frequencies. Figure 8.1a shows the f-2f interferometer beat note, extracting the carrier envelope offset frequency as described in 4.4. The spectrum, obtained to a 10 kHz bandwidth, is presented over a 1 MHz span around 60 MHz. It exhibits a coherent peak with sidebands attenuated by 30 dB. The beat in 8.1b is the optical beat of the stable laser and the closest comb tooth, used to stabilize the comb repetition frequency. As opposed to the previous spectrum, this one shows a significant servo bumps at about 200 kHz. As changing the lock parameters also affects the position and power of these bumps, it seems to be an evidence for the small bandwidth of the comb repetition rate locking. These servo bumps, unavoidable if one needs high gain for elimination of low frequency phase noise, would be transfered to any laser using the comb as an optical reference, assuming its lock circuit bandwidth is sufficiently high. It then limits the ability to eliminate phase noise around these frequencies. Since laser diodes have a usual fast linewidth <1 MHz, it seems to limit the ability to use the comb as a clean reference for phase noise reduction.
To have a better estimation of a comb tooth frequency spectrum, we recorded the beat note of our 674 nm comb laser, when both RF frequencies are locked, with the probe laser, which is known to have a linewidth <100 Hz [40]. Since this probe laser is generated in a distant lab, it had to be delivered through a 60 m optical fiber. The probe laser linewidth is then fiber noise broadened, but is still expected to have a fast linewidth <1 kHz when emitted in the comb lab. According to section 2.2.1, the resulting PSD is an estimation of the power in the phase noise process of the two lasers together. This places a bound on the phase noise of each of the lasers alone, as for the variance of a sum of two

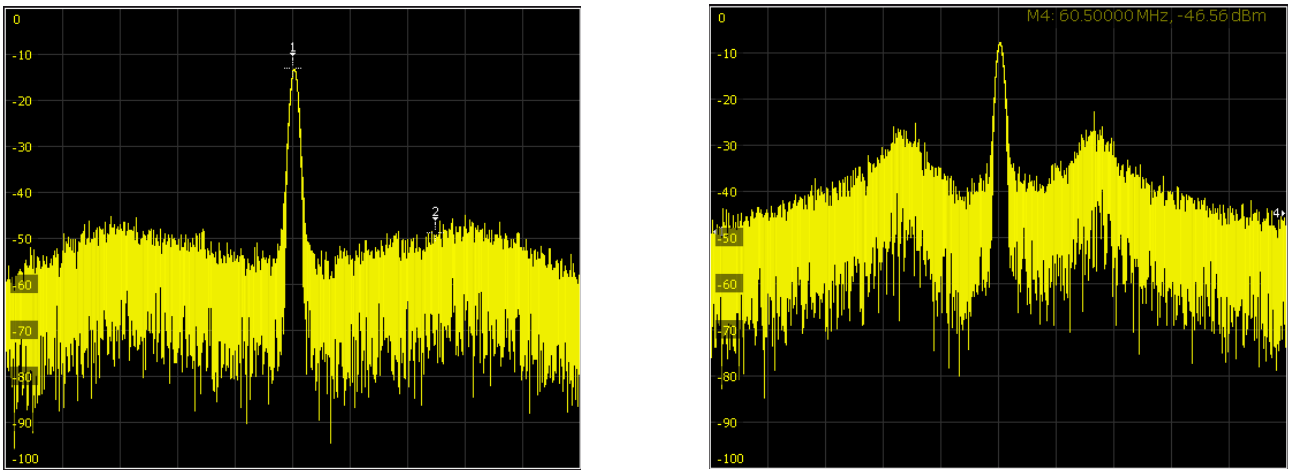

(a) f-2f interferometer beat used to lock the carrier envelope offset frequency

(b) Beat note of the comb tooth and the stable 1560nm laser

Figure 8.1: In loop beat notes stabilizing the comb

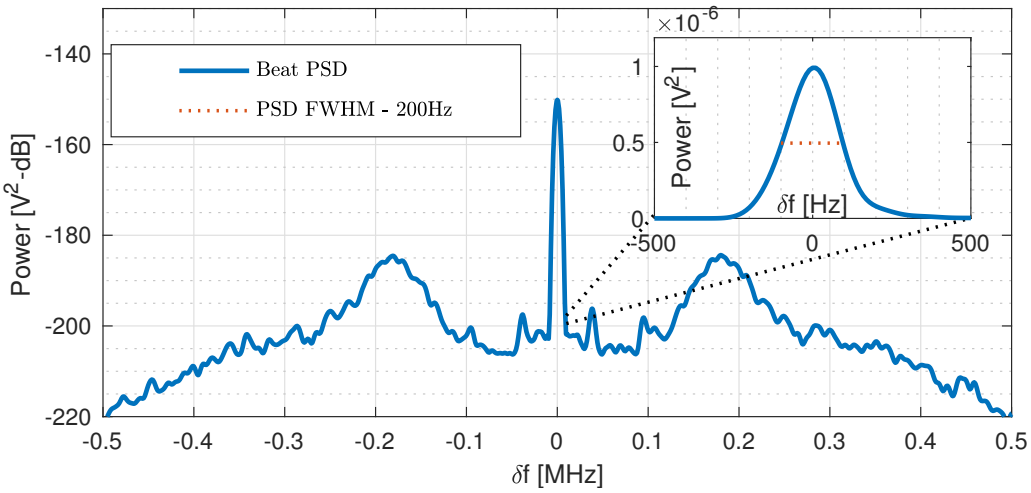

Figure 8.2: PSD estimation for the comb and probe laser beat note

uncorrelated phase noise processes equals the sum of its variances [42]:

$$\varphi(t) = \varphi_l(t) - \varphi_{ion}(t) \rightarrow \sigma^2 = \sigma_l^2 + \sigma_{ion}^2 - \frac{1}{\tau^2}\langle(\varphi_l(t+\tau) - \varphi_l(t)) \cdot (\varphi_{ion}(t+\tau) - \varphi_{ion}(t))\rangle \tag{8.1}$$

The Power spectral density of the probe laser and the frequency comb beat, presented in figure 8.2 was estimated from the recorded beat note of the two over a 10 ms time window. The coherent peak, with estimated full width at half the max value (FWHM) of 200 Hz, helps us both in determining the expected phase noise broadening of a laser going through the two labs, and also sets a bound on the spectral width of each one of the lasers alone, ensuring us that the comb has a coherent pick of width smaller than or equal to that measured. The sideband spectrum of the comb presents a remarkable feature of excess noise at about 200 kHz, probably corresponding to the comb servo bumps. As suspected, these repetition rate servo bumps might degrade the ability of the comb to act as a stable optical frequency reference

Another measurement carried out was a long-term comparison of the comb repetition frequency with a stable RF oscillator, referenced to the GPS optical clock. This kind of measurement, being carried out

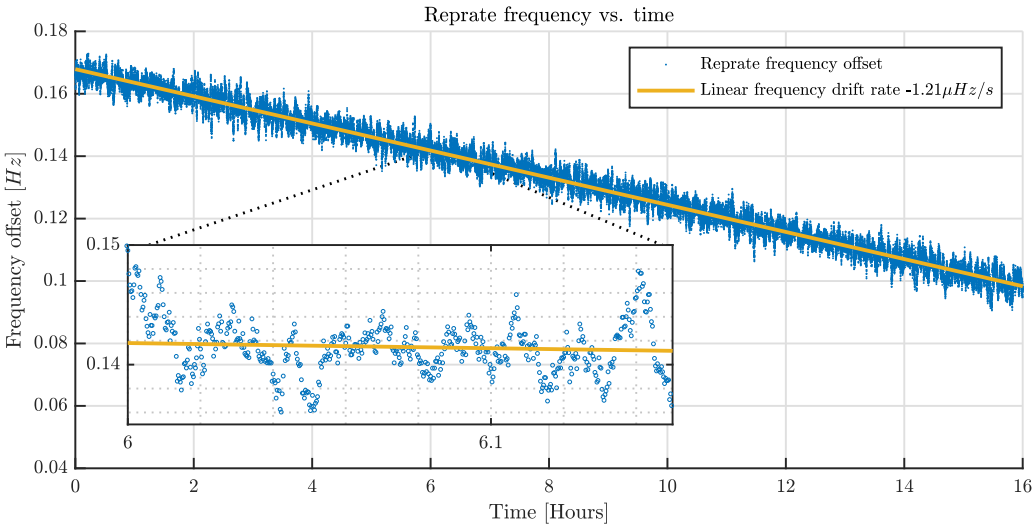

Figure 8.3: Long term comparison of the repetition frequency offset from its nominal value and a GPS atomic clock

in the RF domain, is easier to perform and was done using a frequency counter. The comb repetition frequency was counted and estimated every second, and the resulting long term plot of the frequency Vs. time is presented in figure 8.3. The linear drift trend extracted was estimated to be $1.2\,\mu\mathrm{Hz\,s^{-1}}$, that amounts to a drift of about 2.13 Hz's at 674 nm. This drift is suspected to be caused by the stable laser, and in particular by a drift of its reference cavity resonance wavelength. If it drifts, as cavities often do, it would force the stable laser carrier frequency to drift with it, and the repetition rate, being locked to it, will drift as well. Corresponding to the measured repetition frequency drift, the stable laser cavity should be drifting at $0.92\,\mathrm{Hz\,s^{-1}}$, a rate larger by an order of magnitude than that stated by the stable laser cavity manufacturer. While the reason for such high drift rate should be further investigated, for the purpose of estimation of the clock laser properties we can just be aware of the frequency comb drift rate and remove the drift in the analysis when necessary.

8.2 the 674 Laser

8.2.1 AM and FM frequency response

A crucial step in designing the controller in an electronic feedback system is to determine the open loop transfer function of the system. To do so, we had to measure the frequency response of our laser. A modulation of the current going into a laser diode affects both the output power (due to the change in number of injected charge carriers) and the laser frequency (through the induced modulation of the refractive index). To measure the amplitude response, we recorded the power incident on a photodiode, as we modulated the current through the current driver bias port and modulation port. We then estimated the response function for the two ports. Figure (8.4) shows the measured data along with a plot of the estimated transfer function: The bias current port of the current driver is known to have a low modulation bandwidth of about 7 kHz. The equivalent linear system, yielding a similar gain and phase response over the relevant frequencies, was estimated to be:

$$H_{AM-bias}(s) = \frac{1}{3.12\cdot 10^{-16}(s+4.22\cdot 10^4)\cdot\prod_{j=0}^{1}(s+2.93\cdot 10^4+i(-1)^j 9.02\cdot 10^4)} \tag{8.2}$$

Which is an order 3 low pass filters with poles starting at $\omega = 2\pi\cdot 6.7\,\mathrm{kHz}$. This gives evidence for the bias port of the current driver to be insufficient for correction of fast phase noises. The modulation

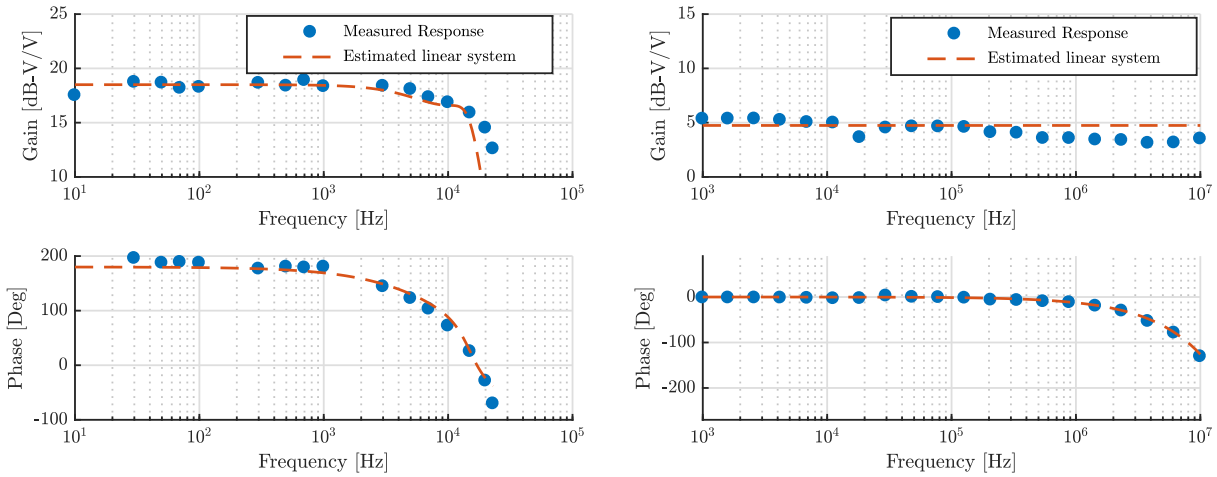

(a) $H_{bias}(s)$ - LPF Characteristic

(b) $H_{mod}(s)$ - time delay

Figure 8.4: AM Response through two modulation ports

port frequency response was estimated as a system exhibiting a delay of 35 ns:

$$H_{AM-mod}(s) = 4.74 \cdot e^{-3.5 \cdot 10^{-8} \cdot s} \tag{8.3}$$

This delay might be anywhere along the way from the signal generator to the photodiode on which we recorded the beat, so it is not necessarily the electronic delay on the port, but it sets a pessimistic bound on the bandwidth of that channel.
The FM response of the laser is a measure of the modulation depth and phase of the laser frequency, in response to a modulation of one of the laser ports. Knowing that the piezo electric port controlling the grating angle has a mechanical bandwidth of only a couple of kHzs, we set to determine the response through the current modulation port. Such measurement requires some kind of FM demodulation scheme, which can be an electric or rather optical apparatus translating frequency into amplitude. We choose to go down a different path and digitally analyze a recoded beat signal of the modulated clock laser and the comb. Using short time Furrier transform technique, we created a spectrogram image of the two lasers beat with a satisfactory resolution in both time and frequency. From this image we were able to extract the frequency modulation signal and obtain the phase and gain response. Figure 8.5a presents such spectrogram image and the corresponding extracted signal. The time resolution limited the modulation frequency to be less than 2 MHz, while the frequency resolution limit of ~ 22 MHz sets the major error contribution to the gain estimation. Figure 8.5b presents the measured FM response of the system and the corresponding linear system estimated to best fit the measured data. The gain here, being FM response, has the dimensions of Hz V^{-1}. The estimated system is a single pole system with delay:

$$H_{FM}(s) = e^{-1.2 \cdot 10^{-7} \cdot s} \frac{1.74 \cdot 10^8}{\frac{s}{2\pi \cdot 6 \cdot 10^5} + 1} \tag{8.4}$$

Since the delay here is an order of magnitude larger then the AM response delay Eq. (8.3), we can safely account most of it to the different electronics involved in the beat note measurement. The pole at $\omega = 2\pi \cdot 0.6$ MHz gives a good estimation of the point where phase begins to drop, and thus determines the bandwidth of the control loop.

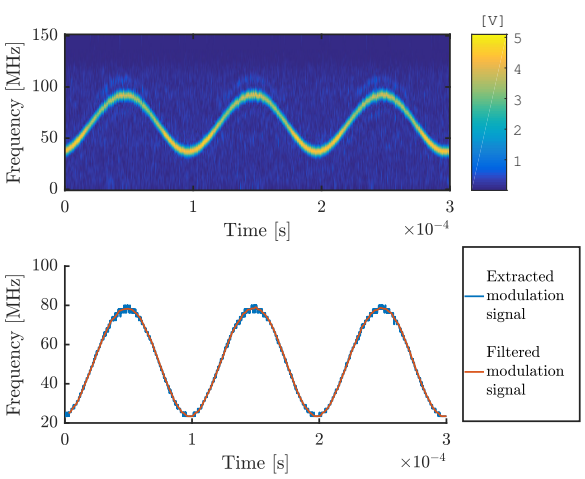

(a) Modulation signal extraction using the spectrogram image

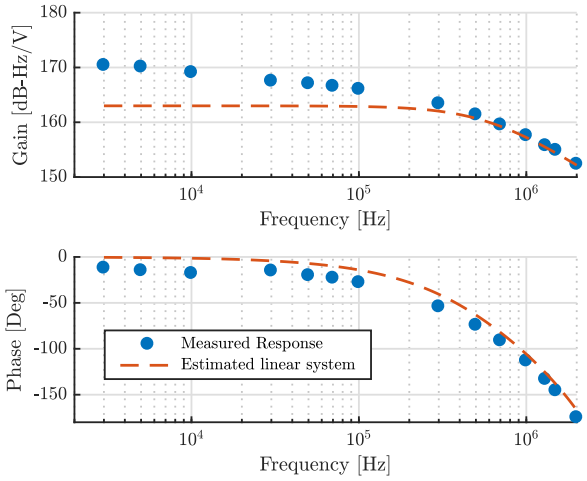

(b) FM linear response - Bode plot

Figure 8.5: FM response through current modulation port

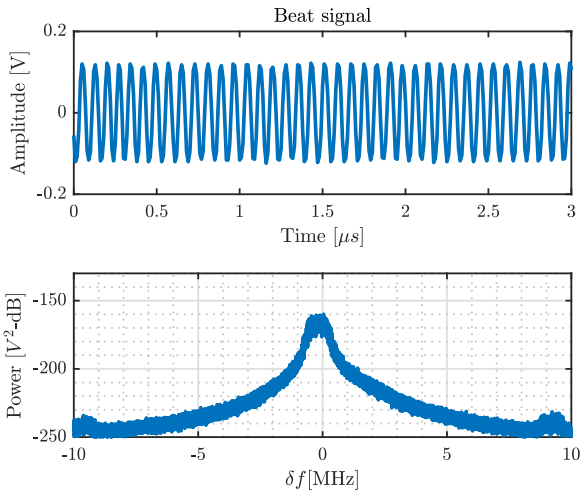

(a) Probe Vs. clock laser beat signal and corresponding estimated PSD

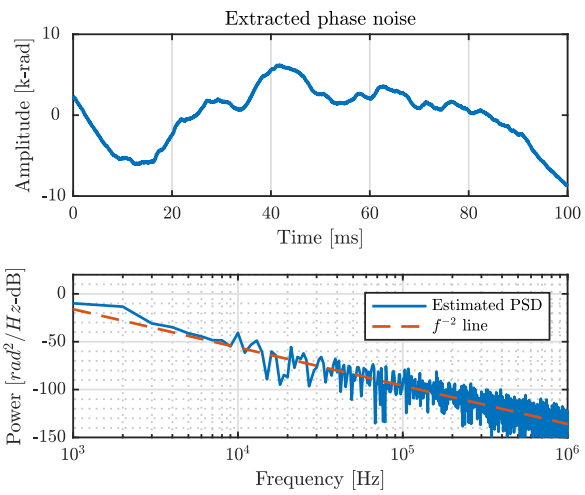

(b) Extracted phase noise process and its estimated PSD

Figure 8.6: Phase noise estimation of the prove Vs. clock laser beat

8.2.2 Linewidth measurements

To estimate the linewidth of the unlocked 674 ECDL, we observed the beat between our unlocked clock laser and the probe laser. Again, here the probe laser was delivered through a 60m optical fiber, so it is spectrally broadened. As shown at figure 8.2, it can be safely assumed to be narrower then 1 kHz, so we can use it to estimate our unlocked laser performance. The beat of the clock laser and the probe laser was recorded over a time window of 100 ms. We extracted the phase noise process using the method described in section 7.2.1, and estimated its PSD. The two lasers beat PSD, with a linewidth of about 1 MHz, is much wider than the probe and comb beat, indicating that the majority of the phase noise comes from the unlocked clock laser. Figure 8.6b presents the extracted phase noise sample time signal and its power spectral density estimate. The phase noise PSD has a f^{-2} form, which indicates the dominance of white frequency noise, as expected from a laser diode away from the carrier.

8.3 Laser stabilization

As described, we used a PLL control scheme to eliminate the laser phase noise and to phase lock it to the frequency comb tooth. In light of the measured laser FM response and phase noise, the lock bandwidth and gain had to be considered.

8.3.1 Controller frequency response model

The control parameters were first estimated using a computer transfer function model. We used the simple PLL model presented in figure 5.3, and the following transfer functions were used for the estimation:

1. The phase detector: the entire electronic configuration of the phase detector consists of a FPD as explained in section 7.1.3, a summer with 1/100 attenuation and and an LPF with pole at $\omega = 2\pi \cdot 2.5\,\text{MHz}$. Since the loop bandwidth should be almost an order of magnitude smaller then that, this additional LPF was neglected for initial estimation. The phase detector operational

voltage was 5V, so the phase detector transfer function was estimated as a gain of:

$$H_{PD}(s) = \frac{5}{2\pi} \cdot \frac{1}{100}$$

2. The loop controller: The loop controller is implemented as three parallel amplifiers, each connected in a P, I or D configuration. The three are then summed on a configurable gain summer amplifier. Thus the loop transfer function is

$$H_C(s) = k_s \left(kp + \frac{k_i}{s} + k_d s \right)$$

Where k_s, k_p, k_i and k_d are the configurable gains of the summer, proportional, integral and derivative amplifiers respectively. adjustment of the gain is done by controlling the knob of four variable registers. There are four controllers on three effective degrees of freedom, but controlling the total gain with the sum makes it more practical to optimize the loop parameters.

3. The VCO: We used the measured response of the VCO from Eq. (8.4), with an addition of an integrator (as we describe the phase response)

$$H_{VCO} = e^{-1.2 \cdot 10^{-7} \cdot s} \frac{1.74 \cdot 10^8}{s(\frac{s}{2\pi 6 \cdot 10^5} + 1)}$$

4. The frequency divider: We worked with N=7

In general, the open loop transfer function was modeled as follows:

$$\begin{aligned} ol(s) =& e^{-1.2 \cdot 10^{-7} \cdot s} \frac{5}{2\pi} \cdot \frac{1.74 \cdot 10^6}{7} \frac{k_s \left(k_d s^2 + k_p s + k_i \right)}{s^2 \left(\frac{s}{2\pi 6 \cdot 10^5} + 1 \right)} \\ \equiv& e^{-1.2 \cdot 10^{-7} \cdot s} \frac{\left(K_d s^2 + K_p s + K_i \right)}{s^2 \left(\frac{s}{2\pi 6 \cdot 10^5} + 1 \right)} \end{aligned} \tag{8.5}$$

The open loop has three poles: two integrators and a pole at about 0.6 MHz, and two zeros at

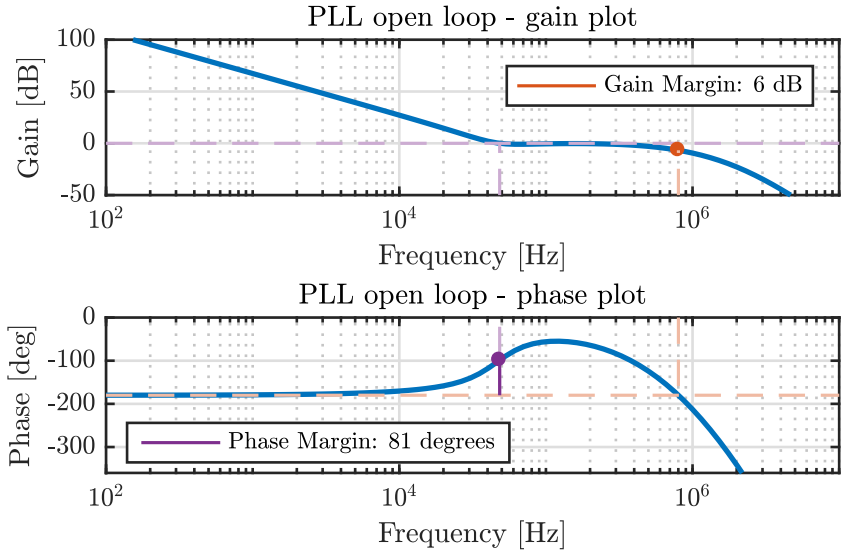

Figure 8.7: Transfer function model for the open loop $H(s)$. The red and purple points corresponds to the 180 phase and 0dB gain points, respectfully

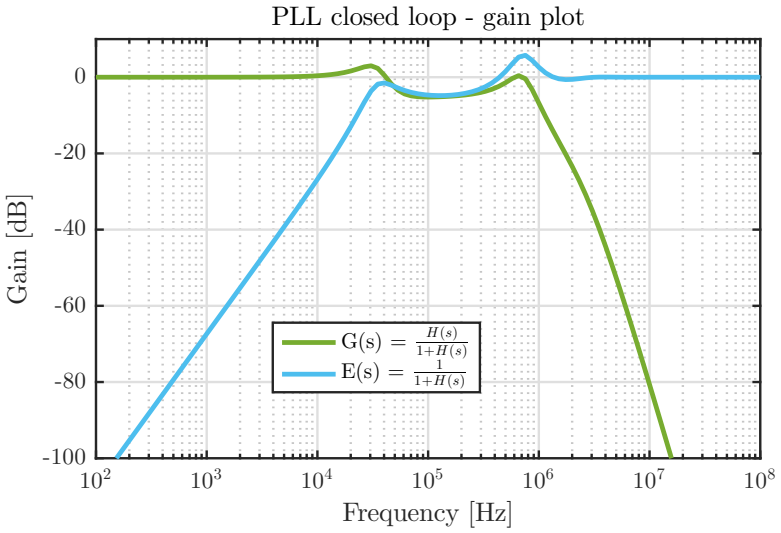

Figure 8.8: Transfer function gain plot for the reference phase $G(s)$ and the oscillator phase noise $E(s)$

configurable frequencies. It starts with a -π phase due to the two integrators, and rolls down due to the delay and pole starting 300 kHz. This roll off sets the limit on the possible loop bandwidth. Being so, the two zeros needs to be placed such that at the unity gain point both those zeros will already contribute their phase increase, leading to a positive phase margin. More so, to optimize the low frequency gain factor, the two zeros are desired to be placed close to the unity gain frequency, so that the gain slope will be 40 dB/dec
The optimal gains were estimated by performing optimization of the $1\,\mathrm{rad\,s^{-1}}$ gain, constrained by keeping phase margin bigger then 40°. These were then set using the variable resistors, and final adjustments were carried out to optimize the actual transfer function (as opposed to the transfer function model).

figures 8.7 shows the open loop model with the actual gains used to lock the laser phase. This model is the one specified in Eq. (8.5), with additional low pass filters at 2.5 MHz that where overlooked for the initial estimation of loop gains. The model shows higher then expected phase margin of 80° degrees, and lower gain margin of 6 dB. The closed loop transfer function for the reference phase and VCO phase noise is also displayed in figure 8.8 showing a bandwidth of about 0.5 MHz, where already at 50 kHz the phase noise filtering gain greatly decreases.

8.3.2 In loop measurement of the stabilized optical beat

We examined the clock laser and frequency comb beat signal when phase locked to the external reference 10 MHz RF signal to appreciate the PLL performance. We recorded the beat of the two lasers with and without the PLL feedback connected, at about 70 MHz, sampled at 500 MHz. Figure 8.9 shows the spectrum of the "free running" (without PLL feedback) and locked beat signals. It is clear that s substantial amount of the signal energy is concentrated around the central peak, here evaluated to a 1 kHz resolution limit, whereas for the free running signal the energy is spanned over a much larger frequency ranges. Inspecting the locked beat PSD plot, it can be seen that the lock bandwidth is about 0.5 MHz, a bit more then the assumed model but still within a reasonable gap. The most distinctive features are the bumps at about 200 kHz. These are noises that are supposed to be within the loop bandwidth but are not eliminated. They seem to originate by the frequency comb servo locking the comb to the stable laser, as discussed in section 8.1. The PLL modulate the clock laser to fight the comb induced noise, and reduces the bumps to a level limited by the gain at 200 kHz. Furthermore, the PLL actually transfers these servo bumps to the clock laser spectrum, so that these bumps are

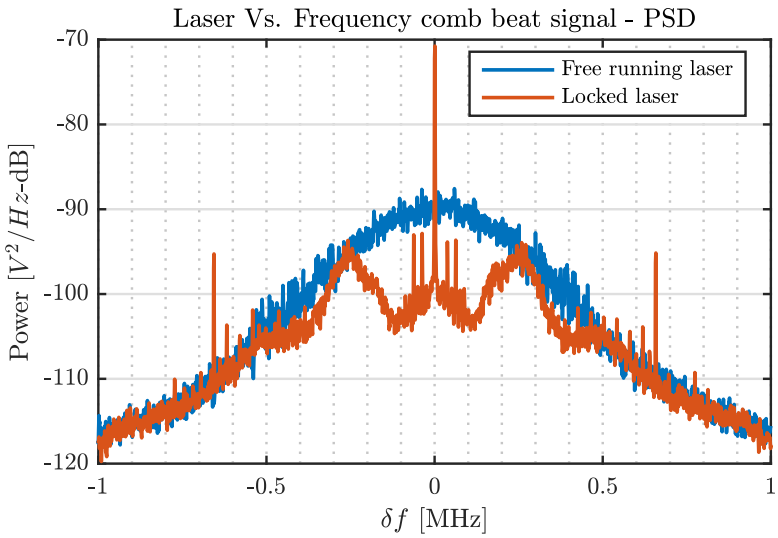

Figure 8.9: In loop measurement of the clock laser Vs. 674 nm Comb beat note power spectral density in the locked and unlocked states

likely to be seen implanted on the clock laser spectrum even when it is beat with an uncorrelated laser.

Figure 8.10 displays the extracted phase noise process sample, and its power spectral density estimation. As before, the free running PSD is dominated by white frequency noise at frequencies above a couple of kHz's, indicated by the yellow f^{-2} trend. The locked beat note PSD on the other hand displays a flat spectrum, evidence for the diminishing PLL gain with frequency. The 200 kHz bumps related to the comb phase noise are also apparent, after which the phase noise power goes down like f^{-2}, as it is outside of the PLL bandwidth.

8.3.3 Out of loop beat measurement

To measure the actual spectral properties of our clock laser, we needed to compare it to an uncorrelated frequency reference, as the in-loop measurement can only quantify the phase lock quality. To do so, we used the setup described at section 7.2.2, and recorded the probe laser and clock laser beat. Figure 8.11 presents the power spectral density estimation of the two lasers beat, with and without the active

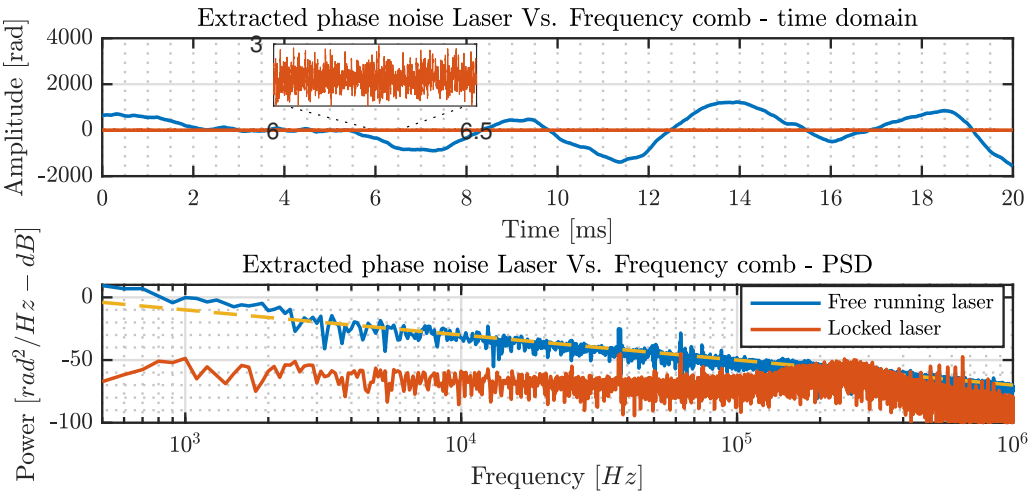

Figure 8.10: In loop - Clock Vs. Comb beat note extracted phase noise and its PSD

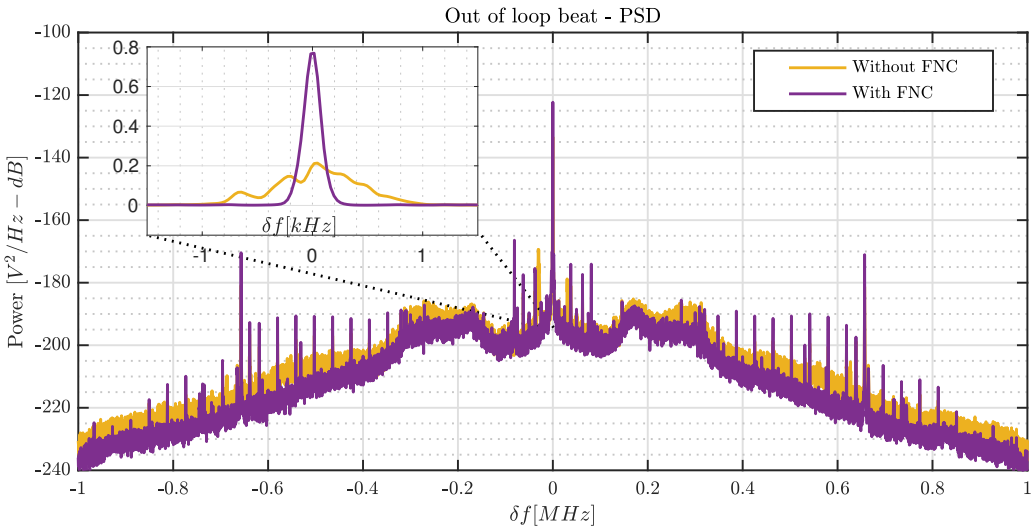

Figure 8.11: PSD estimation probe and clock laser beat, with and without active fiber noise cancellation (FNC)

fiber noise cancellation. Both the spectra contain the 200 kHz bumps, injected to the clock laser by the PLL, as discussed in previous section. The spectra also includes a series a spikes, all of which are evenly spaced at 38 kHz, which seemed to be coming from the electronics as it exists in many electronic systems in our lab, including the ground grid itself. Also the large spike at 600 kHz is found to be a major component in our ground network, and eliminating these frequency components remains an objective yet to be achieved.

The spectrum peak is presented in the boxed plot, which demonstrate the contribution of the fiber noise cancellation system. Here, we zoom into the central peak and plot it on a linear scale. The yellow trend, without active fiber noise compensation, presents a peak with width of about a couple of hundreds of Hz's. When noise cancellation is active, however, the peak is seen to be narrower, and in this plot is Furrier limited. A longer interrogation is needed to observe the true spectral width.

To do so we further mixed down the beat with a stable local oscillator to 75 kHz, and band pass filtered it in a 30 kHz wide filter. Decreasing the beat frequency enabled us to decrease the sample rate, allowing for longer observation times and lower Furrier limit. Figure 8.12 demonstrates the PSD estimators for a couple of beat signals recorded for 80 ms, leading to 12.5 Hz Furrier limit. For clarity purpose, the peak was frequency shifted when plotted to be equally spread on the plot region, so the actual frequency is meaningless, but the width is still to scale. The full width half max (FWHM) was measured for the signals, leading to about 20 Hz width of the two lasers. Each beat contains significant 50 Hz and 100 Hz sideband components, indicating that power grid related oscillation might coherently modulate one (or both) of the lasers.

When examined over long times, the beat signal exhibited a noticeable linear drift. This drift was anticipated considering the comb drift of section 8.1. More so, the probe laser was characterized before and found to drift at a rate lower by at least an order of magnitude [40], so it has to be due to the clock laser drift.

To estimate the laser drift rate, we took the same down-mixed band pass filtered signal, and sampled it with an FPGA repeatedly. The FPGA retained the samples for one second, and sent it to the computer for analysis while sampling another second. Out of each array of samples containing a second of oscillation the beat spectrum was estimated and the spectrum peak was estimated as the momentary frequency. A series of frequency measurements Vs. time was obtained, and the measurement was carried out until the beat drifted out of the filter bandwidth. Figure 8.13 presents this time series of frequency measurements. The series exhibits an obvious linear drift, measured to be $2.4\,\mathrm{Hz\,s^{-1}}$.

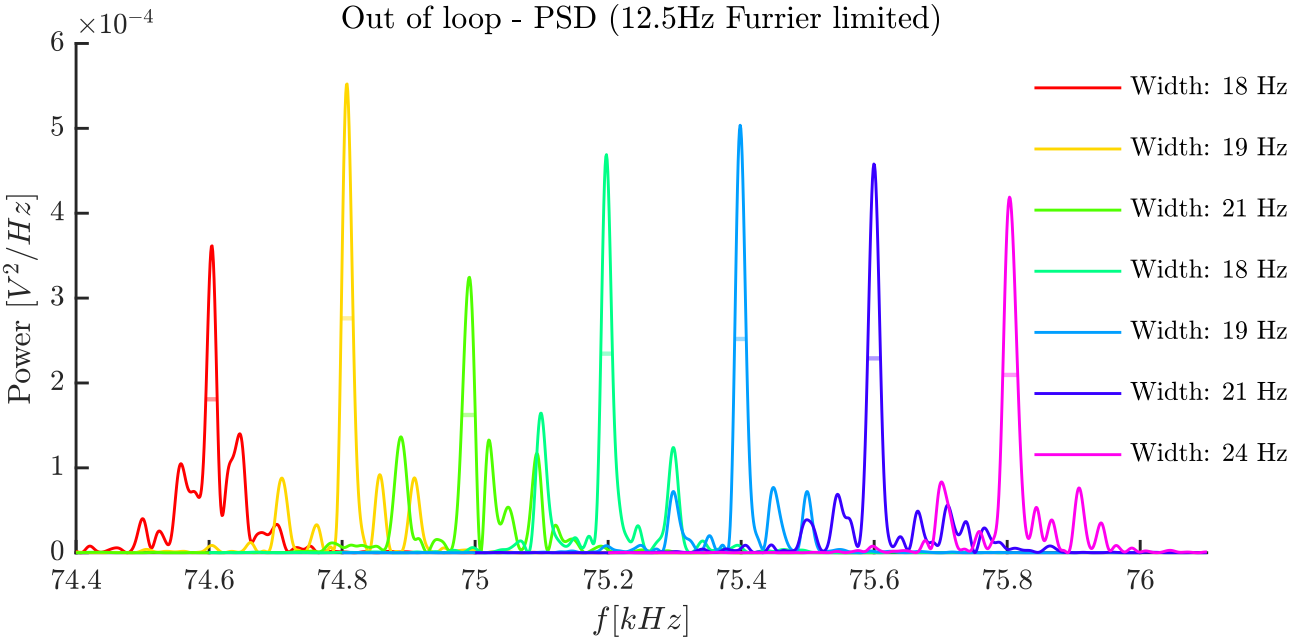

Figure 8.12: Power spectral density of the two lasers beat showing $20Hz$ spectral width at half the maximum power

Relating this drift to the measured repetition frequency drift reported at section 8.1, we can hold it mainly responsible for the drift measured for the two lasers beat. The rate difference is about 10% of the drift rate, and can be due to the fact that the two measurements where not conducted at the same time, and the drift rate of the repetition frequency does change over time.
Another view on the phase noise of the two laser beat is by plotting Allan variance Vs. integration time. We were able to extract the phase noise signal out of the beat by the same methods described above. The Allan variance over short time scales could be measured from that signal, in which the integration time is limited by the memory depth of our oscilloscope, imposing in our case about 100 ms limit. On the other hand, the frequency time series of figure 8.13 could be used for Allan variance

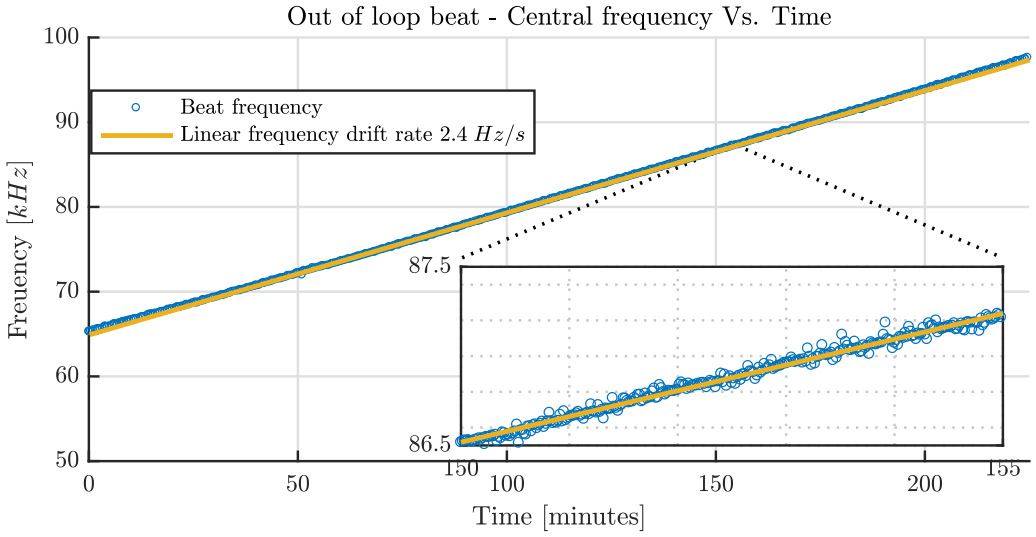

Figure 8.13: Central beat frequency measured over long time scale, showing a substantial linear frequency drift over time

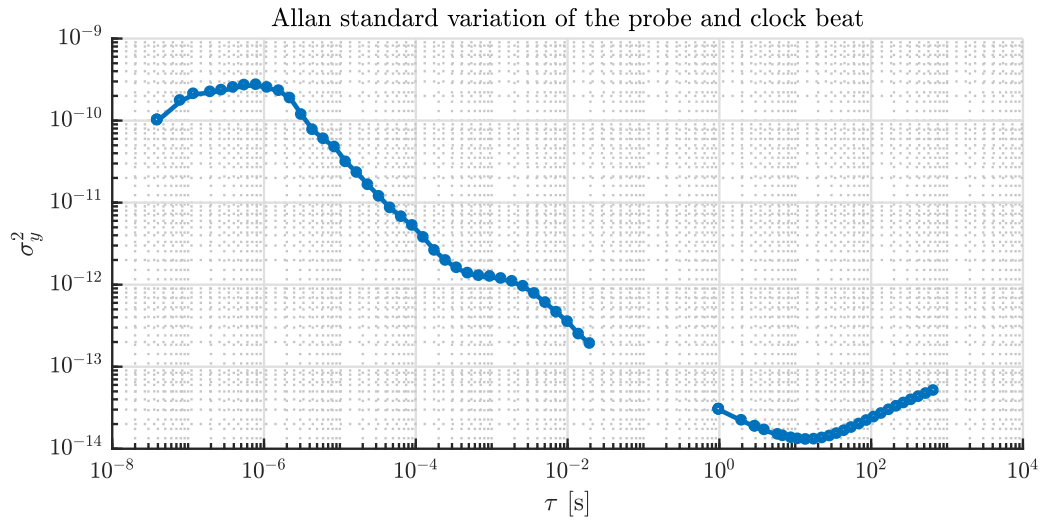

Figure 8.14: Allan standard variation of the probe and clock laser beat frequency

analysis as well, as long as we compensate for the linear drift. figure 8.14 shows the allan standard variation plot for the two timescales. The two plots seem to generally agree, although each of them was evaluated using a different measurement scheme (and different interrogation times). The two lasers achieve the maximal stability at about 10 seconds of integration, after which a linear term $\propto \tau$ degrades the frequency stability. This kind of stability loss seems to be due to frequency drift, and can be explained by either the residual frequency drift of the stable laser cavity or from probe laser's cavity drift, both of which are sub $\mathrm{Hz\,s^{-1}}$ drift and become dominant over times longer then a couple of seconds.

8.4 Ion Measurements

8.4.1 Rabi Spectroscopy

We performed Rabi spectroscopy on the trapped ion, with the aim of observing the narrow resonance of the $\left|4S_{1/2}\right\rangle \rightarrow \left|4D_{5/2}\right\rangle$ quadrapole transition. We know from Eq. (6.14) that the detuning, and through that so does phase-noise, changes the effective Rabi frequency throughout the pulse, and widening the spectroscopic lobe. This makes this kind of spectroscopic measurement a useful tool for noise analysis. The frequency detuning at any moment is equally affected by the laser induced phase noise and ion related phase noise, so this kind of observation will teach us only about the laser to ion relative phase (or frequency) noise.
With the results presented in section 8.3.3 in mind (specifically, the 20 Hz full width at half the max of the two lasers beat presented in figure 8.12), we hoped to observe a resonance peak of the same width. Considering the Furrier limit of a rectangular pulse, indicated by Eq. (6.21), we note that as our laser spectral content is broadened by the inverse of our interrogation time. Therefore we expect our combined laser-ion phase noise to come into play only for long enough interrogation times, when frequency broadening due to phase noise surpasses that imposed by the Furrier limit. Figure 8.15 presents such Rabi spectroscopy measurements, each differs by the interrogation pulse duration. In each measurement the laser frequency was scanned along 13 points in the region of the ion optical resonance frequency. We repeated the measurement at each frequency 100 times, so to reduce the quantization noise by at least an order of magnitude. For each series of measurements a $sinc^2$ model with variable resonance frequency, width and maximal hight was fitted, and its width was estimated. The four measurements here shows that the observed resonance is as wide as imposed by

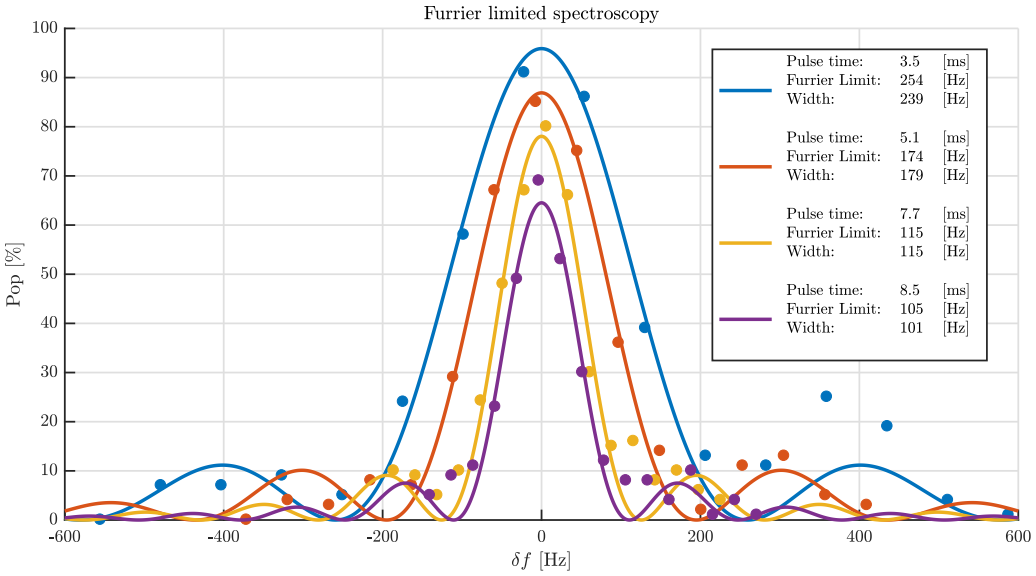

Figure 8.15: Furrier limited Rabi spectroscopy shown for different pulse duration along with the respective Furrier limit and measured FWHM for the fitted model

the corresponding Furrier limit, here even up to 8.5 ms pulses corresponding to a 100 Hz Furrier limit. When we tried to perform longer interrogation time so to push the Furrier limit down, we ran into a threshold at about 100 Hz, and couldn't get a narrower resonance measurement. Figure 8.16 presents four such measurements where the interrogation time (8.5 ms) corresponds to a Furrier limit of about 100 Hz. The estimated width of the fitted model showed a slightly wider resonance, indicating we might be limited by the laser-ion relative phase noise process.

To observe such narrow resonance peaks, we had to overcome a systematic modulation of the ion resonance frequency entering though magnetic field coupling (and Zeeman splitting). 50 Hz Magnetic field oscillations and its higher harmonics, usually associated with the power grid, causes a large frequency modulation of the hyperfine levels, according to Eq. (6.31). When the interrogation time

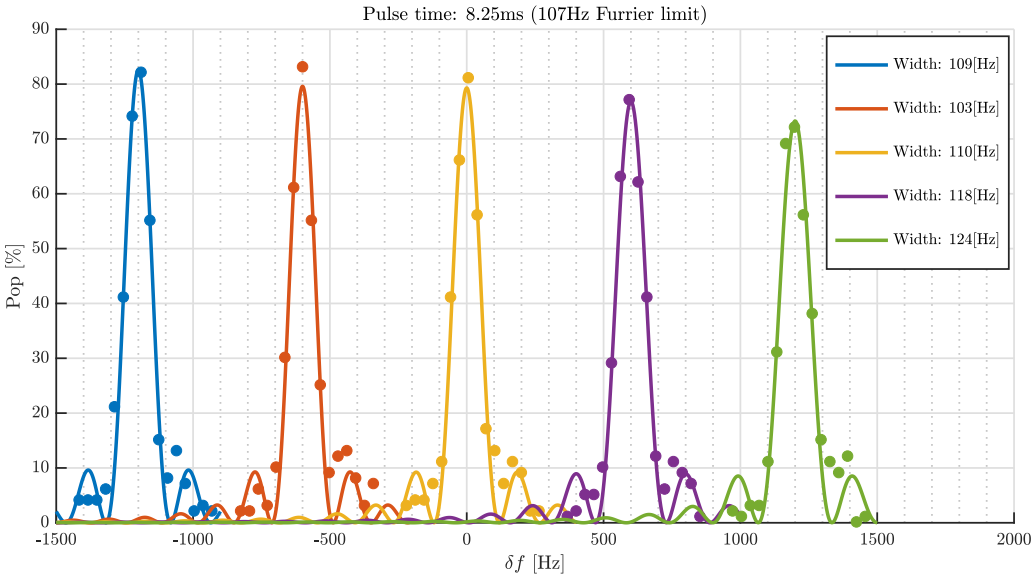

Figure 8.16: Four different spectroscopic measurement of the optical resonance frequency performed over the same interrogation time ($8.25ms$), artificially shifted in δf

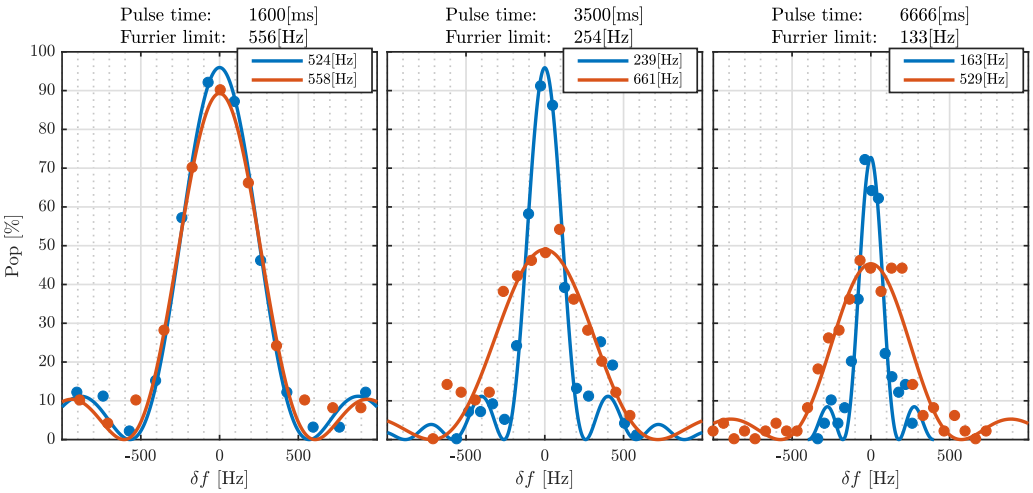

Figure 8.17: Spectroscopy measurement with (blue) and without (red) active fiber noise cancellation system. While the pulse duration increases from left to right, the red trend width remains nearly constant at around 550 Hz

is very short with respect to the modulation period time of ∼20 ms, this effect is negligible. However, as we try to obtain a narrower spectroscopy by prolonging the interrogation time, the frequency excursion through this effect becomes dominant. Being so, when the multiple experiments starts at different phases of the magnetic modulation, they each experiences different substantial phase excursion, leading to loss of coherence and disappearance of the spectroscopy pattern. On the other hand, if all experiments starts at the same phase of the magnetic modulation, they all experience relatively the same phase excursion, which adds up coherently when averaged. Thus, to fight the decoherence described above we triggered each experiment with respect to the 50 Hz power grid period. The exact triggering point is scanned to yield a low overall effect on the shape of the spectroscopic fringe.

When we tried interacting with the laser for longer time durations then those presented in fig 8.16, the resulting measurement width was even wider than we observed for shorter pulses. This might serve as evidence for the existence of dominant $1/f$ noise, exhibiting larger modulation depths for lower spectral frequencies. The narrow 100 Hz wide resonance agrees with a previous measurement done in [40], where for the characterization of the probe laser a similar series of measurements where conducted and a narrow 100 Hz resonance was attained as well. Considering the 20 Hz narrow beat of the two lasers over an larger interrogation time by about ten times, we can suspect that the strong low frequency phase noise originates at the ion. The ability to observe the optical resonance to a 100 Hz resolution gave us an opportunity to inspect the effect fiber-induced phase noises. To do so we conducted three measurements twice, once with the fiber noise cancellation system working, and once with the fiber noise correction feedback disconnected (and the fiber noise correction VCO replaced with a sufficiently low phase noise DDS). Figure 8.17 presents these measurements, with the blue trend marking the results obtained with the fiber noise cancellation system working and the red trend corresponding to measurement outcomes without fiber noise correction. In the first plot the two spectra have the same width corresponding to the Furrier limit induced by the relatively short interaction time of about 550 Hz. When the interrogation time got longer, as in the second and third frame, only the fiber noise compensated laser was able to show narrower spectroscopy, while without fiber noise compensation the spectroscopy signal remained limited at about 500 Hz. This measurement outcome agrees with that found when we examined the two lasers beat signal (figure 8.11, boxed), so this effect was measured consistently.

Another phenomenon we could easily observe is the laser frequency drift. To do this we repeatedly

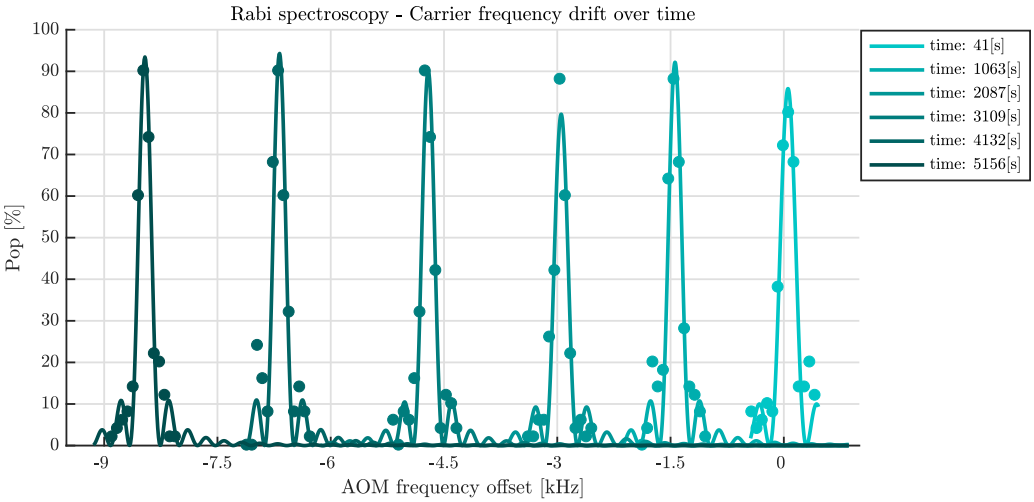

(a) Spectroscopy measurements performed over different times shows a drift in the AOM resonance frequency

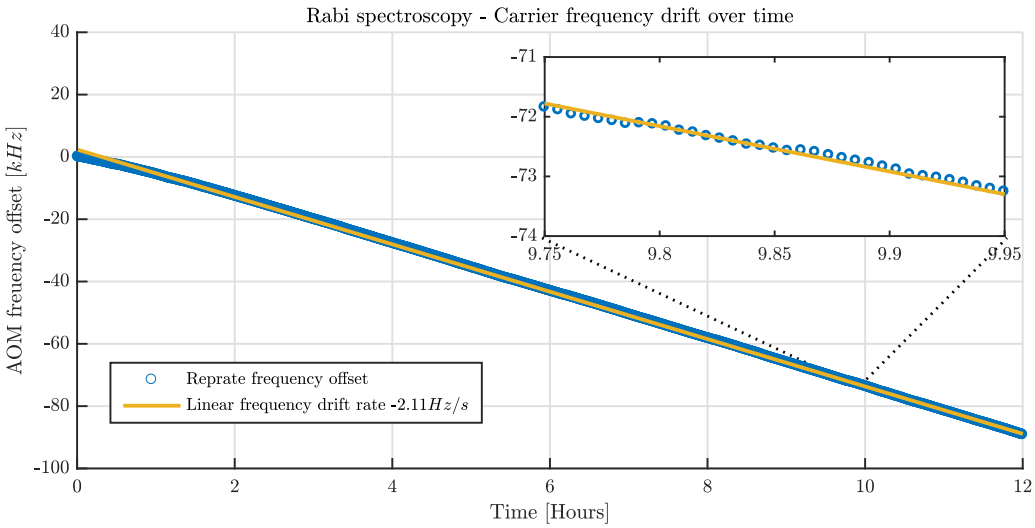

(b) The carrier frequency of each spectrscopy measurement was estimated and these are plotted Vs. time time since the beginning of the experiment

Figure 8.18: Rabi Spectroscopy exhibiting a linear frequency drift

performed a 1 kHz spectroscopy over 13 frequency points, with a single experiment time of about 20 s and a total experiment time of about 12 h. Figure 8.18a shows the measurements and estimation of the carrier frequency with respect to the AOM offset over time. As the color of the line gets darker (corresponding to later times) the carrier frequency drifts at what seems to be a linear trend. In figure 8.18b a plot of all extracted peaks is presented with respect to the experiment time, showing a clear linear drift, here lasting over night for more then 12 hrs. The yellow line is the linear fit to the model, showing a 2.1 Hz s^{-1} frequency drift rate. This result agrees with the previous drift rate measurements (the repetition rate drift and the two lasers beat), supporting previous findings regarding the laser frequency drift.

8.4.2 Rabi Oscillations

We performed and measured Rabi oscillations of the $|S\rangle \rightarrow |D\rangle$ transition, each time with different laser power (and $\Omega_0 \propto |E|^2$). We measured the ion state after letting it interact with our laser for increasing

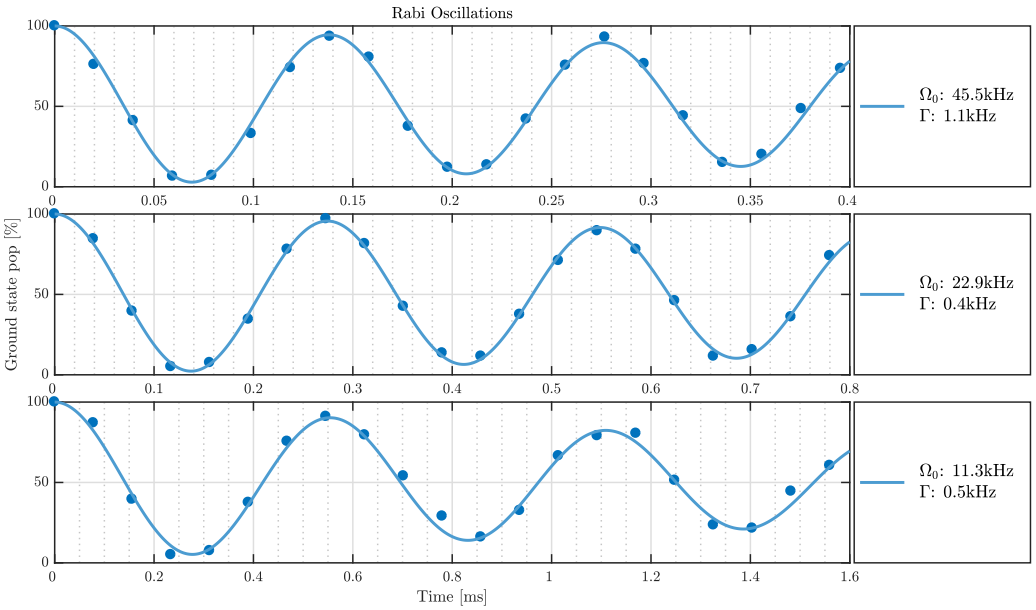

Figure 8.19: Relatively low power Rabi oscillations, showing low decoherence rate

interaction times, starting with zero time interaction. As before, we repeated the measurement for each interaction time about 100 times to reduce quantization noises. The measurement outcome was then a time series of the $\left|5S_{1/2}\right\rangle$ population while interacting with our laser of Rabi frequency Ω_0. We then fitted a two parameter model for Rabi oscillations with decoherence term, as presented in Eq. 6.25, and extracted both the actual Rabi frequency Ω_0 and the decoherence rate γ (Γ in the graphs). Figures 8.19 and 8.20 shows these measurement performed for a variety of fields strengths. The line in each graph correspond to the two parameters fitted model, with the fitted parameters Ω_0 and Γ presented to the right. The estimated decoherence should correspond to the random ion-laser phase noise, and in figure 8.19 we estimated it to be about $500\,\mathrm{s}^{-1}$. However, when shorter times are considered and higher laser power is configured so that the Rabi frequency is larger, the decoherence rate grows bigger with the laser power, and in figure 8.20 for $\Omega_0 = 350\,\mathrm{krad\,s}^{-1}$ the decoherence rate is about 100 times bigger than it is estimated for weaker laser power ($\Omega_0 = 11.3\,\mathrm{krad\,s}^{-1}$). We suspected the reason for the degradation in coherence time is the high frequency noise, which becomes more dominant as we increase the laser power. A similar result was demonstrated in [43], where frequency comb residual

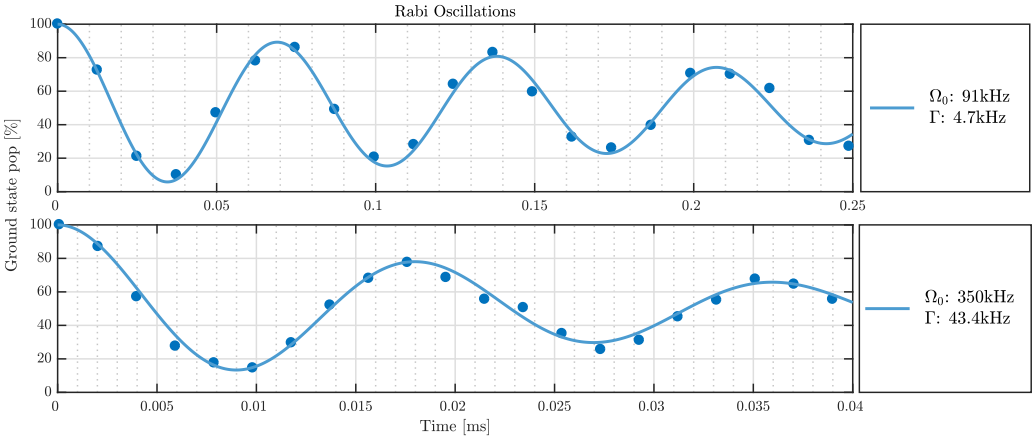

Figure 8.20: High power Rabi oscillations exhibiting fairly high decoherence rate, growing stronger with increasing Rabi frequency

phase noise at about 100 kHz led to larger de-coherence rate for Rabi oscillations. As we couldn't find a model to explain this kind of phenomena, we plan to perform a stochastic simulation of a laser with a phase noise of similar properties with the goal of observing the same effect. This feature of our laser limits its ability to perform fast coherent operations such as logical rotations or even fast $\frac{\pi}{2}$-pulses for spectroscopy.

8.4.3 Ramsey Spectroscopy

To further investigate our laser linewidth we performed Ramsey spectroscopy measurements. We initialized the ion at the $\left|5S_{1/2}, -1/2\right\rangle$ state, and performed a $\pi/2$-pulse to further excite our atom to the $\left|5S_{1/2}, -1/2\right\rangle \leftrightarrow \left|4D_{5/2}, -3/2\right\rangle$ superposition. We let our ion evolve and measured the excitation probability at different times. We fitted our results to a model with exponentially decaying amplitude according to Eqs. (6.29) and (6.30). We then repeated the experiment magnetic field dynamic decoupling pulses. We chose to perform the dynamic decoupling on the $\left|4D_{5/2}, -3/2\right\rangle \leftrightarrow \left|4D_{5/2}, 3/2\right\rangle$ levels, as according to Eq. (6.31) the levels susceptibility is:

$$\begin{aligned} \chi_{-1/2,-3/2} &= -2.802 \cdot (-0.5) + 1.68 \cdot (-1.5) = -1.12 \text{ MHz/G} \\ \chi_{-1/2,3/2} &= -2.802 \cdot (-0.5) + 1.68 \cdot (1.5) = 3.92 \text{ MHz/G} \end{aligned} \tag{8.6}$$

We performed the experiment according to the scheme presented in figure 6.4.the times T_1 and T_2 where chosen such that their ratio correspond to the susceptibility ratio according to Eq. (6.32). The total experiment time could be therefore described as:

$$T = N \cdot (T_1 + T_2) \tag{8.7}$$

With N being the number of pulses per experiment. Figure 8.21 presents the measurement outcomes for Ramsey measurements with no MFDD pulses, one pulse and four pulses over each measurement time. Each experiment took several minutes, and the laser drift measured previously became a limiting factor. We measured the time between each experiment and compensated for the drifted frequency

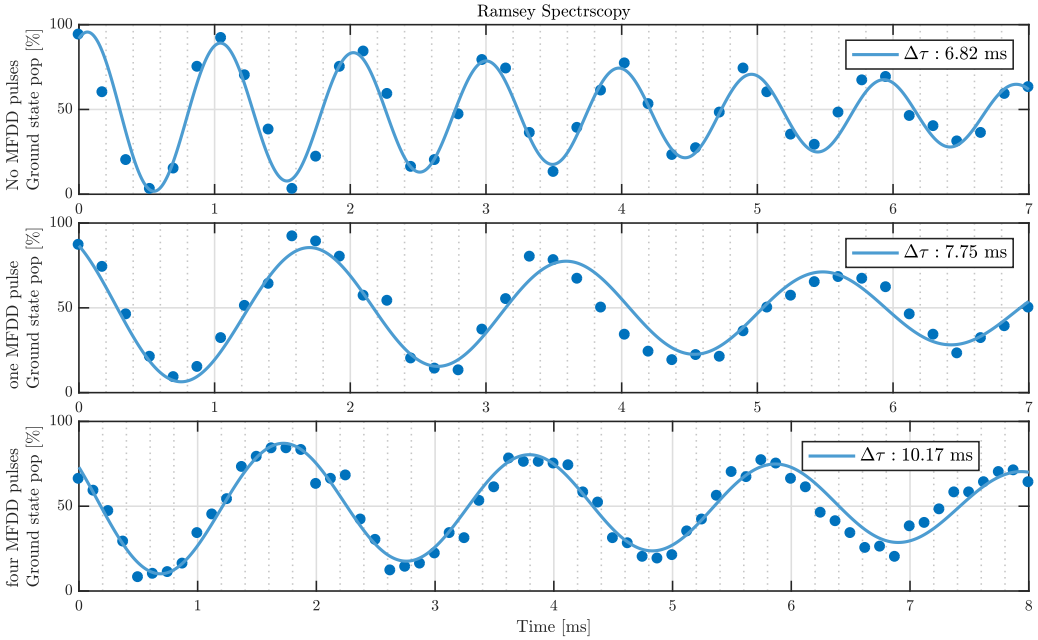

Figure 8.21: Ramsey spectroscopy fringes, for different amount of magnetic field dynamic decoupling pulses. The decay time is a measure of the combined laser-ion phase noise

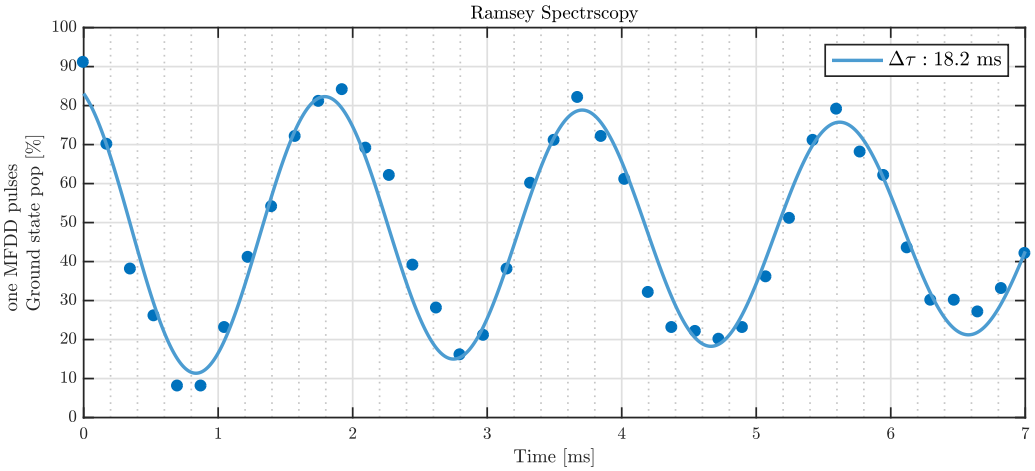

Figure 8.22: Ramsey spectroscopy with one MFDD pulse, showing relatively low decoherence rate

by shifting the laser frequency using the AOM at an amount equal to the measured time multiplied by the estimated drift rate. This rate, however, seemed to not be constant on a day-by-day basis, so we changed our fit model to include a linear drift term, thus it should not effect the decoherence rate of the Ramsey fringes. The three measurement shows an increasing coherence time with increasing number of MFDD pulses. The 4 pulses measurement, with decay time $\Delta\tau = 10.17$ms seemed to be the best decoherence rate we could observe, and adding further pulses did not seem to prolong the decay time. According to the relation of Eq. (6.30), This kind of decay correspond to a spectral density width of:

$$\Delta\omega = \frac{\pi}{0.01017} = 308\text{Hz} \tag{8.8}$$

Which is an order of magnitude larger then the spectral width of the two lasers, indicating that the ion phase noise might still be a limiting factor, even after applying the MFDD pulses. On one specific measurement involving one MFDD pulse we estimated a decay rate of 18.2 ms, corresponding to spectral width of about 170 Hz. This measurement is presented in figure 8.22.

8.5 Summary

In this work we demonstrated the ability to transfer the phase stability of a narrow linewidth laser down to other portions of the optical spectrum using a frequency comb as a frequency bridge. We built a phase locking setup for a 674 nm laser diode and analyzed its properties when locked compared to a cavity referenced stable laser of the same wavelength, and compared to a trapped ion. We showed that even though the short term stability is degraded (because of what seems to be the comb lock bandwidth), low frequency phase noise around the carrier is still greatly eliminated and a narrow linewidth beat note can be measured. We've seen that in that fiber induced noise becomes a limiting factor on such narrow linewidth laser, and built a fiber noise cancellation setup to eliminate it. When inspecting the ion we learned that fast and powerful logic or spectroscopic measurements suffers from the excess phase noise imprinted on the laser. On the other hand, long time interactions do maintain coherency and spectroscopic measurements can be performed to low resolution limit, eventually limited by phase noise originating from the ion. As an atomic clock laser candidate, this scheme seems to provide a laser with an acceptable stability characteristics On the other hand, performing high fidelity quantum logic operations (or even fast enough $\pi/2$ pulses for Ramsey type experiments) seems to be a problem considering the laser high frequency phase noise profile. This is a problem that should be addressed when further designing an optical clock based on such laser.

Bibliography

[1] Th Udem, A Huber, B Gross, J Reichert, M Prevedelli, M Weitz, and Th W Hänsch. Phase-coherent measurement of the hydrogen 1 s- 2 s transition frequency with an optical frequency interval divider chain. *Physical Review Letters*, 79(14):2646, 1997.

[2] Till Rosenband, DB Hume, PO Schmidt, Chin-Wen Chou, Anders Brusch, Luca Lorini, WH Oskay, Robert E Drullinger, Tara M Fortier, JE Stalnaker, et al. Frequency ratio of al+ and hg+ single-ion optical clocks; metrology at the 17th decimal place. *Science*, 319(5871):1808–1812, 2008.

[3] N Hinkley, JA Sherman, NB Phillips, M Schioppo, ND Lemke, K Beloy, M Pizzocaro, CW Oates, and AD Ludlow. An atomic clock with 10–18 instability. *Science*, 341(6151):1215–1218, 2013.

[4] Wayne M Itano, James C Bergquist, John J Bollinger, JM Gilligan, DJ Heinzen, FL Moore, MG Raizen, and David J Wineland. Quantum projection noise: Population fluctuations in two-level systems. *Physical Review A*, 47(5):3554, 1993.

[5] G John Dick. Local oscillator induced instabilities in trapped ion frequency standards. Technical report, CALIFORNIA INST OF TECH PASADENA JET PROPULSION LAB, 1987.

[6] Audrey Quessada, Richard P Kovacich, Irène Courtillot, André Clairon, Giorgio Santarelli, and Pierre Lemonde. The dick effect for an optical frequency standard. *Journal of Optics B: Quantum and Semiclassical Optics*, 5(2):S150, 2003.

[7] Andrew D Ludlow, X Huang, M Notcutt, T Zanon-Willette, SM Foreman, MM Boyd, S Blatt, and Jun Ye. Compact, thermal-noise-limited optical cavity for diode laser stabilization at $1\times$ 10-15. *Optics letters*, 32(6):641–643, 2007.

[8] Mark Notcutt, Long-Sheng Ma, Jun Ye, and John L Hall. Simple and compact 1-hz laser system via an improved mounting configuration of a reference cavity. *Optics letters*, 30(14):1815–1817, 2005.

[9] Fritz Riehle. *Frequency standards: basics and applications*. John Wiley & Sons, 2006.

[10] Jacques Rutman and FL Walls. Characterization of frequency stability in precision frequency sources. *Proceedings of the IEEE*, 79(7):952–960, 1991.

[11] David W Allan. Statistics of atomic frequency standards. *Proceedings of the IEEE*, 54(2):221–230, 1966.

[12] James A Barnes, Andrew R Chi, Leonard S Cutler, Daniel J Healey, David B Leeson, Thomas E McGunigal, James A Mullen, Warren L Smith, Richard L Sydnor, Robert FC Vessot, et al. Characterization of frequency stability. *IEEE transactions on instrumentation and measurement*, 1001(2):105–120, 1971.

[13] Nitzan Akerman. *Trapped Ions and Free Photons*. PhD thesis, Weizmann Institute of Science, Rehovot, Israel, 2012.

[14] Charles Henry. Theory of the linewidth of semiconductor lasers. *IEEE Journal of Quantum Electronics*, 18(2):259–264, 1982.

[15] Arthur L Schawlow and Charles H Townes. Infrared and optical masers. *Physical Review*, 112(6):1940, 1958.

[16] A Barlow and D Payne. The stress-optic effect in optical fibers. *IEEE Journal of quantum electronics*, 19(5):834–839, 1983.

[17] GB Hocker. Fiber-optic sensing of pressure and temperature. *Applied optics*, 18(9):1445–1448, 1979.

[18] Yi Pang, Jeffrey J Hamilton, and Jean-Paul Richard. Frequency noise induced by fiber perturbations in a fiber-linked stabilized laser. *Applied optics*, 31(36):7532–7534, 1992.

[19] Long-Sheng Ma, Peter Jungner, Jun Ye, and John L Hall. Delivering the same optical frequency at two places: accurate cancellation of phase noise introduced by an optical fiber or other time-varying path. *Optics letters*, 19(21):1777–1779, 1994.

[20] Orazio Svelto and David C Hanna. *Principles of lasers*, volume 4. Springer, 1998.

[21] LE Hargrove, Richard L Fork, and MA Pollack. Locking of he–ne laser modes induced by synchronous intracavity modulation. *Applied Physics Letters*, 5(1):4–5, 1964.

[22] Daniel K Negus, Luis Spinelli, Norman Goldblatt, and Gilles Feugnet. Sub-100 femtosecond pulse generation by kerr lens mode-locking in ti: Al2o3. In *Advanced Solid State Lasers*, page SPL7. Optical Society of America, 1991.

[23] Steven T Cundiff. Phase stabilization of ultrashort optical pulses. *Journal of Physics D: Applied Physics*, 35(8):R43, 2002.

[24] Th Udem, J Reichert, R Holzwarth, and TW Hänsch. Accurate measurement of large optical frequency differences with a mode-locked laser. *Optics letters*, 24(13):881–883, 1999.

[25] David J Jones, Scott A Diddams, Jinendra K Ranka, Andrew Stentz, Robert S Windeler, John L Hall, and Steven T Cundiff. Carrier-envelope phase control of femtosecond mode-locked lasers and direct optical frequency synthesis. *Science*, 288(5466):635–639, 2000.

[26] L Richter, H Mandelberg, M Kruger, and P McGrath. Linewidth determination from self-heterodyne measurements with subcoherence delay times. *IEEE Journal of Quantum Electronics*, 22(11):2070–2074, 1986.

[27] Linden B Mercer. 1/f frequency noise effects on self-heterodyne linewidth measurements. *Journal of Lightwave Technology*, 9(4):485–493, 1991.

[28] Ulrich L Rohde, Ajay K Poddar, and Anisha M Apte. Getting its measure: Oscillator phase noise measurement techniques and limitations. *IEEE Microwave Magazine*, 14(6):73–86, 2013.

[29] Katsuhiko Ogata and Yanjuan Yang. Modern control engineering. 1970.

[30] Floyd M Gardner. *Phaselock techniques*. John Wiley & Sons, 2005.

[31] MG Raizen, JM Gilligan, James C Bergquist, Wayne M Itano, and David J Wineland. Ionic crystals in a linear paul trap. *Physical Review A*, 45(9):6493, 1992.

[32] David J Wineland, C Monroe, Wayne M Itano, Dietrich Leibfried, Brian E King, and Dawn M Meekhof. Experimental issues in coherent quantum-state manipulation of trapped atomic ions. *Journal of Research of the National Institute of Standards and Technology*, 103(3):259, 1998.

[33] Daniel A Steck. Quantum and atom optics. *Oregon Center for Optics and Department of Physics, University of Oregon*, 47, 2007.

[34] HG Dehmelt. Bull. am. phys. soc. 20, 60 (1974). *Bull. Am. Phys. Soc.*, 20:60, 1974.

[35] Max Born and Emil Wolf. *Principles of optics: electromagnetic theory of propagation, interference and diffraction of light*. Elsevier, 2013.

[36] Nitzan Akerman, Nir Navon, Shlomi Kotler, Yinnon Glickman, and Roee Ozeri. Universal gate-set for trapped-ion qubits using a narrow linewidth diode laser. *New Journal of Physics*, 17(11):113060, 2015.

[37] G Grosche, O Terra, Katharina Predehl, Ronald Holzwarth, B Lipphardt, F Vogt, U Sterr, and H Schnatz. Optical frequency transfer via 146 km fiber link with 10- 19 relative accuracy. *Optics letters*, 34(15):2270–2272, 2009.

[38] Leopoldo Angrisani, Massimo D'Apuzzo, and Mauro D'Arco. A digital signal-processing approach for phase noise measurement. *IEEE Transactions on instrumentation and measurement*, 50(4):930–935, 2001.

[39] Yinnon Glickman. *Ion-Ion and Ion-Photon Entanglement in Trapped Ions System*. PhD thesis, Weizmann Institute of Science, Rehovot, Israel, 2012.

[40] Ravid Shaniv. Spectral noise analysis of a narrow line-width laser using a single trapped ion. Master's thesis, Weizmann Institute of Science, Rehovot, Israel, 2015.

[41] Tom Manovitz. Individual addressing and imaging of ion in a paul trap. Master's thesis, Weizmann Institute of Science, Rehovot, Israel, 2016.

[42] James E Gray and David W Allan. A method for estimating the frequency stability of an individual oscillator. In *28th Annual Symposium on Frequency Control. 1974*, pages 243–246. IEEE, 1974.

[43] Nils Scharnhorst, Jannes B Wübbena, Stephan Hannig, Kornelius Jakobsen, Johannes Kramer, Ian D Leroux, and Piet O Schmidt. High-bandwidth transfer of phase stability through a fiber frequency comb. *Optics Express*, 23(15):19771–19776, 2015.